NATURAL AND SYNTHETIC MINERAL SILICATES AS FUNCTIONAL NANOPARTICLES IN POLYMER COMPOSITES

By

Hua Shao

A DISSERTATION

Submitted to
Michigan State University
in partial fulfillment of the requirements
for the degree of

DOCTOR OF PHILOSOPHY

Chemistry

2009

ABSTRACT

NATURAL AND SYNTHETIC MINERAL SILICATES AS FUNCTIONAL NANOPARTICLES IN POLYMER COMPOSITES

By

Hua Shao

A new strategy is described for the substantial enhancement of the barrier properties for both a thermoset epoxy polymer and a thermoplastic polyolefin by sandwiching a novel self-supported clay fabric film between thin polymer sheets. The success of this strategy is attributed to the high orientation of clay nanolayers in the paper-like clay fabric films and to the filling of the micro- or sub-micro sized voids between imperfectly tiled clay platelet edges by the polymer chains.

Thermoplastic polyolefin-clay fabric film composites were fabricated by hot-pressing the clay films between two sheets of high density polyethylene (HDPE) films. The sandwiched composites exhibit more than a 30-fold decrease in O_2 transmission rate with respect to the pure HDPE film. Impregnating the self-supported clay papers with epoxy pre-polymers successfully leads to thermoset composite films with more than 2-3 orders of magnitude reduction in O_2 permeability in comparison to the pristine epoxy matrix.

Owing to the promising use of synthetic Mg-saponite (denoted SAP) as epoxy polymer reinforcing agents, we investigated the cost-effective synthesis of SAP by replacing urea with sodium hydroxide as base source. Co-crystallization of new zeolite phases, such as garronite (denoted GIS) and cancrinite (denoted CAN), occurred along with SAP upon increasing the alkalinity of the reaction

mixture. This finding represents the first example of the preparation of a CAN/SAP phase mixture. Moreover, pure-phase cancrinite with rod-like morphology up to several μm in length was synthesized under Mg-free conditions. Also, the Si/Al ratio within the synthesis gel has an influence on the chemical composition and textural properties of pure CAN crystals.

Microporous cancrinite is a promising candidate for reinforcing epoxy polymers, considering that CAN represents a substantial fraction of the mixed CAN-SAP phase formed during the synthesis of saponite. Therefore, the reaction conditions (e.g. alkalinity, reaction temperature, and duration) were further expored in order to optimize the formation of small crystals of CAN (~ 100 nm) with large external surface area and high pore volume. These textural features facilitate the homogeneous dispersion of cancrinite particles in epoxy matrices. In addition, a new phase sodalite (denoted SOD) was co-crystallized along with CAN in some cases, depending on reaction conditions.

The synthetic zeolites CAN and SOD act as reinforcing agents for thermoset epoxy polymers owing in part to their small particle size, large surface area and high pore volume. The tensile strength, modulus and toughness of an epoxy matrix are simultaneously enhanced without the need for organic surface modification of zeolites. This finding represents the first example for which the mechanical properties of glassy epoxy composite are all improved through the use of a microporous zeolite as a functional inorganic nanoparticle.

ACKNOWLEDGEMENT

First, I would like to express my appreciation to Professor Thomas J. Pinnavaia for his thoughtful and kind guidance for the last five years. I learned a lot of things from him that I need to be an independent researcher. I feel extremely lucky to be his student.

Also, I would like to thank former and current group members. Dr. Park had great patience in teaching me how to use the MOCON instrument and to prepare epoxy-clay film composites. Dr. Xue helped me a lot by showing me how to synthesize saponite and make glassy epoxy nanocomposites. Dr. Sun has always been willing to help me when I got troubles especially my early years in the US. Dr. Kim, Dr. Zhang and Dr. Wang are very nice to me and they are really diligent and smart people. I also enjoyed the experience of working with Joel for the Ford project back in 2007. My close friend Gwen has always shared good and bad things happening to me.

I could not have finished my PhD study without the love and support from my parents, Mr. Jingchao Shao and Mrs. Xiaoyun Zhou. I would also like to dedicate this humble thesis to my beloved husband, Ilhwan An.

TABLE OF CONTENTS

CHAPTER 6

LIST OF TABLES

LIST OF FIGURES

CHAPTER 1

An Overview of Polymer-Based Nanocomposites

1.1 Clay

Smectite clays are a class of layered silicate minerals characterized by various properties such as a very small particle size, large ion-exchange and adsorption capacities, a low hardness index, and a high particle aspect ratio.[1] The elementary polyhedral building blocks of layered silicates are tetrahedra and octahedra of oxygen ions. The coordinating cations in the center of the tetrahedra are essentially Si, Al, or Fe^{3+}, among which Si is the most frequent. Octahedrally coordinated cations are usually Al, Mg, Fe^{3+} and Fe^{2+}.

The structural unit formed by linking one octahedral sheet to one tetrahedral sheet results in a 1:1 layer, whereas the unit formed by sandwiching one octahedral sheet with two tetrahedral sheets affords a 2:1 layer, as shown in Figure 1.1.[2] The exposed surfaces of 1:1 layers consist of oxygen atoms on the tetrahedral layer surface, and –OH groups on the octahedral layer side. Only bridging oxygen atoms are exposed on the basal surfaces of 2:1 layers. A brief summary of the major 1:1 and 2:1 clay groups is shown in Table 1.1.[1]

1:1 and 2:1 layers are not always neutral. Very often, as a result of isomorphic metal ion substitution in the lattice, the layers bear a net negative charge that is balanced by hydrated cations situated inside the galleries. The galleries cations (Na^+ or K^+) can be displaced by alkylammonium ions through

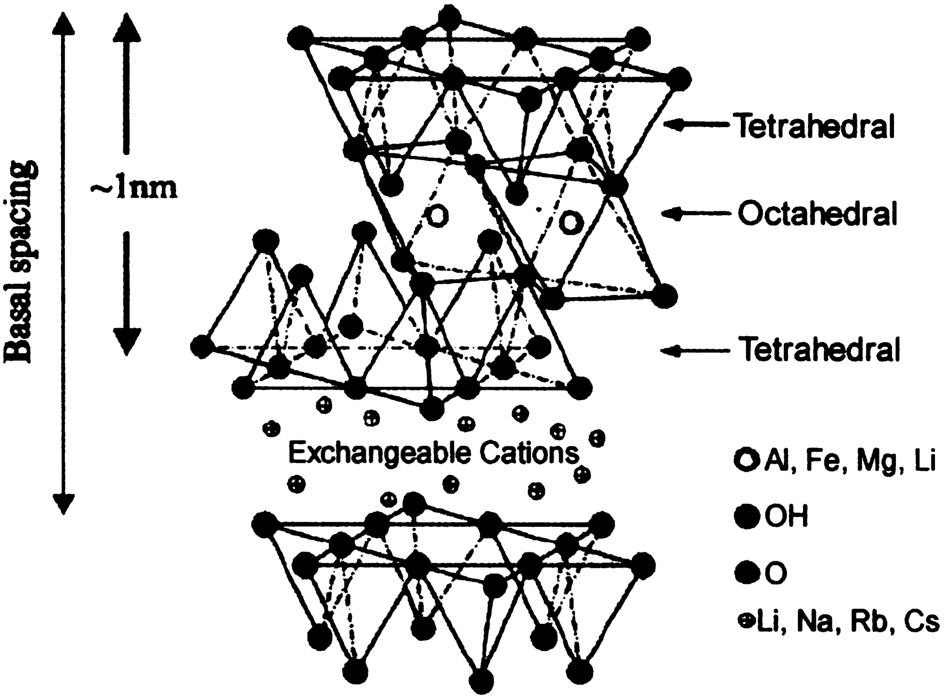

Figure 1.1 Structure of 2:1 phyllosilicates.

Table 1.1 Classification of some clay minerals

Structure type	Mineral group	Charge	Formula
1:1 layer	kaolinite	~0	$[Al_4](Si_4)O_{10}(OH)_8$
2:1 layer	talc	~0	$[Mg_6](Si_8)O_{20}(OH)_4$
	smectite	0.2-0.6	$M^{n+}_x \cdot yH_2O[(Al, Mg, Fe, Zn)_4]((Si, Al)_8)O_{20}(OH)_4$
	vermiculite	1.2-1.8	$Mg^{2+}_x[(Mg, Ca, K, Fe^{2+})_6]((Si, Al, Fe^{3+})_8)O_{20}(OH)_4$

ion-exchange reaction to fine-tune the surface chemistry of clay layers, which converts the normally hydrophilic silicate surface to an organophilic one. Organic modifiers can lower the surface energy of the nanoclay particles and improve the wetting behavior with the polymers. In some cases, cationic surfactants can provide functional end groups that can react with the polymer matrix[3] or catalyze the polymerization of monomers[4-6] to improve the strength of interfacial interactions between the inorganic silicates and the polymer matrix.

The most commonly used layered silicates for the preparation of polymer-clay nanocomposites are smectite clays, which belong to the 2:1 phyllosilicates (Figure 1.1). Typical members of the family are montmorillonite (MMT), hectorite and saponite. The substitution of Al^{3+} by Mg^{2+} results in negative charges on the octahedral sheet in layers of montmorillonite. The negative charge centers are counterbalanced by hydrated sodium or calcium cations in the interlayer between 2:1 silicate sheets. The layer thickness is around 1nm, and the lateral dimensions may vary from 30 nm to several microns or lager, providing a high aspect ratio.

1.2 Polymer-Clay Nanocomposites

Based on the dispersion of clay particles in the polymer matrix, polymer-clay nanocomposites can be divided into three categories as illustrated in Figure 1.2[7]. For the "conventional composites", there's no intercalation of polymer chains into the clay layers and the clay platelets remain as a tactoid structure. Therefore, the X-ray diffraction (XRD) pattern shows the same d-spacing as the pristine clay. Due to the limited interfacial interaction, phase segregation normally occurs in this case. For the "intercalated nanocomposites", polymer molecules penetrate into the clay gallery and correspondingly expand the gallery height. The gallery height expansion is reflected by an increase in the X-ray d-spacing along the layer stacking direction. In the case of "exfoliated or delaminated polymer-clay nanocomposites", individual clay nanolayers are separated by the polymer, as verified by the disappearance of the reflection peak in the low-angle region of X-ray pattern. Exfoliated composites optimize the interfacial interaction between the silicate layers and the polymer matrix and result in simultaneous improvements in mechanical, thermal, flame resistance and barrier properties.

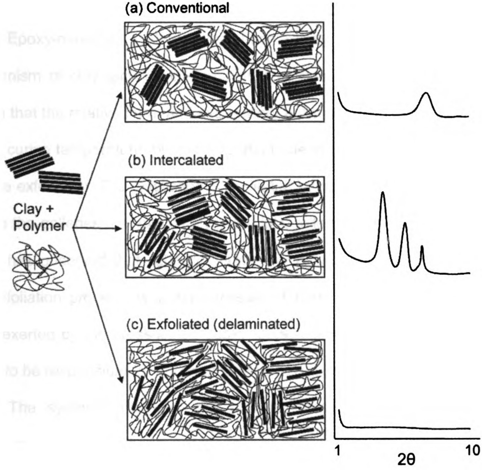

Figure 1.2 Schematic illustrations of three types of polymer-clay nanocomposites: (a) conventional composites, (b) intercalated nanocomposites, and (c) exfoliated (delaminated) nanocomposites. The corresponding X-ray diffraction (XRD) patterns for composites at low-angle region (1-10°) are also shown.

Nanocomposite studies have been carried out on various polymer systems, including polyurethane, polyimide, polyamide, polystyrene, polypropylene, epoxy, etc.[2-6,8-25] In the case of thermoplastic polyurethane[3], nanocomposites containing 5 wt% layered silicate organoclay exhibit a 125% increase in tensile stress, 100% increase in elongation, and 78% increase in tensile modulus along with a 130% increase in tear strength due to the reinforcement provided by the full exfoliation of nanoclay layers.

Epoxy-nanoclay systems have been widely studied with regard to the mechanism of clay tactoids intercalation and exfoliation. Earlier works[4-6] have shown that the relative intra- and extragallery polymerization rates, along with the epoxy curing temperature, play an important role in controlling the degree of clay particle exfoliation. The exfoliation is facilitated by acidic primary alkylammonium ions in the galleries that can catalyze the intragallery epoxy polymerization. But Jana[8] has observed that catalytic intragallery polymerization, though expedited the exfoliation process, was not necessary for exfoliation. The entropic elastic force exerted by the cross-linked epoxy molecules inside the clay galleries was found to be responsible for the delamination of clay layers.

The synthetic methods and material properties of polypropylene-clay nanocomposites have been widely studied due to the very large commercial importance of polypropylene (PP). In terms of thermodynamics, the dispersion of clay platelets (intercalation or exfoliation) was energetically favorable when the polymer-silicate surface interactions were maximized and polymer-alkyl surfactants interactions were minimized,[26,27] as illustrated in Figure 1.3[28].

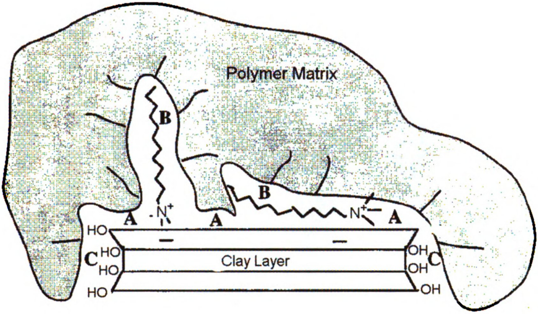

Figure 1.3 Schematic illustration of the types of interfacial interactions occurring in polymer-organoclay nanocomposites, including direct binding (adsorption) of the polymer to the basal siloxane oxygens (type A), "dissolving" of the onium ion chains into the polymer matrix (type B), and polymer binding to hydroxylated edge sites (type C).[28]

Therefore, the incorporation of any polar or polarizable functional groups in polypropylene polymer will promote PP compatibility with organoclays.[18,20-23] For instance, Manias and co-workers[23] prepared maleic anhydride functionalized polypropylene (PP-r-MA) nanocomposites by melting processing. A TEM image of the composite containing 6 wt% organo-MMT clearly shows that there are intercalated tactoids and disordered exfoliated silicate layers coexisting in the nanocomposite structure (Figure 1.4).

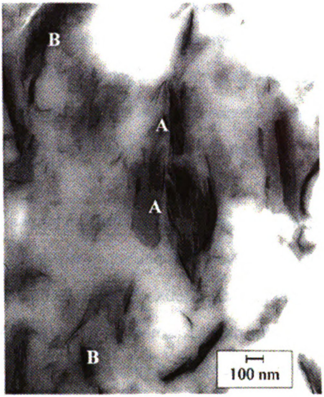

Figure 1.4 TEM image of the MA-functionalized-PP/2C18-montmorillonite (MMT) nanocomposite structure at 6 wt% loading, showing the coexistence of intercalated clay tactoids (A) and disordered exfoliated clay layers (B).[23]

The goal of MA functionalization was to improve the interactions between the polymer and layered silicate surfaces so as to become thermodynamically more favorable compared to the polymer-surfactants interactions. The same effect can be achieved by decreasing the interactions between the polymer and alkyl surfactants, which subsequently will render the PP/clay contacts favorable. This approach can be realized by introducing appropriate organic modifiers, such as semi-fluorinated surfactants.[25] Specifically, octadecylammonium exchanged montmorillonite was further modified by reaction with a semi-fluorinated alkyltrichlorosilane surfactant (CF_3-$(CF_2)_5$-$(CH_2)_2$-Si-Cl_3), which was grafted to the clay surface through an interaction of the trichlorosilane groups with hydroxyls in the cleavage plane of the montmorillonite. An estimated 25% and 40% of the resulting clay layers are exfoliated in unfunctionalized PP nanocomposites made via melt-intercalation processing and through extrusion in a twin-screw extruder, respectively.

It has been realized recently that unmodified synthetic inorganic clays can disperse uniformly in polymer matrix and thus provide mechanical reinforcement and improvement in thermal properties. Xue[29] reported that synthetic porous Mg-saponite[30] improves the tensile properties of both rubbery and glassy epoxy matrices without the need for the organic modification of the clay surface. The improvements in tensile strength, modulus and toughness are superior to those of orgaoclays, a result that is ascribed to the irregular stacking and textural porosities of saponite nanolayers. The polymer fills the interparticle pores, thereby resulting in favorable interfacial interactions and reducing the tendency toward microcrack formation. Using a novel solvent-exchange method, McKinley and co-workers successfully dispersed the fully exfoliated synthetic laponite nanolayers in a thermoplastic elastomer, composed of polyurethane and polyether block copolymer, and preferentially reinforced the polyurethane hard microdomains.[15] The stronger adhesion of the hydrophilic, unmodified laponite with the more polar hard segments rather than with the soft segments allows the laponite to segregate into the hard microdomains during processing, thus resulting in the increase in the stiffness, toughness and heat distortion

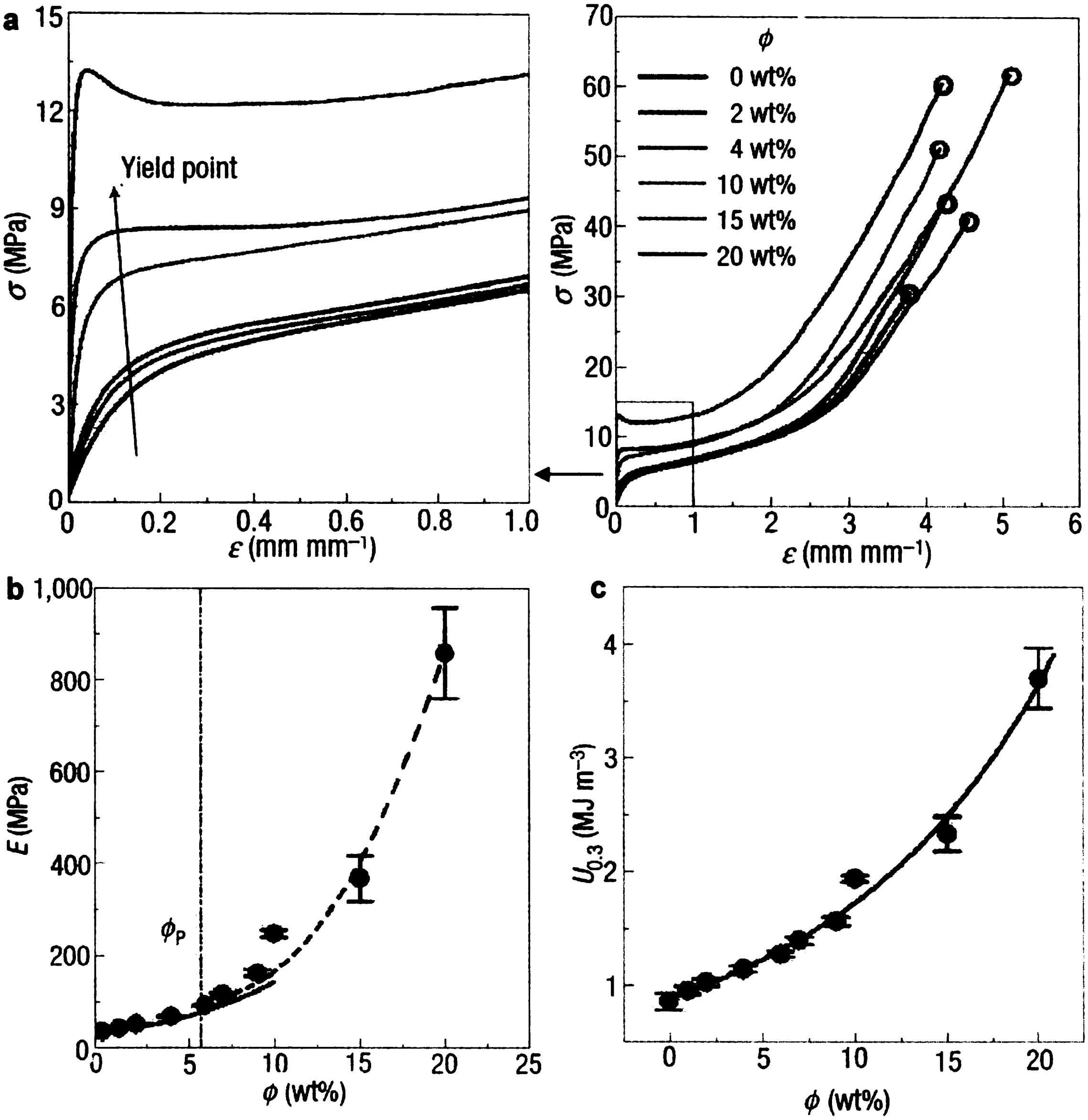

Figure 1.5 Effect of laponite concentration on the mechanical properties of thermoplastic elastomers. **a**, Representative stress-strain (σ-ε) curves of thin-film nanocomposites containing between 0 and 20 wt% laponite. **b**, Initial elastic modulus, E, increases with increasing laponite concentration, Φ. **c**, Toughness, $U_{0.3}$ (defined as the area under the σ-ε curve up to ε=0.3, increases quadratically with Φ. The error bars in **b, c** are equal to one standard deviation (minimum of five samples) plus the contribution based on the instrument imprecision.[15]

temperature of the material. The dramatic influence of laponite on the elastic modulus of polyurethane is shown in Figure 1.5[15]. The initial modulus of the elastomer increases significantly with increasing laponite concentration as this region is governed by the polyurethane crystallinity. Specifically, the sharp increase in modulus at $\Phi > 6$ wt% (Figure 1.5 b), is a consequence of the percolative laponite network. After the yield point, the region of moderate slope is indicative of soft-segment deformation and the steep upturn is characterized by the strain-induced crystallization of the soft domains. The addition of laponite does not affect the slopes of these two regions, which can be explained by the fact that there is no interaction between the smectite clay and soft microdomains.

1.3 Barrier Properties of Polymer-Clay Nanocomposites

The mechanism of barrier improvement for polymer-clay nanocomposites was first explained by Nielson's tortuous path model (Figure 1.6), wherein the exfoliated impermeable nanoclay layers are highly oriented and retard the transport of diffusing species, such as oxygen and water molecules.[31] The tortuosity factor (τ) is defined by the ratio of the actual distance that a diffusing gas must travel to the shortest distance that it would have traveled in the absence of the layered silicate and is expressed in terms of the length (L), width (W), and volume fraction of the clay (Φ) as

$$\tau = 1+(L/2W)\,\Phi = 1+ \alpha\,\Phi/2 \qquad \text{(Equation 1.1)}$$

where α is the aspect ratio of the silicate clay. Relative permeability is defined by the ratio of the permeability of the composite to that of the pristine polymer:

$$P_c/P_p = 1 / [1+(L/2W)\ \Phi] = 1 / (1+ \alpha\ \Phi/2) \qquad \text{(Equation 1.2)}$$

where P_c and P_p represent the permeabilities of the composite and pure polymer, respectively. It can be seen that the relative permeability P_c/P_p equals $1/\tau$.

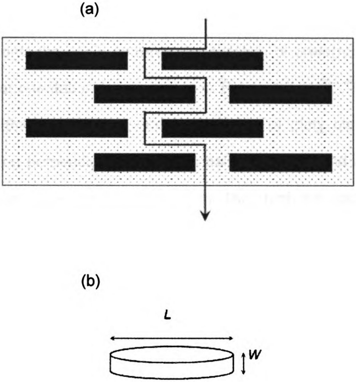

Figure 1.6 (a) A tortuous path model for a diffusing gas through a polymer filled with highly oriented impermeable disks; (b) Individual clay nanolayer with aspect ratio, $\alpha = L/W$.

In contrast to expectations, only a 2-4-fold reduction in permeability is observed in practice. Nielson's model is based on a key assumption of full exfoliation of clay tactoids and clay nanolayers highly oriented along the direction perpendicular to the film surface. Neither condition is achieved in practice.

Therefore, the effect of clay platelet dispersion and orientation on the barrier properties of polymer-clay nanocomposites has been studied in detail.[32,33]

With regard to the effect of sheet orientation, the layer order parameter is defined as

$$S = \tfrac{1}{2}(3\cos^2\theta - 1) \qquad \text{(Equation 1.3)}$$

where θ represents the angle between the direction of preferred orientation (**n**) and actual sheet orientation (**p**) as shown in Figure 1.7 (a)[32]. This function can range from 1 (θ=0), indicating perfect orientation of platy clay layers, to $-\tfrac{1}{2}$ ($\theta=\pi/2$), indicating perpendicular or orthogonal orientation, and a value of 0 for random orientation. The tortuosity factor is modified further to include the platelet orientation order S. The resulting relative permeability is given by

$$P_c/P_p = 1 / [1+(L/2W)\Phi(2/3)(S+\tfrac{1}{2})] \qquad \text{(Equation 1.4)}$$

The above expression reduces to Equation 1.2 when S=1 and converges approximately to the permeability of the pristine polymer when $S= -\tfrac{1}{2}$.

The effect of increasing aggregation while keeping a parallel platelet orientation is illustrated in Figure 1.7 (b)[32]. For single clay layers dispersed in the polymer matrix, the width is ~ 1 nm which allows for the maximum aspect ratio. In contrast, consider a case where aggregates composed of two silicate layers and an intercalated polymer layer are dispersed throughout the matrix. Now, the width increases to ~ 3 nm assuming that the polymer layer is 1 nm thick. Aggregates of four silicate sheets with three layers of intercalated polymer chains lead to an effective width of ~ 7 nm, thus dramatically increasing the relative permeability.

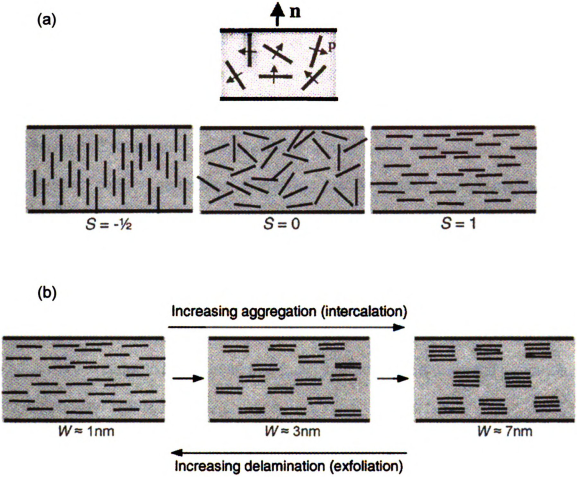

Figure 1.7 (a) Effect of sheet orientation on the relative permeability of exfoliated nanocomposites. The illustrations show the definition of the direction of preferred orientation (**n**) of the silicate layers and the actual orientation (**p**), and three values of the order parameter *S*= -½, 0, and 1. (b) Effect of incomplete exfoliation on the relative permeability. The illustrations show the effect of having one-, two-, and four-sheet aggregates dispersed throughout the matrix.[32]

1.4 Polymer-Carbon Nanotube Nanocomposites

Carbon nanotubes (CNTs) have attracted special attention as an ideal filler for polymer composites due to their exceptional mechanical properties (e.g. high modulus, stiffness and extensibility),[34,35] and high electrical[36,37] and thermal conductivity.[38,39] Currently, a variety of nanotube types is available, such as single-walled carbon nanotubes (SWNTs), double-walled carbon nanotubes (DWNTs), and multi-walled carbon nanotubes (MWNTs). When nanotubes are considered for reinforcement applications, it is important to address bundle formation because of intertubular van der Waals forces (Figure 1.8).[40] In order to facilitate CNTs dispersion/exfoliation, surface functionalization of the nanotubes is necessary in order to form strong interfacial interactions between the nanotube and the polymer matrix.[41-45]

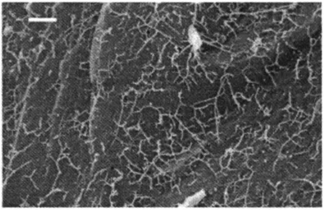

Figure 1.8 SEM micrograph showing a network of SWNT aggregates on the surface of a fractured nanotube-epoxy composite.[40]

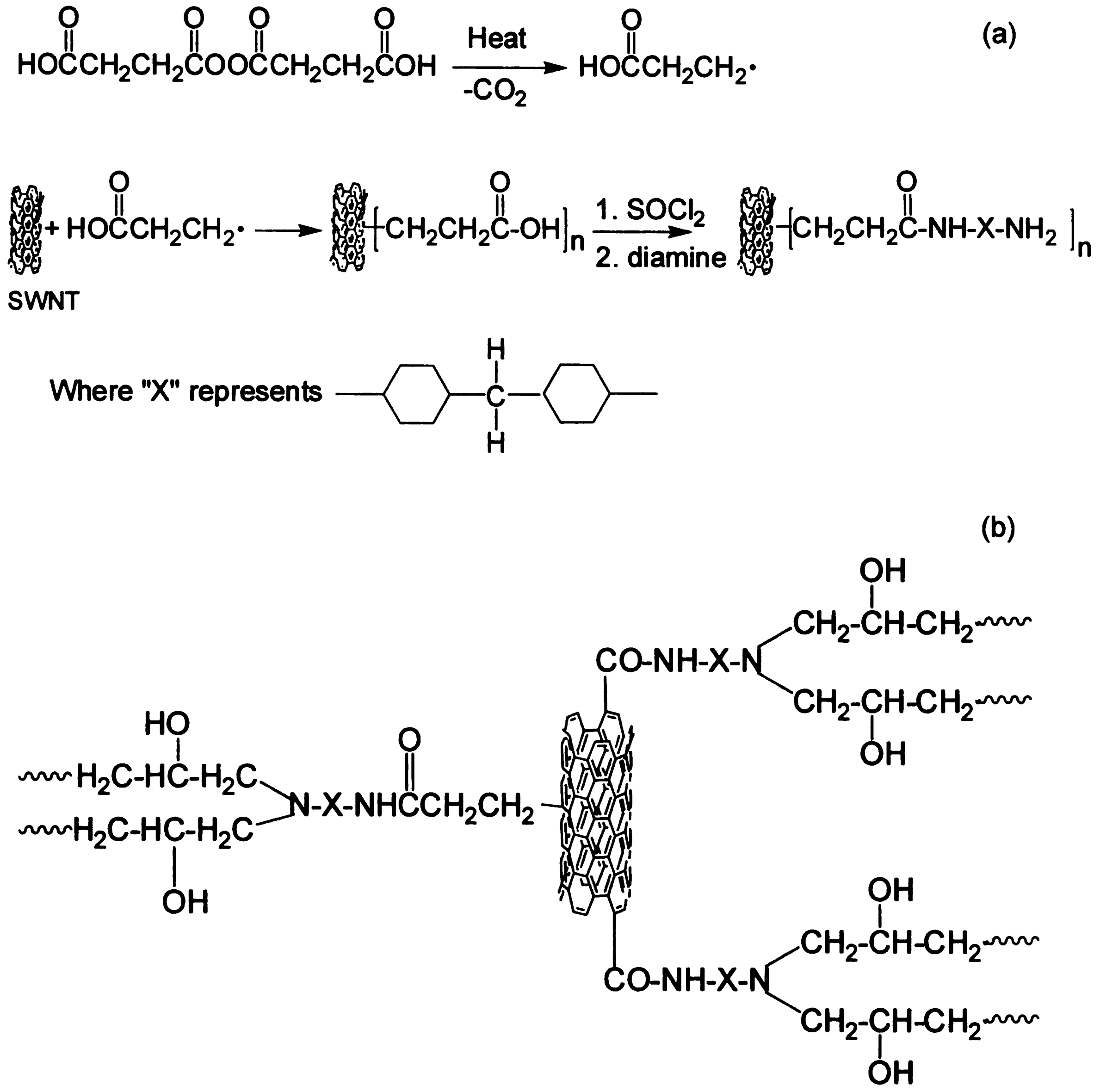

Figure 1.9 (a) Reaction scheme for the functionalization of SWNTs and (b) Integration of the functionalized SWNTs into an epoxy matrix.[42]

Wagner and co-workers reported a significant enhancement of mechanical properties of poly(vinyl alcohol) (PVA) composites with the addition of covalently functionalized SWNTs with multiple surface hydroxyl groups. The improvements are attributed to the strong hydrogen bonding at the polymer-nanotube interface.[45] In one study, a fully integrated nanotube-epoxy polymer composite with covalent chemical bonding between the matrix and functionalized SWNTs is reported.[42] Functionalized nanotubes were prepared through the reaction of diamines with alkylcarboxyl groups attached to the SWNTs sidewalls as shown in Figure 1.9 (a). The terminal amino groups attached to the nanotubes readily react with epoxy resin and thus serve as an additional curing agent. Therefore, nanotubes are covalently integrated into the matrix and become part of the cross-linked structure, rather than just a separate filler (Figure 1.9 (b)). At a loading of only 1 wt% functionalized SWNTs, the resulting epoxy composites demonstrate significant increase in tensile strength, Young's modulus and elongation-at-break by more than 25%, 30% and 30%, respectively. This also suggests higher toughness with respect to the neat epoxy. These observations support the theoretical and molecular simulation[46] predictions that load transfer from the matrix to the nanotubes can be effectively increased by the formation of covalent bonding at the interface. The simulations predict that the shear strength required for load transfer can be enhanced by more than one order of magnitude with the introduction of chemical bonds involving less than 1% of nanotube carbon atoms.

Although surface functionalization enables particle-matrix interactions to be controlled through a variety of organic groups attached to the carbon nanotubes, and as a consequence, to design nanotube-reinforced polymer composites, covalently functionalized carbon nanotubes are not good candidates for the improvement of composite conductivity, because strong tube-polymer adhesion produces weaker nanotube-nanotube contacts, which weakens the three-dimensional nanotube network.[47-49]

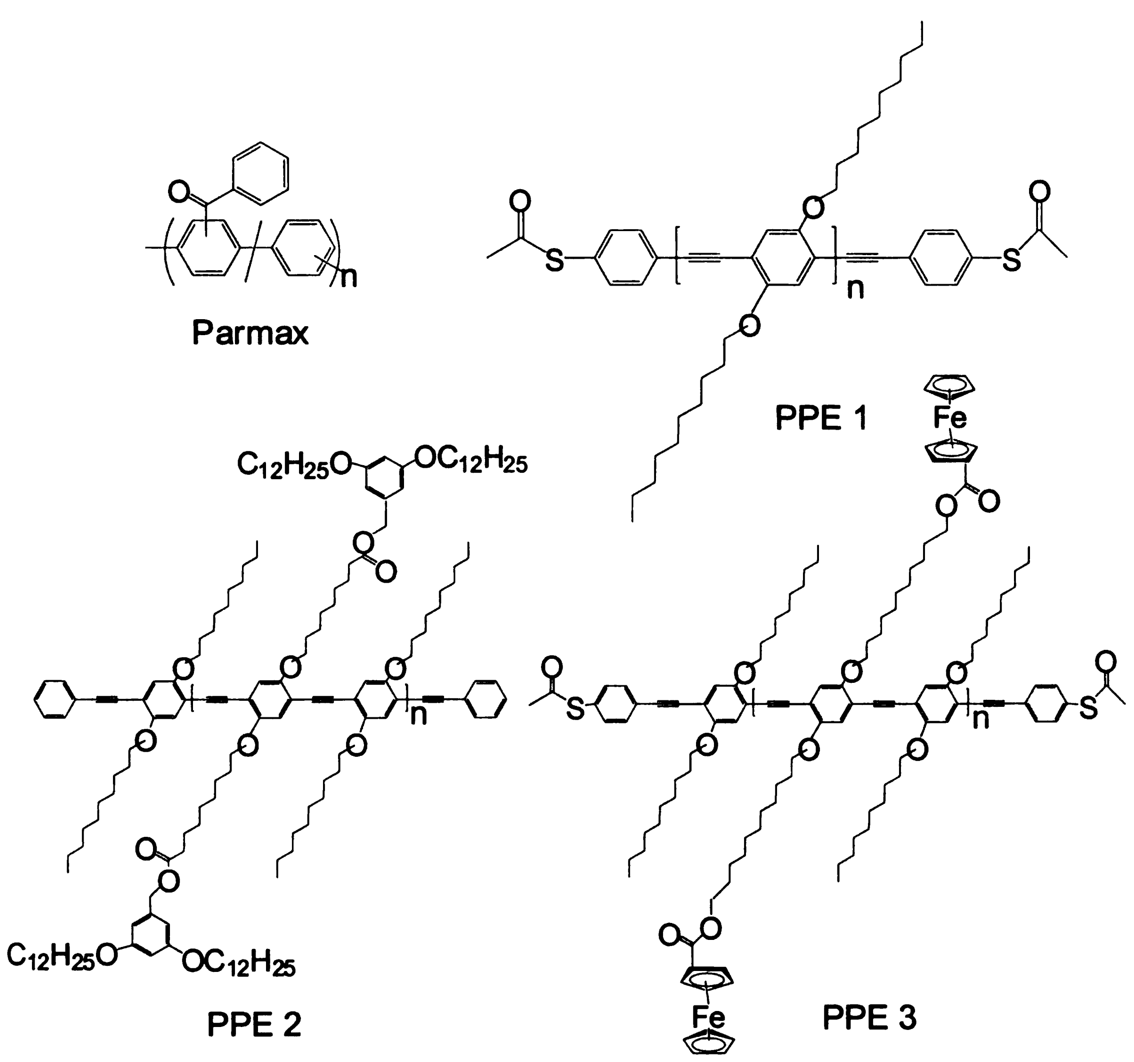

Figure 1.10 Chemical structures of the polymer matrix Parmax and poly(*p*-phenylene ethylene)s (PPEs) used for the surface modification of carbon nanotubes.[47]

For the first time, Chen and co-workers suggested non-covalently functionalized SWNTs as being crucial for achieving a simultaneous

Table 1.2 Electrical and mechanical properties of the films[47]

Film sample	Electric conductivity ($S \cdot m^{-1}$)	Young's modulus (GPa)	Tensile strength (MPa)
A	$< 10^{-11}$	3.9 ± 0.2	144 ± 8
B	0.42	5.3 ± 0.8	155 ± 9
C	0.56	5.9 ± 0.7	211 ± 7
D	28.6	5.0 ± 0.3	248 ± 8

improvement in mechanical and electrical properties of SWNT-polymer nanocomposites.[47] They used Parmax (Figure 1.10), poly(benzoyl-1,4-phenylene) -co-(1,3-phenylene), as the polymer matrix in this study because of its extraordinary mechanical strength and stiffness, inflammability, and high-temperature stability. They used three poly(*p*-phenylene ethylene)s (PPEs) (Figure 1.10) to non-covalently functionalize SWNTs and disperse SWNTs homogeneously in polymer matrix. Studies have shown that the backbone of PPE modifiers can bind irreversibly to carbon nanotube surfaces by π-stacking.[50,51] Four different composite film samples were prepared for this study: sample A is pure Parmax and samples B, C and D are Parmax composites with the addition of 2 wt% PPE 1, PPE 2 and PPE 3 functionalized SWNTs, respectively. As shown in Table 1.2, in comparison to sample B, sample C demonstrates a similar enhancement in electrical conductivity, but a more significant increase in tensile strength. The weak van der Waals' interactions exist for both samples, while the large, branched side chains in PPE 2 may increase mechanical interlocking. Furthermore, the PPE 3/Parmax interface exhibits the most dramatic effects on the tensile strength and electrical conductivity of the PPE-SWNT-Parmax composite, suggesting the best adhesion between PPE 3 and Parmax matrix as compared to that between PPE 1, 2 and Parmax. This is achieved through the π-π interactions between ferrocenyl groups in PPE 3 and Parmax.

More recently, a new approach to make conductive nanotube-filled polymer composites is to introduce clay into single-walled carbon nanotube/epoxy composites to assist nanotube dispersion without harming mechanical property.[48] It was found out that with only 0.05 wt% SWNT, electrical conductivity was increased by more than four orders of magnitude in combination with 0.2 wt% clay. This improvement in conductivity was accompanied by a slight increase in storage modulus. In addition, the percolation threshold for the nanocomposites was reduced from 0.05 wt% without clay to 0.01 wt% with the addition of clay. The most likely reason why clay helps SWNT network formation is that the nanotubes seem to interact more strongly with the negatively-charged montmorillonite layers than the epoxy polymer. This tube-clay interaction can be observed using partially polarized light in an optical microscope in Figure 1.11 (a): the epoxy matrix is in gray color, whereas clay is seen as bright clusters and SWNT is black. Almost all of the clay tactoids are surrounded by a SWNT network and the nanotubes are not observed in open areas that have little or no clay. Clay-assisted dispersion of carbon nanotubes is illustrated in Figure 1.11 (b). The limited improvement in composite mechanical properties might be caused by the inadequate exfoliation of the clay nanolayers.

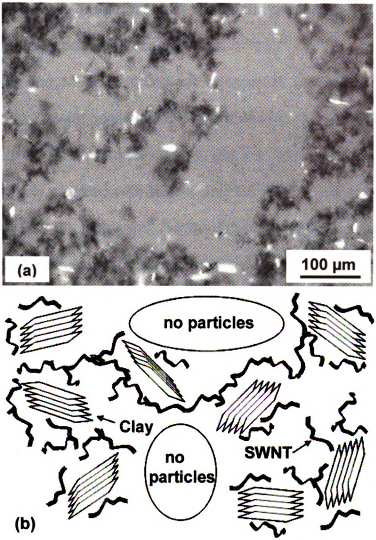

Figure 1.11 (a) Optical microscope image for composite containing 0.05 wt% SWNT and 2 wt% clay under partial polarized light condition, and (b) Schematic illustration of clay assisted dispersion of SWNTs.[48]

1.5 Polymer-Zeolite Nanocomposites

Zeolites are crystalline microporous materials that are widely used as catalysts for applications like the cracking of heavy oil fractions, cumene production, alkane hydroisomerization and fine chemicals synthesis.[52] Since the

1980s, there has been a great deal of interest in the preparation, characterization and application of polymer-zeolite composites.

Al-ghamdi and Mark[53] studied reinforcements of poly(dimethylsiloxane) (PDMS) by zeolite 3A with pore size of 3 Å and zeolite 13X with pore diameter of 10 Å, both with a cubic morphology and particle size of 1-5 *μm*. These two zeolites were simply blended with PDMS and found to improve the mechanical properties of the PDMS elastomers. But the effect was more dramatic for zeolite 13X with the larger pore size. Further characterization of such zeolite-reinforced PDMS elastomers by Wen and Mark[54] concluded that there was negligible penetration of the polymer into the zeolite pores, as suggested by the small-angle neutron scattering (SANS) results of the pure and zeolite-filled PDMS networks. Also, the superior reinforcement achieved by zeolite 13X might be attributed to its smaller particle size, rather than its larger pore size.

In the cases discussed above, the polymer is directly introduced into the zeolite confined structure. A different approach is to introduce monomers and subsequently polymerize monomers within channels to obtain the final composite materials.[55-57] In the first application of this approach, Frisch and Xue[55] added monomeric styrene to a desired amount of zeolite 13X in various ratios, followed by the addition of a benzoyl peroxide initiator for the polymerization of the styrene. In the presence of ethylene glycol dimethacrylate (EGDM) as a cross-linker, the cross-linked polystyrene (PS)/zeolite composite formed a fully interpenetrating polymer network (IPN) as no significant amount of cross-linked polystyrene chains was removed by extensive solvent extractions. In contrast, the linear PS chains and zeolites were considered to form a pseudointerpenetrating polymer network (PIPN) since half of the linear polymer could be removed after solvent extraction. According to the differential scanning calorimetry (DSC) measurements, an extracted sample of PIPNs exhibited no glass transition temperature T_g because the linear polymer chains situated in the internal pores of zeolite 13X, adopt a more extended, one dimensionally oriented conformation. This interpretation is consistent with Giannelis's observation that intercalated PS chains in silicate clay layers do not show a T_g characteristic of the pure polymer.[58]

Polymer-zeolite composites may provide economical, high performance gas separation membranes if interfacial voids at the molecular sieve/polymer interface can be eliminated.[59-63] Marand and co-workers fabricated mixed matrix membranes (MMMs) composed of aminopropyltriethoxysilane (APTES) surface modified zeolite L (ZL) covalently linked to a polyimide matrix containing carboxylic acid groups along the backbone.[61] Unlike zeolites employed in other MMM studies, zeolite L containing one-dimensional channel with an aperture of 7.1 Å can separate gas molecules by selective adsorption in addition to size exclusion. The channels contain cationic sites, which can interact with negatively charged or polar molecules.[64] As illustrated in Figure 1.12, the sorption capacity of the APTES-ZL is significantly lower than that of the pristine ZL, suggesting the possibility of pore blockage by the coupling agents. O_2 and N_2 permeability increases 13% and 24%, respectively, through the MMM when compared to the pure polyimide membrane. However, this results in a slight decrease in the

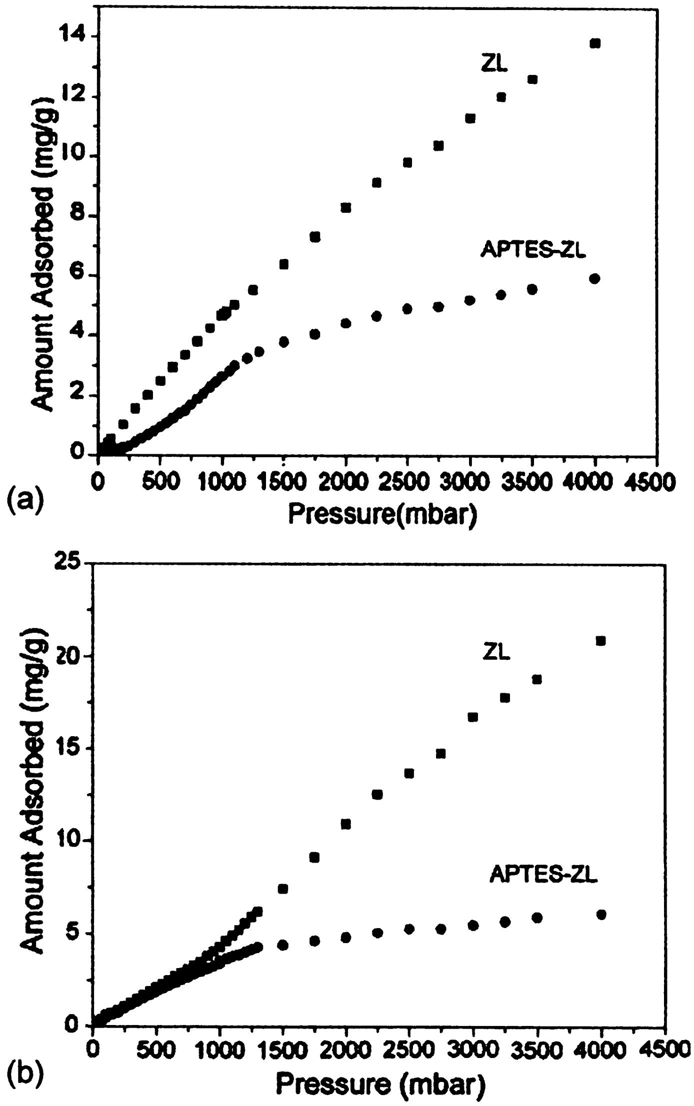

Figure 1.12 Gas sorption isotherms at 35°C for unmodified zeolite L (ZL) and modified zeolite L with APTES (APTES-ZL): (a) nitrogen and (b) oxygen.[61]

selectivity factor for O_2/N_2 from 4.8 to 4.5 because N_2 is expected to have higher sorption in zeolite L.

Yong et al. proposed a new method to fill the space between the polymer and zeolite particles by introducing 2,4,6-triaminopyrimidine (TAP) to form hydrogen bonds between the two phases instead of the surface treatment of zeolites.[62] The void-free PI/zeolite 13 X/TAP membrane showed higher permeability for He, N_2, O_2, CO_2, and CH_4 with little compromise in permselectivity as compared to the PI/TAP membrane. The PI/zeolite 4A/TAP membrance showed lower permeability but higher selectivity for all gases. These results could be explained by the different pore sizes in 13X and 4A zeolites. The 7.4 Å pore size of zeolite 13X, appears to be large enough for the facile penetration of all gases compared to the PI/TAP matrix. However, the 3.8 Å diameter of zeolite 4A is very close to the kinetic diameter of the gas molecules, which may provide the molecular-sieving effect.

A novel carbon/ZSM-5 nanocomposite membrane with high performace for oxygen/nitrogen separation is prepared by incorporating nano-sized ZSM-5 into the polyimide precursor.[63] Carbon membranes have an ultra-micropore structure with pore diameters of 3-5 Å, close to the diameters of O_2 and N_2. Thus, they are good candidates for air separation. But there's a strong trade-off relationship between the gas flux and selectivity because of the disordered pore structure and diffusion resistance in membranes. Zeolite ZSM-5 features uniform pores (5.5 Å) and can endure high temperature treatment. Therefore, the channels in zeolite will remain intact to some degree and function as continuous transport pathways for gas species as shown in Figure 1.13. Table 1.3 shows the permeation properties of the pure carbon membrane and the carbon nanocomposite membranes incorporated with different zeolite loadings.[63] It's clear that the permeabilities of O_2 and N_2 increase substantially at higher zeolite loadings, indicating that porous zeolite ZSM-5 helps to minimize the resistance in the gas diffusion process. In addition, the composite membranes retain good O_2/N_2 selectivity from 12 to 14.4, which can be mainly attributed to the carbon matrix, because ZSM-5 is a non-selective zeolite with a pore size greater than oxygen and nitrogen.

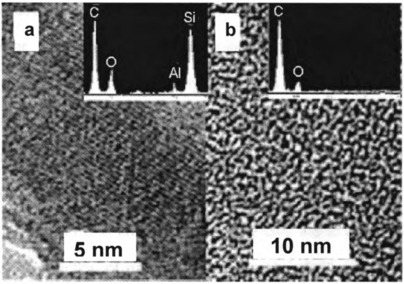

Figure 1.13 High-resolution TEM images of carbon/ZSM-5 composite membrane with 9.1 wt% of ZSM-5 (denoted PIZ2): (a) ZSM-5 embedded in membranes, (b) carbon phase in membranes.[63]

Table 1.3 Permeation properties of carbon/ZSM-5 membranes at 298K[63]

	Flux/Barrers[a]		Selectivity
Membrane	O_2	N_2	O_2/N_2
PI (polymeric membrane)	0.16	0.04	4.2
PI (carbon membrane)	2.21	0.16	13.8
PIZ1 (4.8 wt% ZSM-5)	70.0	5.85	12
PIZ2 (9.1 wt% ZSM-5)	431.0	30.0	14.4
PIZ3 (16.7 wt% ZSM-5)	499.0	39.6	12.6

[a] 1 Barrer = 1×10^{-10} cm^3 (STP) cm/cm^2 s cmHg

1.6 Research Goals and Significance

In contrast to the exponential reduction in permeability expected on the basis of the Nielson's model for composites embedded with oriented lamellar platelets, a more typical 2- to 4-fold reduction in gas permeability is usually achieved by polymer-clay nanocomposites owing to the partial exfoliation and disalignments of clay nanolayers in the polymer. This thesis demonstrates a new strategy that substantially enhances the barrier properties of both thermoset epoxy polymer and thermoplastic polyolefins by sandwiching novel self-supported clay fabric films between polymer sheets. The paper-like clay films are prepared by casting suspensions of the clay onto glass plates, allowing the suspensions to evaporate and then peeling away the film. Various homoionic organic and homostructured and heterostructured mixed organic-inorganic ion montmorillonite (MMT) and fluorohectorite (FH) clay fabric films were prepared by ion-exchange reaction of naturally occurring Na^+-MMT and synthetic Li^+-FH with a variety of organic modifiers in order to afford adequate interfacial adhesion with the polymer matrices. Thermoplastic polyolefin-clay fabric film composites were fabricated by sandwiching the resulting clay films between two sheets of high density polyethylene (HDPE) films through a hot-pressing process. The sandwiched composites exhibit more than 30-fold decrease in O_2 transmission rate with respect to the pure HDPE film. In the case of thermoset system, impregnating the self-supported clay papers with epoxy pre-polymers successfully leads to composite films with more than 2-3 orders of magnitude reduction in O_2 permeability in comparison to the pristine epoxy matrix.

Another objective of this thesis is to investigate the synthesis of a new phase mixture of saponite and cancrinite. Saponite (denoted SAP) belongs to 2:1 structured smectite clay, whereas cancrinite (denoted CAN) is a porous zeolite with the natural composition $Na_6Ca[AlSiO_4]_6CO_3(H_2O)_2$. The cancrinite framework topology is shown in Figure 1.14. Synthetic Mg-saponite has potential applications as reinforcement agents for themoset epoxy polymers[29] and as acid catalysts for alkylation[65]. However, the available synthetic routes are cost intensive.[65] In an effort to develop a more efficient and cost-effective synthesis of Mg-saponite, sodium hydroxide instead of urea is used as the base source. Pure delaminated SAP platelets were synthesized at low alkalinity at 90°C. Interestingly, upon increasing the alkalinity, cancrinite was co-crystallized together with saponite. Also, pure-phase cancrinte with dimensions ranging from several hundred nm to several μm in length was achieved by varying synthetic conditions.

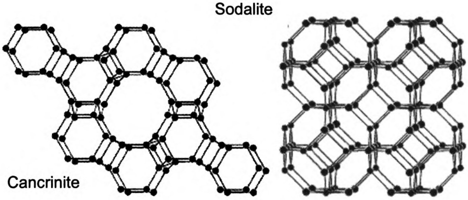

Figure 1.14 Comparison between the framework topologies of cancrinite and sodalite. The vertices represent the positions of Si and Al in the framework and the edges represent the positions of bridging oxygen atoms.

It has been found that synthetic Mg-saponite can improve the tensile properties of both rubbery and glassy epoxy polymers without the need for the organic modification of the clay surface.[29] Microporous cancrinite may also be promising candidates for reinforcing epoxy polymers, considering that cancrinite can be co-crystallized along with Mg-saponite during the saponite synthesis. Therefore, the reaction conditions (e.g. alkalinity, reaction temperature, and duration) are explored in the present work with the objective to form small crystals of cancrinite (~ 100 nm) with large external surface area and high pore volume. These particle properties will facilitate the uniform dispersion of cancrinite particles in epoxy matrices. Moreover, as part of the exploration of the synthesis of cancrinite with a small particle size, we find that co-crystallization of sodalite, another mineral silicate with zeolite structure (c.f. Figure 1.14), takes place in some cases.

Only a few studies have been reported on zeolite-epoxy composites,[66-69] wherein the focus was on the effect of natural zeolite particles on the curing kinetics and mechanical properties of the epoxy system. With increasing zeolite content, tensile strength decreased dramatically, while Young's modulus increased, which is the result typical of conventional composites.[66]

The present work aims to use synthetic cancrinite and sodalite as reinforcing agents for thermoset epoxy polymers owing to their small particle size, large surface area and high pore volume. The results show that the tensile strength, modulus and toughness of the composites are simultaneously enhanced without the need for an organic surface modification of zeolites. This finding represents the first example for which the mechanical properties of glassy epoxy composite are all improved through the use of a microporous zeolite as a functional inorganic filler. Also, the properties of epoxy nanocomposites reinforced by microporous cancrinite and sodalite are compared with those of nanocomposites made from organo-clay nanoparticles, carbon nanotubes and mesoporous silicas.

References

(1) Boccara, N.; Daoud, M. *Physics of Finely Divided Matter*: New York, **1985**.

(2) Ray, S. S.; Okamoto, M. *Prog. Polym. Sci.* **2003**, *28*, 1539.

(3) Jana, S. C.; Pattanayak, A. *Polymer* **2005**, *46*, 5183.

(4) Pinnavaia, T. J.; Lan, T.; Kaviratna, P. D. *Chem. Mater.* **1995**, *7*, 2144.

(5) Pinnavaia, T. J.; Lan, T.; Kaviratna, P. D. *J. Phys. Chem. Solids* **1996**, *57*, 1005.

(6) Pinnavaia, T. J.; Lan, T. *Chem. Mater.* **1994**, *6*, 2216.

(7) Park, I. *Diploma Thesis*, Michigan State University, **2006**.

(8) Jana, S. C.; Park, J. H. *Macromolecules* **2003**, *36*, 2758.

(9) Tyan, H. L.; Leu, C. M.; Wei, K. H. *Chem. Mater.* **2001**, *13*, 222.

(10) Leu, C. M.; Wu, Z. W.; Wei, K. H. *Chem. Mater.* **2002**, *14*, 3016.

(11) Tyan, H. L.; Liu, Y. C.; Wei, K. H. *Chem. Mater.* **1999**, *11*, 1942.

(12) Agag, T.; Koga, T.; Takeichi, T. *Polymer*, **2001**, *42*, 3399.

(13) Zhang, Y. H.; Dang, Z. M.; Fu, S. Y.; Xin, J. H.; Deng, J. G.; Wu, J. T.; Yang, S. Y.; Li, L. F.; Yuan, Q. *Chem. Phys. Lett.* **2005**, *401*, 553.

(14) Jiang, L. Y.; Leu, C. M.; Wei, K. H. *Adv. Mater.* **2002**, *14*, 426.

(15) Liff, S. M.; Kumar, N.; McKinley, G. H. *Nature Mater.* **2007**, *6*, 76.

(16) Vaia, R. A.; Maguire, J. F. *Chem. Mater.* **2007**, *19*, 2736.

(17) Cabedo, L.; Gimẽnez, E.; Lagaron, J. M.; Gavara, R.; Saura, J. *Polymer* **2004**, *45*, 5233.

(18) Manias, E.; Touny, A.; Wu, L.; Strawhecker, K.; Lu, B.; Chung, T. C. *Chem. Mater.* **2001**, *13*, 3516.

(19) Baker, A. M. E.; Windle, A. H. *Polymer* **2001**, *42*, 667.

(20) Kato, M.; Usuki, A.; Okada, A. *J. Appl. Polym. Sci.* **1997**, *66*, 1781.

(21) Kawasumi, M.; Hasegawa, N.; Kato, M.; Usuki, A. *Macromolecules* **1997**, *30*, 6333.

(22) Reichert, P.; Nitz, H.; Klinke, S.; Brandsch, R.; Thomann, R.; Mülhaupt, R. *Macromol. Mater. Eng.* **2000**, *275*, 8.

(23) Manias, E.; Touny, A.; Wu, L.; Lu, B.; Strawhecker, K.; Gilman, J. W.; Chung, T. C. *Polym. Mater. Sci. Eng.* **2000**, *82*, 282.

(24) Gintert, M. J.; Jana, S. C.; Miller, S. G. *Polymer* **2007**, *48*, 4166.

(25) Manias, E.; Touny, A.; Wu, L.; Lu, B.; Chung, T. C. *Macromolecules*, in press.

(26) Vaia, R. A.; Giannelis, E. P. *Macromolecules* **1997**, *30*, 7990.

(27) Vaia, R. A.; Giannelis, E. P. *Macromolecules* **1997**, *30*, 8000.

(28) Pinnavaia, T. J.; Shi, H.; Lan, T. *Chem. Mater.* **1996**, *8*, 1584.

(29) Xue, S.; Pinnavaia, T. J. *Micropor. Mesopor. Mater.* **2008**, *107*, 134.

(30) Vogels, R. J. M. J.; Breukelaar, J.; Kloprogge, J. T. *Clays Clay Miner.* **1997**, *45*, 1.

(31) Nielson, L. E. *J. Macromol. Sci. (Chem.)* **1967**, *A1*, 929.

(32) Bharadwaj, R. K. *Macromolecules* **2001**, *34*, 9189.

(33) Lu, C.; Mai, Y-W. *Phys. Rev. Lett.* **2005**, *95*, 088303.

(34) Coleman, J. N.; Khan, U.; Gun'ko, Y. K. *Adv. Mater.* **2006**, *18*, 689.

(35) Ajayan, P. M. *Chem. Rev.* **1999**, *99*, 1787.

(36) Tans, S. J.; Verschueren, A. R. M; Dekker, C. *Nature* **1998**, *393*, 49.

(37) Postma, H. W. C.; Teepen, T.; Yao, Z.; Grifoni, M. Dekker, C. *Science* **2001**, *293*, 76.

(38) Pop, E.; Mann, D.; Wang, Q.; Goodson, K.; Dai, H. *Nano. Lett.* **2006**, *6*, 96.

(39) Berber, S.; Kwon, Y. K.; Tomanek, D. *Phys. Rev. Lett.* **2000**, *84*, 4613.

(40) Ajayan, P. M.; Schadler, L. S.; Giannaris, C.; Rubio, A. *Adv. Mater.* **2000**, *12*, 750.

(41) Liang, F.; Beach, J. M.; Rai, P. K.; Guo, W.; Hauge, R. H.; Matteo, P.; Smalley, R. E.; Billups, W. E. *Chem. Mater.* **2006**, *18*, 1520.

(42) Zhu, J.; Peng, H.; Rodriguez-Macias, F.; Margrave, J. L; Khabashesku, V. N.; Imam, A. M.; Lozano, K.; Barrera, E. V. *Adv. Funct. Mater.* **2004**, *14*, 643.

(43) Warren, G. L.; Sun, L.; Hadjiev, V. G.; Davis, D.; Lagoudas, D.; Sue, H.-J. *J. Appl. Polym. Sci.* **2009**, *112*, 290.

(44) Zhu, J.; Kim, J.; Peng, H.; Margrave, J. L.; Khabashesku, V. N.; Barrera, E. V. *Nano Lett.* **2003**, *3*, 1107.

(45) Liu, L.; Barber, A. H.; Nuriel, S.; Wagner, H. D. *Adv. Funct. Mater.* **2005**, *15*, 975.

(46) Frankland, S. J. V.; Caglar, A.; Brenner, D. W.; Griebel, M. *J. Phys. Chem. B* **2002**, *106*, 3046.

(47) Chen, J.; Ramasubramaniam, R.; Xue, C.; Liu, H. *Adv. Funct. Mater.* **2006**, *16*, 114.

(48) Liu, L.; Grunlan, J. C. *Adv. Funct. Mater.* **2007**, *17*, 2343.

(49) Gojny, F. H.; Wichmann, M. H. G.; Fiedler, B.; Kinloch, I. A.; Bauhofer, W.; Windle, A. H.; Schulte, K. *Polymer* **2006**, *47*, 2036.

(50) Chen, J.; Liu, H.; Weimer, W. A.; Halls, M. D.; Waldeck, D. H.; Walker, G. C. *J. Am. Chem. Soc.* **2002**, *124*, 9034.

(51) Chen, J.; Ramasubramaniam, R.; Liu, H. *Mater. Res. Soc. Symp. Proc.* **2005**, *858E*, HH12.4.

(52) Corma, A. *Chem. Rev.* **1995**, 95, 559.

(53) Al-ghamdi, A. M. S.; Mark, J. E. *Polym. Bull.* **1988**, *20*, 537.

(54) Wen, J.; Mark, J. E. *J. Mater. Sci.* **1994**, *29*, 499.

(55) Frisch, H. L.; Xue, Y. *J. Polym. Sci. Polym. Chem. Ed.* **1995**, *33*, 1979.

(56) Frisch, H. L.; Maaref, S.; Xue, Y.; Beaucage, G.; Pu, Z.; Mark, J. E. *J. Polym. Sci. Polym. Chem. Ed.* **1996**, *34*, 673.

(57) Cooney, R. P.; Millar, G. J.; Lewis, A. R.; Bowmaker, G. A. *J. Mater. Chem.* **1993**, *3*, 867.

(58) Vaia, R. A.; Ishii, H.; Giannelis, E. P. *Chem. Mater.* **1993**, *5*, 1694.

(59) Uytterhoeven, J. B.; Vankelecom, I. F. J.; Merckx, E.; Luts, M. *J. Phys. Chem.* **1995**, *99*, 13187.

(60) Koros, W. J.; Zimmerman, C. M.; Singh, A. *J. Membr. Sci.* **1997**, *137*, 145.

(61) Pechar, T. W.; Kim, S.; Vaughan, B.; Marand, E.; Tsapatsis, M.; Jeong, H. K.; Cornelius, C. J. *J. Membr. Sci.* **2006**, *277*, 195.

(62) Yong, H. H.; Park, H. C.; Kang, Y. S.; Won, J.; Kim, W. N. *J. Membr. Sci.* **2001**, *188*, 151.

(63) Liu, Q.; Wang, T.; Qiu, J.; Cao, Y. *Chem. Commun.* **2006**, 1230.

(64) Tsapatsis, M.; Lovallo, M.; Okubo, T.; Davis, M.; Sadakata, M. *Chem. Mater.* **1995**, *7*, 1734.

(65) Vogels, R. J. M. J.; Kerkhoffs, M. J. H. V.; Geus, J. W. *Stud. Surf. Sci. Catal.* **1995**, *91*, 1153.

(66) Kim, S.-W.; Shim, M.-J.; Lee, J.-Y. *Polym. Eng. Sci.* **1999**, *39*, 1993.

(67) Kim, S.-W.; Shim, M.-J.; Lee, J.-Y. *J. Mater. Sci.* **2001**, *36*, 4405.

(68) Kim, S.-W.; Shim, M.-J.; Lee, J.-Y. *Mater. Chem. Phys.* **1997**, *48*, 36.

(69) Narayanan, S.; Palaniappan, S.; Sreedhar, B. *Polym. Adv. Technol.* **2002**, *13*, 459.

CHAPTER 2

Thermoplastic Polyolefin-Clay Fabric Film Composites with High Barrier Property towards Oxygen and Petroleum Fuel Components

2.1 Introduction

Since the late 1980s much research has focused on developing methods to incorporate fully exfoliated smectite clays into polymers to enhance mechanical and barrier properties.[1] However, it has been a scientific challenge to achieve the exfoliation of the clay nanolayers and even intercalated morphologies in polymer matrices have been difficult to obtain, particularly for thermoplastic polyolefins. The highly hydrophobic character of polyolefins prevents the development of adequate physical binding to the aluminosilicate surfaces of smectite clays. Two methods are often used to improve the interfacial interactions between two phases: (i) the surface chemistry of clays is fine-tuned by ion-exchange reaction with cationic organic surfactants such as alkylammonium ions, and (ii) polar maleic anhydride (MA)-grafted polyolefins are introduced in the formulations as compatibilizers.[2-10] MA-grafted polyolefins are typically characterized by very complicated molecular structures due to many side reactions,[11,12] including severe chain degradation during the free radical grafting process, as well as many impurities. An alternative approach is to use reactive chain transfer agents to prepare end-functionalized polyolefins containing a terminal functional group (OH, NH_2, COOH, anhydride, etc.), while maintaining a well-controlled polymer molecular weight and narrow molecular weight and composition distributions.[7,13]

Clay platelet particles enhance the barrier properties of polymers according to a tortuous path model developed by Nielsen.[14] In the model the impermeable clay nanolayers retard the transport of diffusing species such as oxygen or water vapor. The magnitude of barrier improvement strongly depends on the aspect ratio, volume fraction, and the state of dispersion and orientation of the platy inorganic particles. In contrast to the expected orders of magnitude reduction in permeability, a 2-4-fold reduction in permeation rates is more typical owing to the limited exfoliation and dis-alignment of the individual clay layers. The oxygen transmission rate of the epoxy matrix was reduced 1.25-4 times at 1-5 vol% of organoclay loading.[15] Long alkylammonium ions enhance the polymer intercalation but increase the oxygen permeability coefficient, most likely due to the phase separation at the interface between the polymer and the layered silicates. Composites made from ethoxylated short chain alkylammonium-montmorillonite exhibit the best oxygen barrier properties. It has been suggested that the functional –OH groups in the ethoxylated alkylammonium ions may react with the epoxy resin, energetically favoring the partial exfoliation of clay platelets with the entropically unfavorable small d-sapcings. A recent study[16] on the barrier properties of olefinic nanocomposites showed a 300-fold improvement in barrier properties was achieved due to the strong interfacial interaction between the wax and the organoclay surface. It was also found out that phase separation happened with the large difference between the freezing points of the polymer and organoclay, leading to the decrease in the magnitude of barrier improvements.

This research is focused on applying clay fabric film nanotechnology to thermoplastic polymer systems for automotive applications, particularly for the manufacturing of automotive fuel tanks for both conventional and flex-fuel automotive vehicles. Our recent study[17,18] on the oxygen barrier properties of epoxy-clay fabric film composites proposed a new strategy for achieving high barrier performace by impregnating the self-supported clay papers with epoxy pre-polymer. We successfully achieved 2-3 orders of magnitude reduction in O_2 permeability in comparison to the pristine polymer. The present investigation of oxygen barrier properties of high density polyethylene (HDPE)-clay fabric film composites exhibits more than 30-fold decrease in O_2 transmission rate with respect to the pure HDPE film. The magnitude of barrier improvements of polyolefin system is lower than that of the epoxy system, which can be explained by the fact that polyethylene chains can only block interparticle voids on the external surface of the clay films, unlike the epoxy system wherein the epoxy monomer and curing agent may diffuse into the interlayers of the clay film, as well as block the voids formed between clay particle edges upon curing. Measurements carried out in collaboration with Central Laboratory of Ford Motor Company have shown that the transmission rates of the HDPE-clay fabric film composites can be reduced to about one-sixth with regard to three petroleum fuel components: toluene, isooctane and ethanol.

2.2 Experimental

2.2.1 Materials

PGW Na^+-montmorillonite (Na^+-MMT) with a cation exchange capacity (CEC) of 100 meq/ 100 g was provided by Nanocor Inc.. A synthetic Li^+-fluorohectorite clay (Li^+-FH) with a CEC similar to that of PGW montmorillonite was purchased from Corning Inc.. All other chemicals were purchased from Aldrich Chemical Co. and used without further purification.

2.2.2 Preparation of Homoionic and Mixed-ion Clay Fabric Films

Homoionic inorganic Na^+-montmorillonite and Li^+-fluorohectorite clay films were made by preparing a 5 wt% homogeneous aqueous colloidal suspension of clay powders, then casting the suspension on a flat glass substrate, followed by drying in air for 1 day at room temperature. Continuous and self-supported clay fabric films were carefully peeled off the glass plate.

Homoionic organo-clay films and mixed inorganic-organic clay films were prepared by ion exchange of aqueous inorganic clay suspension with the desired amounts of onium ions. The ion-exchange reaction was carried out for 24-48 h at ambient temperature. The exchanged clay were isolated by centrifugation and washed with deionized water 3-4 times until free of Na^+, then followed by casting and drying in air at room temperature.

2.2.3 Hot-pressing the Organoclay Film with HDPE Sheets

An organoclay film approximately 8 cm x 8 cm was placed between two sheets of HDPE film (6 inch x 6 inch) and the assembly placed at the center of two flat Taflon-coated steel sheets used to prevent sticking. A sandwich-type composite film was subsequently made in a Tetrahedron Press Instrument using a hot-pressing procedure, wherein the sheets were heated to 270-330°F at a rate of 30°F/min under an applied pressure of 4 kPs, followed by cooling down to the room temperature at the same rate. The dwell time at the maximum temperature and pressure was normally 6 min.

2.2.4 Characterization and Testing of Clay Films and HDPE – Clay Film Composites

X-ray diffraction (XRD) patterns were obtained on a Rigaku rotaflex 200B diffractometer equipped with Cu Kα X-ray radiation and a curved crystal graphite monochromator, operating at 45 KV and 100 mA. Samples of the clay films were prepared by mounting the films on glass X-ray sample holders.

Thermogravimetric analyses (TGA) of the clay films were performed using a Cahn TG System 121 Analyzer. The clay films were cut into small pieces, which were heated to 800°C at a rate of 5°C/min under air flow. The compositions of clay films were determined by CHN chemical analysis and TGA.

Oxygen permeability measurements were performed on a Mocon Ox-tran 2/60 oxygen permeability instrument with 100% oxygen as test gas. The specimens tested were the pristine HDPE polymer with an average thickness of ~0.06 mm (~2.36 mil), and the HDPE – clay fabric film composites with an average thickness of ~0.14 to ~0.16 mm.

The fuel permeation tests of pristine polymeric and composite materials were carried out by the Central Laboratory of Ford Motor Company. The permeation measurements refer to three different test fuels: ethanol, isooctane and toluene at 40ºC.

2.3 Results and Discussion

2.3.1 Composition and Structural Properties of Homoionic and Mixed-ion Clay Fabric Films

The formation of self-supported smectite clay films depends on the ability of clay particles to disperse homogeneously with a high degree of exfoliation in aqueous suspensions. Figure 2.1 shows X-ray patterns of Na^+-montmorillonite and Li^+-fluorohectorite clay films and pristine Na^+-montmorillonite powders, respectively. As expected, the interlayer spacings (001 peak, 12.3 Å) are the same for the powder and oriented film form of the clay. However, it's clear that 001 peak of the montmorillonite film sample exhibits more than ten times higher intensity than that of the powder, indicating that the clay nanolayers are highly oriented along the direction perpendicular to the surface of the film. This orientation of the layers is realized by the restacking of exfoliated individual clay platelets in the colloidal suspensions when casted on the glass plate. The 001 peak of the Li^+-fluorohectorite film is 8 times more intense than that of Na^+-montmorillonite film as shown in Figure 2.1. The higher degree of platelet orientation may be caused by the large aspect ratio of the fluorohectorite platelets, which is over ten times that of montmorillonite particles and facilitates more efficient nanolayer alignments. Homoionic inorganic Na^+-montmorillonite and Li^+-fluorohectorite clay fabric films are self-supported, smooth, and semi-transparent. Moreover, the Li^+-flurohectorite fabric film is very robust paper-like material and much more flexible than the Na$^+$-montmorillonite film.

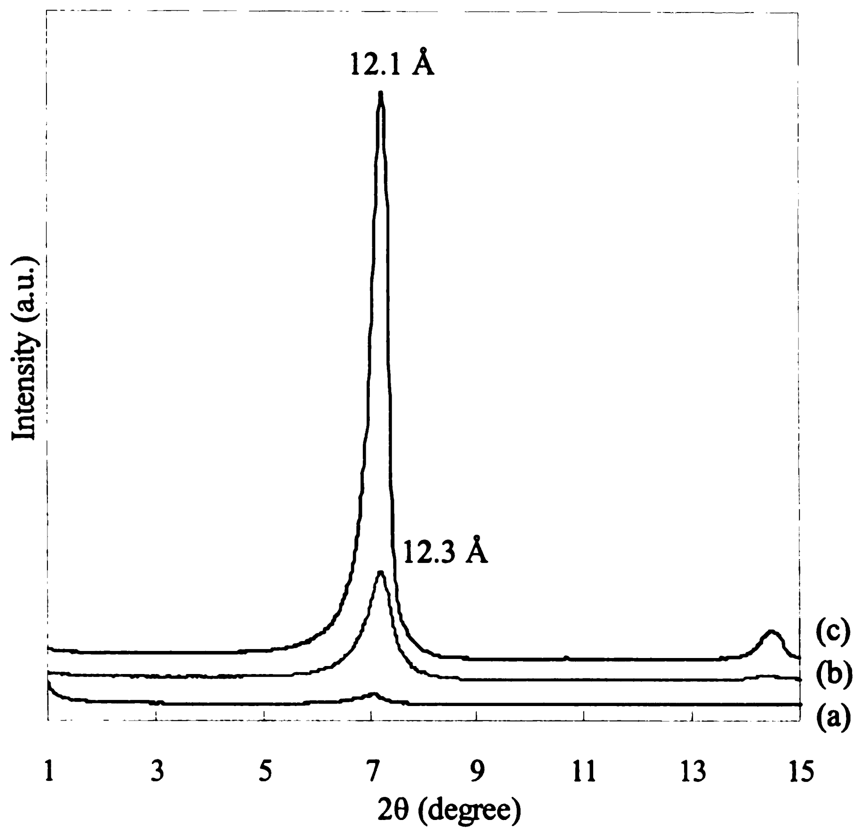

Figure 2.1 X-ray diffraction (XRD) patterns of (a) Na$^+$-montmorillonite clay powders, (b) Na$^+$-montmorillonite clay fabric film and (c) Li$^+$-fluorohectorite clay fabric film.

Na$^+$-MMT and Li$^+$-FH clays are hydrophilic due to the inorganic cations situated on the basal surface of the layered silicates. However, the polyethylene polymer is exclusively hydrophobic. In order to match the polarity of the clay with the polymer matrix, ion-exchange of inorganic clays with cationic surfactants is necessary. Homoionic organic and heterostructured mixed inorganic-organic ion clay fabric films using different onium ions were prepared to afford adequate interfacial adhesion with the thermoplastic polyolefin. The X-ray basal spacings for the clay films containing betaine, choline, and cetyltrimethylammonium (CTA^+) ions as the organic modifiers are provided in Table 2.1. Representative XRD patterns of some organo-MMT fabric films are shown in Figure 2.2.

Table 2.1 Basal spacings of homoionic and mixed-ion montmorillonite and fluorohectorite clay fabric films

clay sample designation	organic modifier	onium ion (%) [a]	basal spacings d_{001} (Å)	description
Na^+-MMT (PGW)	-	-	12.3	continuous film
Na^+/BET_{100}-MMT	betaine	100	14.3	continuous film
Na^+/BET_{150}-MMT	betaine	150	14.3, 18.7	continuous film
Na^+/BET_{200}-MMT	betaine	200	18.7	continuous film
$choline_{100}$-MMT	choline	100	14.1	continuous film
Na^+/CTA^+_{42}-MMT	CTA	42	27.8, 15.1	continuous film
Li^+-FH	-	-	12.1	continuous film
$choline_{100}$-FH	choline	100	13.8	continuous film
Li^+/CTA^+_{40}-FH	CTA	40	27.1, 13.5, 12.2	continuous film

[a] The percent onium ion-exchange represents the extent to which the ion-exchange sites of the clay have been replaced by onium ions; the reported values were determined by elemental or TGA analysis.

Betaine $(CH_3)_3N^+CH_2COO^-$ is a zwitterionic surfactant and doesn't replace inorganic cations because of its electrically neutral structure. Instead, betaine co-exists with Na^+ or Li^+ ions in the clay layers. Intercalated betaine arranged a monolayer and bilayer structure in the gallery at 100% and 200% equivalent amounts, respectively. Phase segregation happened at a loading of 150% equivalents, wherein both monolayer and bilayer orientations of betaine molecules were observed in terms of two basal spacings. The long-chain

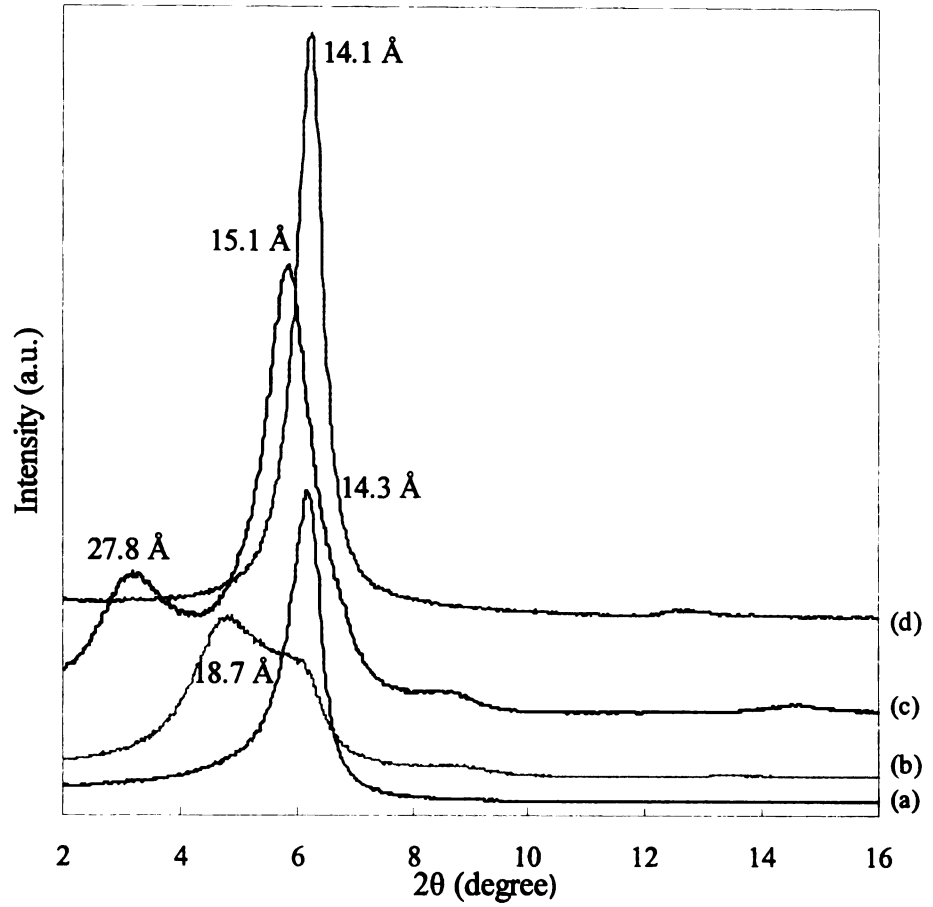

Figure 2.2 X-ray diffraction (XRD) patterns of (a) Na^+/BET_{100}-MMT, (b) Na^+/BET_{150}-MMT, (c) Na^+/CTA^+_{42}-MMT and (d) $choline_{100}$-MMT clay fabric films.

cetyltrimethylammonium (CTA^+) ion results in a large basal spacing of 27.8 Å for the mixed-ion clay film containing 42 mol% CTA^+ and 58 mol% Na^+ ions (denoted as Na^+/CTA^+_{42}-MMT). This spacing can be attributed to the clay gallery interlayered by paraffin-like structured onium ions. However, for the additional peak corresponding to the lower basal spacing of 15.1 Å, the onium ions adopt a monolayer orientation. Therefore, segregation of onium ions occurs in the clay film due to the different orientation of alkyl surfactants in the clay interlayers.

Homoionic-choline exchanged montmorillonite and fluorohectorite films have only one d-spacing of about 14 Å. The segregation of the organic and inorganic exchange cations into separate galleries is observed for the 40% CTA^+ exchanged Li^+-fluorohectorite film. Basal spacings of 27.1 Å and 13.5 Å suggest the galleries are interlayered by paraffin-like and monolayer structured alkylammonium ions, respectively. The diffraction peak at 12.2 Å can be attributed to the inorganic phase exclusively intercalated by Li^+ ions. The segregation of the ions is driven by the differences in the solvation properties of the two very different types of cations.

Compared with the pristine Na^+-MMT clay film, betaine modified Na^+-MMT is much more flexible, which is not observed with other partially or fully exchanged organo-MMT films. Betaine penetrates into the clay interlayers and adopts a monolayer or bilayer orientation in clay films. At the same time, betaine molecules might act as a binder as well and occupy the spaces formed between the platy clay particle edges. The edges of clay platelets are positively charged and can undergo electrostatic interaction with COO^- groups in betaine. Therefore, the attractive flexible property of BET/Na^+-MMT film can be attributed to a unique nanostructure, in which densely packed clay layers are reinforced by the soft betaine molecules between the clay platelets.

Figure 2.3 showed the thermogravimetric analysis (TGA) curves of Na^+-MMT and Na^+/CTA^+_{42}-MMT clay films. In both cases, the weight loss in the range of 25 to 130°C is due to the evaporation of water adsorbed on the clay surfaces or in the clay interlayers. Dehydroxylation of the inner 2:1 lattice hydroxyl groups takes place around 600°C. The thermal decomposition of $(CH_3)_3N^+(CH_2)_{15}CH_3$ starts around 220°C. Therefore, the HDPE melt-mixing temperature won't cause the Hofmann degradation of alkylammonium ions. The initial thermal degradation temperature of CTAB powder is 170°C. The increased thermal stability of onium ions in the clay can be explained by the strong electrostatic interaction with negatively charged silicate layers.

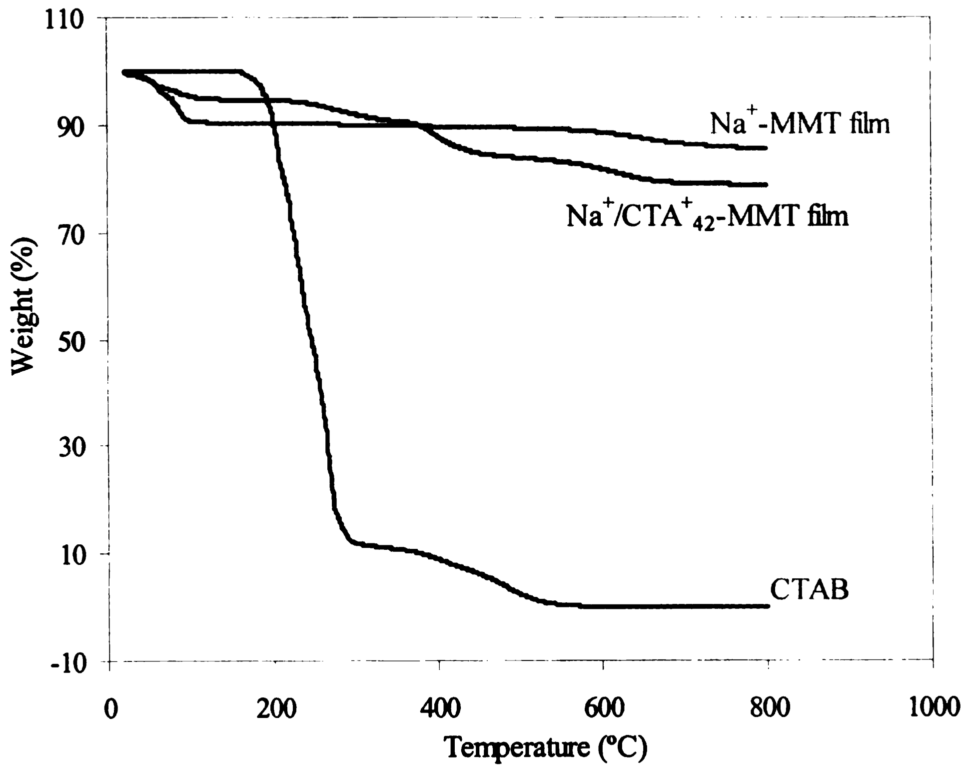

Figure 2.3 Thermogravimetric analysis (TGA) curves for cetyltrimethylammonium bromide powder, sodium montmorillonite and CTA^+ partially exchanged MMT clay fabric films.

2.3.2 Interfacial Adhesion and Oxygen Permeability of HDPE-Clay Fabric

Film Composites

Homoionic inorganic Na^+-MMT and Li^+-FH clay films exhibit no interfacial adhesion to the thermoplastic polyethylene since the polar Na^+ cations situated on the silicate basal planes inhibit the physical adsorption of non-polar –$(CH_2CH_2)_n$- chains to the outer surface of the clay film. Improvement in the interfacial adhesion is achieved by the fully or partially exchanged organo-MMT films with alkylammonium ions.

In fact, the clay films have two different external surfaces that result from the fabrication process. One side of the clay film is in contact with the glass substrate and the other surface contacts the air interface. The "glass" side of the clay film is smoother than the "air" side, suggesting that the evaporation of water during the drying procedure causes some disorientation of the individual clay nanolayers in the upper part of the clay film (air side) and the flat glass substrate may help the efficient alignment of nanoclay platelets in the lower part of the clay film as well (Figure 2.4 (a)). Concerning disorientation, platelike particles can aggregate in a disoriented edge-to-face manner and not only in a face-to-face manner.

It's interesting that two sides of the montmorillonite clay films exhibit different degrees of interfacial interaction with the HDPE polymer coatings. Peeling test shows the smooth "glass" sides of MMT clay films always adhere better to HDPE sheets than the rough "air" sides. The XRD of the HDPE sheet removed from the "air" interface of the Na^+/choline$_{25}$-MMT film exhibits the characteristic 001 peak of organo-MMT (Figure 2.4 (b)), which indicates the weak

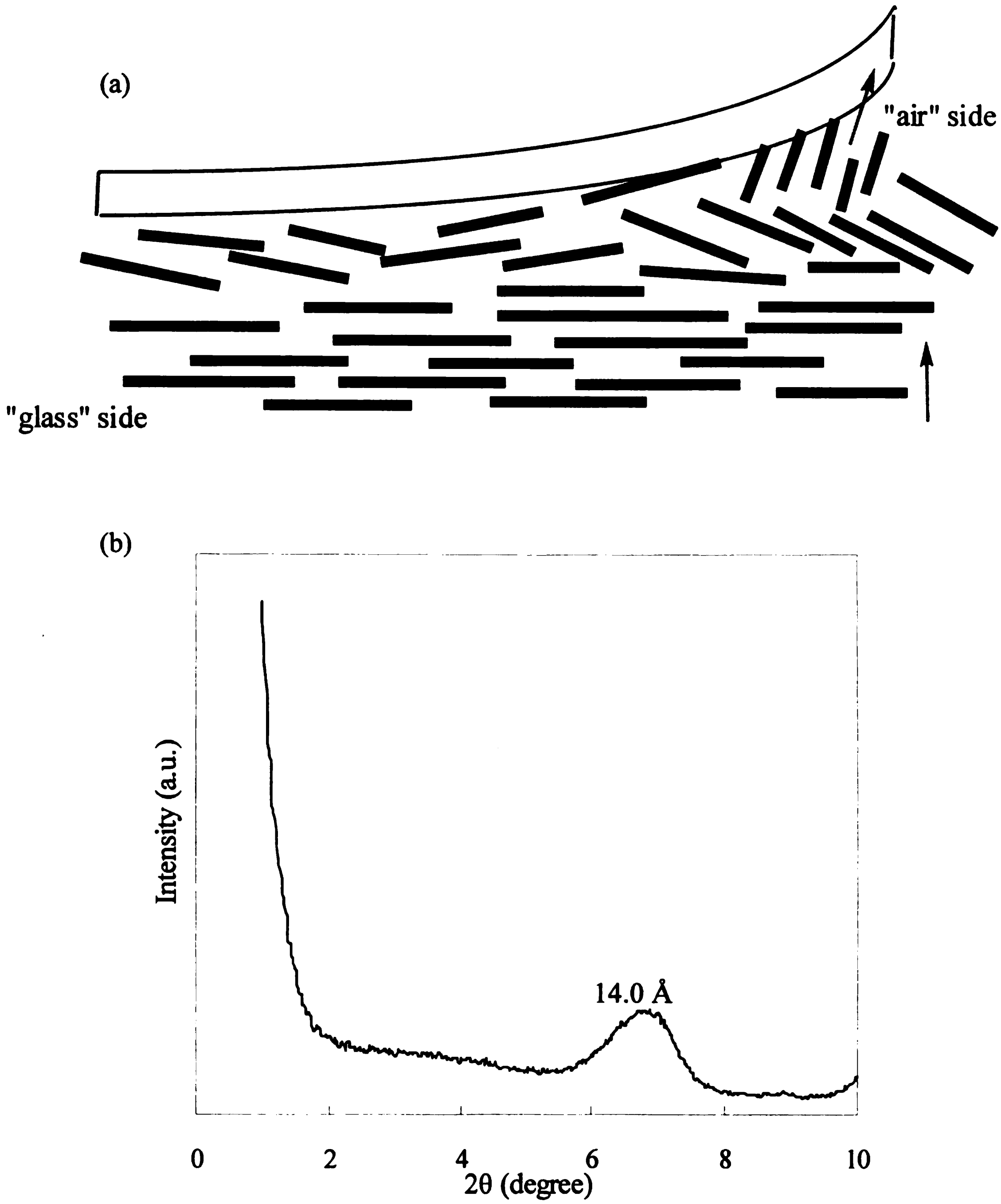

Figure 2.4 (a) Schematic representation of orientation of the clay nanolayers at the "air" and "glass" side of the clay fabric film and peeling off the HDPE coating from the "air" side; (b) XRD of HDPE sheet removed from the "air" side of the Na^+/$choline_{25}$-MMT film.

interface is at clay-clay interface instead of clay-polymer interface. It is well known that the individual MMT platy particles are held together by the electrostatic interaction. Therefore, pulling apart clay layers should not be easy. However, at the "air" side, the disorientation of the individual clay nanolayers decreases the magnitude of ionic bonding between the layers since some clay layers only interact in part with edges of adjacent clay platelets as shown in Figure 2.4 (a). On the other hand, the clay platelets at the "glass" side of the clay paper are well oriented face-to-face, which optimizes the electrostatic attraction between the stacked platelets. Another factor resulting in the weak clay-clay interface is when the HDPE coating was peeled off the "air" side of the clay film, the clay layers would move more relatively in the horizontal direction and in this direction it is much easier to overcome the ionic bonding to take them apart than in a vertical direction.

In comparison to organo-MMT composites, the interface failure at clay-clay interface was more obvious for the HDPE/organo-FH fabric film composites, wherein clay was clearly seen to be sticking to both sides of the HDPE sheet coating when peeled apart. It might be caused by the bent edge of fluorohectorite nanolayer taking less percent of space in the whole plate due to its higher aspect ratio.

From the SEM images, the clay films possess micro or sub-micro voids formed between particle edges and bent platelets. These voids generate extremely high O_2 permeability (>6000 cc·mil/m^2·day). However, betaine modified clay films are extremely impermeable towards oxygen gas (< 0.1 cc·mil/m^2·day), which may be explained by its unique nanostructure, wherein betaine molecules bind to the positively charged edges of clay layers and occupy the voids formed between particle edges.

Table 2.2 Oxygen permeability data for HDPE-clay fabric film composites

clay fabric film composition	thickness of clay fabric film (mm)	thickness of HDPE-clay fabric film composite (mm)	oxygen permeability (cc·mil/(m^2·day))
pristine HDPE		0.060	1832.3
Na$^+$/BET$_{100}$-MMT	0.049		≤0.1
choline$_{100}$-MMT	0.040	0.150	80.0
Na$^+$/choline$_{25}$-MMT[a]	0.025	0.084	76.3
Na$^+$/CTA$^+_{42}$-MMT	0.035	0.160	54.4
Na$^+$/CTA$^+_{42}$-MMT[a]	0.035	0.097	130.0
Li$^+$-FH	0.048	0.160	29.2
choline$_{100}$-FH	0.048	0.160	207.5
Li$^+$/CTA$^+_{40}$-FH	0.030	0.141	883.6

[a] The HDPE coating on the "air" side of the clay film has been peeled off, therefore, only one layer of HDPE coating exists on the "glass" side of the clay film.

Hot-pressing the clay films between a pair of thermoplastic HDPE sheets results in little or no intercalation of polyethylene into the clay gallery because the basal spacing doesn't change upon sandwiching clay film. Instead, the high density polyethylene coating blocks the surface voids on the outer region of the clay film, which dramatically improves the barrier property of the films. The O_2 permeability values of some composite samples were summarized in Table 2.2. For the HDPE composites prepared from organo-MMT clay films, the O_2 permeability is decreased 100- and 30-fold compared to the parent clay film and the pristine HDPE sheet (1832 cc·mil/m^2·day), respectively. Even after the removal of the HDPE coating from the weak "air" interface of organo-MMT film, the resulting composite retains the barrier property similar to the original composite. However, the organo-FH/HDPE composite films are more permeable than the corresponding montmorillonite composites with regard to oxygen. This may be attributable to the much larger aspect ratio of fluorohectorite platelets. The more bendable FH nanolayers may form folded sheets, resulting in more voids in the FH clay film and higher oxygen transmission rate. Interestingly, Li^+-FH/HDPE composites shows better barrier property toward oxygen (29.2 $cc \cdot mil/m^2 \cdot day$) than MMT composites.

2.3.3 Permeability of HDPE-Clay Fabric Film Composites toward Representative Petroleum Fuel Components

An effort was made to test the clay fabric films for automotive applications, particularly for potential applications in automotive fuel tanks. Measurements carried out in collaboration with Central Laboratory of Ford Motor Company have shown that high density polyethylene composite made from 150 mol % betaine modified Na^+-MMT clay fabric film is more than 200 times lower in permeability toward representative petroleum fuel components, toluene and isooctane and more than 50 times lower toward ethanol in comparison to the pristine polymer, which is consistent with the extremely high oxygen barrier performance of betaine montmorillonite films. However, this nanocomposite film is not applicable due to the lack of a chemically stable interface between the clay film and the HDPE matrix. The weak interface facilitates the condensation of the fuel components at the clay-polymer interface, causing the failure of the interface and the formation of blisters that fill with liquid fuel. Results from Ford Motor Company show that BET$_{150}$-MMT/HDPE composite maintained low level of permeation towards organic solvents in spite of the formation of blisters. However, the blisters compromise the structural integrity and strength of the composite.

In order to avoid blister formation, organic alkylammonium ions were used to modify the inorganic clay. The resulting HDPE-organoclay film composite was expected to provide adequate interfacial adhesion. The permeation rate curves of composite materials over the aging time from 1 day to 35 days are shown in Figure 2.5. Choline and CTA$^+$ exchanged MMT and FH clay film composites are not as impermeable as betaine MMT composite to petroleum components. However, no blisters are formed in these four samples, proving the adequate interfacial interaction at the clay-polymer interface. Although organo-FH/HDPE composites exhibit higher oxygen permeability than MMT composites as discussed before, they show less permeation than montmorillonite counterparts toward petroleum components. Particularly, homoionic choline fluorohectorite composite is the most impermeable to all three fuel components and the transmission rate is reduced to about one-sixth in comparison to the pure HDPE polymer.

Interestingly, toluene and ethanol permeation curves even show declining permeation rates in the case of CTA$^+$ exchanged montmorillonite and fluorohectorite composites, which is rather unusual. Typical permeation curves are evaluated based on the initial slope and the rate at equilibrium (flat). Most of

Figure 2.5 Permeation curves of HDPE-organoclay composite films and pure HDPE polymer towards toluene, isooctane and ethanol vapor at 40ºC.

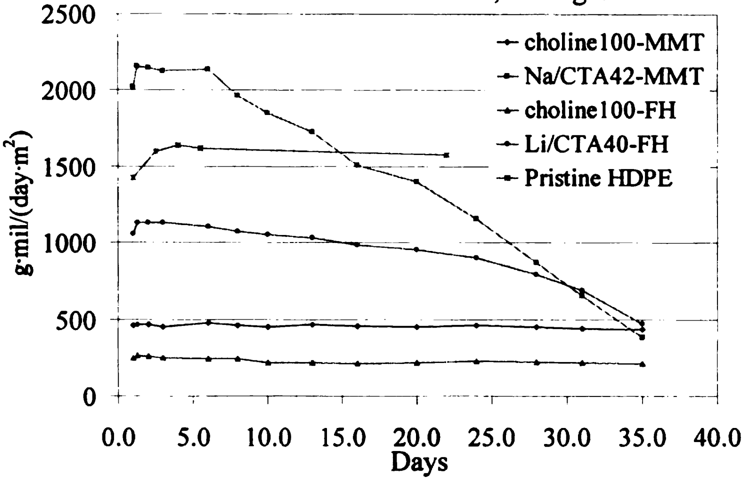
a. TOLUENE Permeation, 40 deg C.

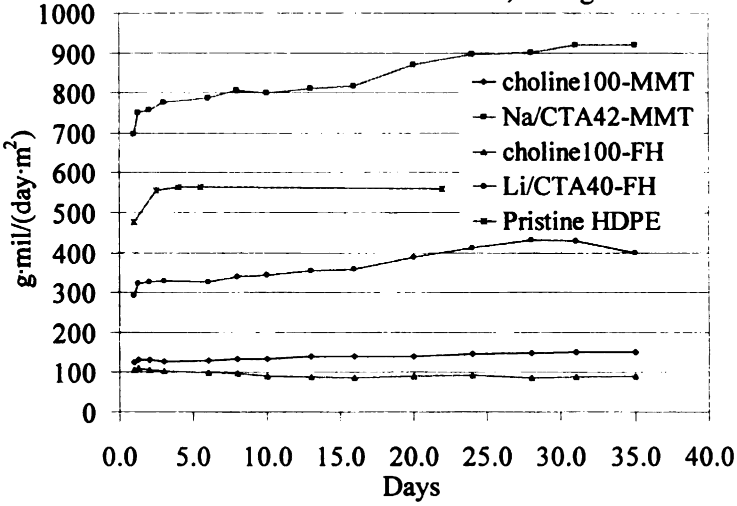
b. ISOOCTANE Permeation, 40 deg C.

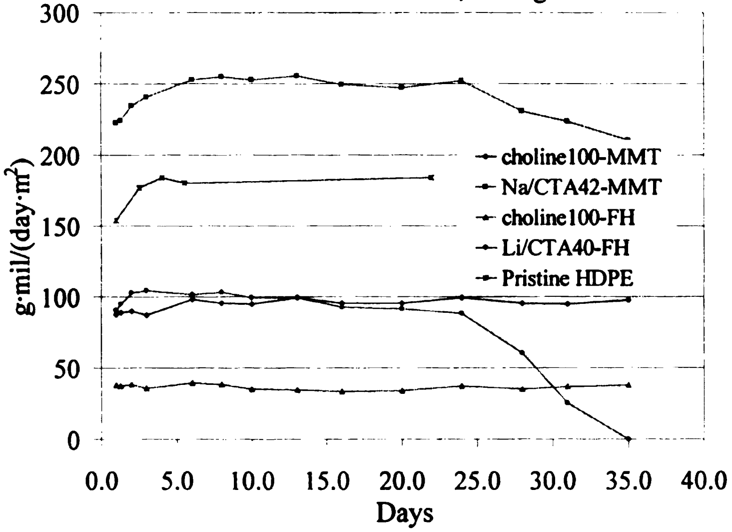
c. ETHANOL Permeation, 40 deg C.

the curves are flat, which would suggest an equilibrium condition. The unusual decrease in permeability with time might be due to the redistribution of long-chain alkyl ammonium ions CTA^+ during the penetration of organic molecules through the composite film, which may block the free volume between the bent clay layers and particle edges. The X-ray diffraction pattern of Na^+/CTA^+_{42}-MMT film after the toluene permeation test clearly exhibits a decrease in the intensity of 001 reflection peak characteristic of organo-clay intercalated by paraffin-like structured CTA^+ (see Figure 2.6), suggesting a swelling of the onium ion galleries and a change in the orientation state of this long alkyl chain onium ion in the gallery. The swelling of the galleries may contribute to a reduction in void volume between platelets.

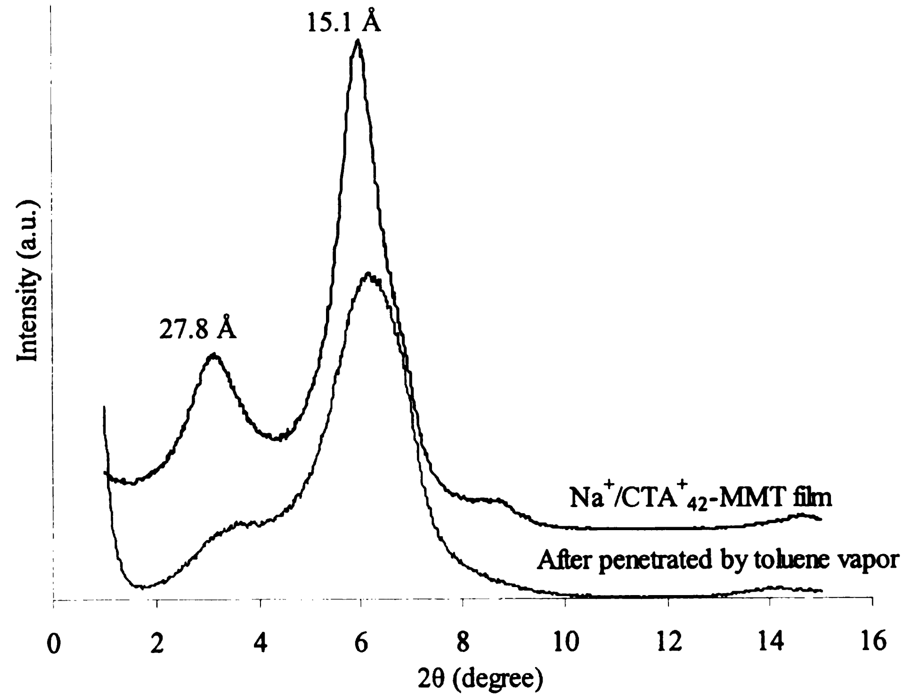

Figure 2.6 XRD patterns of Na^+/CTA^+_{42}-MMT clay fabric film before and after a toluene permeation test.

2.4 Summary

Self-supported clay fabric film nanotechnology was applied to the thermoplastic polyolefin system by sandwiching the clay film between two sheets of high density polyethylene (HDPE) in order to achieve high barrier property towards small molecules such as oxygen, as well as organic solvents included in the petroleum fuel (e.g., isooctane, toluene, ethanol). In order to match the compatibility of the polyolefin with layered silicate, homoionic organic and homostructured and heterostructured mixed inorganic-organic ion clay films were prepared by full or partial ion-exchange reaction of smectite clay Na^+-montmorillonite (MMT) and Li^+-fluorohectorite (FH) with long or short chain quaternary ammonium ions: cetyltrimethylammonium (CTA^+) $(CH_3)_3N^+(CH_2)_{15}CH_3$, and choline $(CH_3)_3N^+CH_2CH_2OH$, and zwitterionic compound betaine $(CH_3)_3N^+CH_2COO^-$. The pristine clay films are very permeable to oxygen due to the micro- to sub-micro size voids formed between clay nanolayer edges. However, the hot-pressed HDPE-clay composite films exhibit more than 100 and 30 times of decrease in O_2 permeability with respect to the parent clay films and the pristine polymer, respectively. The enhancement in barrier properties is attributable to blocking the voids between clay platelet edges on the external surface of clay film by polyethylene chains. Betaine modified montmorillonite film itself is extremely impermeable to oxygen owing to its unique nanostructure, wherein betaine molecules clung to the positively charged edges of clay layers and occupy the voids formed between particle edges. Moreover, high density polyethylene composite made from 150 mol % betaine modified

Na^+-MMT clay fabric film is more than 200 times lower in permeability toward representative petroleum fuel components, toluene and isooctane and more than 50 times lower toward ethanol, in comparison to the pristine polymer. However, this nanocomposite film is not applicable due to the lack of a chemically stable interface between the layered silicate and the polymer. On the other hand, organic alkylammonium ion modified clay films afford adequate interfacial adhesion. In the case of homoionic choline fluorohectorite composite, the transmission rate of all three organic solvents is reduced to about one-sixth in comparison to the pure polymer.

References

(1) Pinnavaia, T. J., Beall, G. W., Eds. *Polymer-Clay Nanocomposites*; John Wiley & Sons: New York, 2000.

(2) Jacquelot, E.; Espuche, E.; Gerard, J.-F.; Duchet, J.; Mazabraud, P. *J. Polym. Sci., Part B: Polym. Phys.* **2006**, *44*, 431.

(3) Zhong, Y.; Janes, D.; Zheng, Y.; Hetzer, M.; Kee, D. D. *Polym. Eng. Sci.* **2007**, *47*, 1101.

(4) Arunvisut, S.; Phummanee, S.; Somwangthanaroj, A. *J. Appl. Polym. Sci.* **2007**, *106*, 2210.

(5) Picard, E.; Gauthier, H.; Gerard, J.-F.; Espuche, E. *J. Colloid Interface Sci.* **2007**, *307*, 364.

(6) Deshmane, C.; Yuan, Q.; Misra, P. D. K. *Mater. Sci. Eng. A* **2007**, *460-461*, 277.

(7) Wang, Z. M.; Nakajima, H.; Manias, E.; Chung, T. C. *Macromolecules* **2003**, *36*, 8919.

(8) Galgali, G.; Ramesh, C.; Lele, A. *Macromolecules* **2001**, *34*, 852.

(9) Nam, P. H.; Maiti, P.; Okamoto, M.; Kotaka, T.; Hasegawa, N. Usuki, A. *Polymer* **2001**, *42*, 9633.

(10) Hotta, S.; Paul, D. R. *Polymer*, **2004**, *45*, 7639.

(11) Lu, B.; Chung, T. C. *Macromolecules* **1999**, *32*, 2525.

(12) Priola, A.; Bongiovanni, R.; Gozzelino, G. *Eur. Polym. J.* **1994**, *30*, 1047.

(13) Chung, T. C. *Prog. Polym. Sci.* **2002**, *27*, 39.

(14) Nielson, L. E. *J. Macromol. Sci. (Chem.)* **1967**, *A1*, 929.

(15) Suter, U. W.; Osman, M. A.; Mittal, V.; Morbidelli, M. *Macromolecules*, **2004**, *37*, 7250.

(16) Chaiko, D. J.; Leyva, A. A. *Chem. Mater.* **2005**, *17*, 13.

(17) Triantafyllidis, K. S.; LeBaron, P. C.; Park, I.; Pinnavaia, T. J. *Chem. Mater.* **2006**, *18*, 4393.

(18) Shao, H.; Pinnavaia, T. J. *Unpublished data*, **2006**.

CHAPTER 3

Gas Barrier Properties of Transparent Epoxy-Clay Fabric Film Composites

3.1 Introduction

The use of inorganic nanoparticles as additives to enhance polymer performances has been established. The technical advances provide numerous commercial opportunities in areas ranging from advanced aerospace systems to commodity plastics.[1] Small amounts (1-5 wt%) of highly anisotropic nanoparticles, such as layered silicates, carbon nanotubes or mesoporous silicas, provide polymer property enhancements that are comparable to those achieved by conventional loadings (15-40 wt%) of traditional fillers. Layered silicate clays, in particular smectite clays, have been widely used to improve the mechanical, thermal and barrier properties of thermoset and thermoplastic polymers. Owing to their high aspect ratio, ion-exchange capacity, good crystallinity and chemical robustness, smectite clays provide improvements that include high modulus[2], increased tensile strength[2-4] and heat distortion temperature[5], and decreased gas permeability[3-11] and thermal expansion coefficient.[3,4]

Polymers are used extensively in packaging applications, especially in food and drug packaging, where transparency and gas barrier properties are important criteria. Clay platelet particles (e.g., montmorillonite, fluorohectorite) enhance the barrier property of polymers according to a tortuous path model developed by Nielsen.[12] In this model, the impermeable clay nanolayers retard the transport of diffusing species such as oxygen or water vapor. The magnitude of improvement in barrier properties strongly depends on the aspect ratio, volume fraction, and the state of dispersion and orientation of the clay platelets. Epoxy-clay nanocomposites have been extensively studied with regard to the mechanism of clay tactoid intercalation and exfoliation, and the enhanced mechanical properties.[13-22] However, few researches have been reported regarding the gas barrier properties of epoxy nanocomposites.[23-26]

The oxygen transmission rate of the epoxy matrix was reduced to 1.25- to 4-fold at 1-5 vol% organoclay loading.[23] Long alkylammonium ions on the exchange sites of the clay enhance polymer intercalation, but contribute to an increase in the oxygen permeability coefficient probably due to the phase separation at the interface between the polymer and the layered silicates, which leads to a decrease in polymer density at the interface, resulting in higher "free volume" and consequently a higher transmission rate. In contrast to expectation, the composites made from organo-montmorillonite with ethoxylated alkylammonium ions exhibit the best oxygen barrier properties. The functional –OH group of the N-CH_2CH_2OH moiety in the short alkyl chain onium ions may react with the epoxy resin, energetically favoring the partial exfoliation of clay particles with the entropically unfavorable small d-spacings in epoxy matrix. This is verified by the existence of single nanolayers shown in the TEM cross-section images. However, only intercalated tactoids are observed for nanocomposites made from montmorillonite with non-functional long alkyl groups on the onium exchange cations, leading to even ~2 times higher oxygen transmission rate than that of the neat polymer. Therefore, exfoliated aluminosilicate layers build a better barrier toward the diffusing gas molecules, whereas the polymer interlayered tactoids do not contribute much to the permeation barrier performance. However, the best barrier property enhancement is only a 4-fold reduction in the oxygen permeability in comparison to the neat epoxy polymer owing to the limited exfoliation and dis-alignments of the individual clay layers. A recent study[26] of the oxygen barrier properties of epoxy-clay fabric film composites proposed a new strategy based on impregnating the self-supported clay papers with epoxy polymer. These clay fabric films provide 2-3 orders of magnitude reduction in O_2 permeability. However, the adhesion of the epoxy matrix to the clay film was poor, thus limiting the usefulness of the films.

In our study, in order to improve the interfacial adhesion of clay films to the thermoset epoxy matrix, various homoionic organic and homostructured and heterostructured mixed inorganic-organic ion clay films were prepared by full or partial ion-exchange reactions of smectite clay Na^+-montmorillonite (MMT) and Li^+-fluorohectorite (FH) with organic onium ions: cetyltrimethylammonium (CTA^+) $(CH_3)_3N^+(CH_2)_{15}CH_3$, choline $(CH_3)_3N^+CH_2CH_2OH$, glycidyltrimethylammonium (GTA^+) 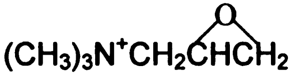 $(CH_3)_3N^+CH_2\overset{O}{CHCH_2}$ and diprotonated primary α, ω-diamine $H_2NCH(CH_3)CH_2[OCH_2CH(CH_3)]_xNH_2$ (denoted Jeffamine D2000 with $x = 33.1$). The objective of the present work is to prepare homoionic organic and mixed inorganic-organic ion smectite clay fabric films and to examine the interfacial adhesion between the epoxy coating and the clay films. In addition to the very high oxygen barrier properties, some epoxy-clay fabric film composites also provide attractive optical properties.

3.2 Experimental

3.2.1 Materials

The epoxide resin used for the formation of the glassy epoxy – clay composite films was a diglycidyl ether of bisphenol A (DGEBA), more specifically, Shell EPON 826 with an epoxy equivalent weight of ~182 g/equivalent:

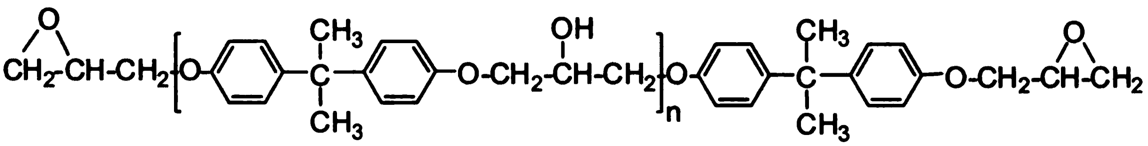

$n = 0$ (90 %), 1 (10 %) (Scheme 3-1)

The curing agent was a polyoxypropylene diamine of the type $NH_2CH(CH_3)CH_2[OCH_2CH(CH_3)]_xNH_2$ (x=2.6), which was provided by Huntsman Chemicals under the tradename Jeffamine D230. Jeffamine D2000 (x=33.1) was used for the preparation of heterostructured mixed organic-inorganic ion clay films. PGW Na^+-montmorillonite (Na^+-MMT) with a cation exchange capacity (CEC) of 100 meq/ 100 g was provided by Nanocor Inc.. A synthetic Li^+-fluorohectorite clay (Li^+-FH) with a CEC similar to that of PGW montmorillonite was obtained from Corning Inc.. All other chemicals were purchased from Aldrich Chemical Co. and used without further purification.

3.2.2 Preparation of Homoionic and Mixed-ion Clay Fabric Films

Homoionic inorganic Na^+-montmorillonite and Li^+-fluorohectorite clay films were made by preparing a 5 wt% homogeneous aqueous colloidal suspension of clay powders, then casting the suspension on a flat glass substrate, followed by drying in air for 1 day at room temperature. Continuous and self-supported clay fabric films were carefully peeled off the glass plate.

The homoionic organic clay films and the mixed inorganic-organic clay films were prepared by ion exchange of an aqueous inorganic clay suspension with the desired amount of onium ions. Usually, the ion-exchange reactions were carried out for 24-48 h and the exchanged clay were isolated by centrifugation and washed with deionized water for 3 to 4 times until free of Na^+. The washed clay was used to form a self-supported film as described above.

3.2.3 Preparation of Epoxy-Clay Fabric Film Composites

Pristine glassy epoxy polymer specimens (disks) were prepared by mixing stoichiometric amounts of epoxy monomer (EPON 826) and curing agent (Jeffamine D230) at 50°C for ~30 min. Liquid mixture was then outgassed at room temperature for 20 min and cured on an aluminum disk mold at 75°C for 3 h and then at 125°C for another 3 h under N_2 flow. The formed epoxy disks were polished to an average thickness of ~0.2 mm (~8 mil).

For the preparation of the epoxy-clay composite film sepecimens, the self-supported clay fabric films were dip-coated with a stoichiometric mixture of outgassed EPON 826 and Jeffamine D230. The wetted films were then suspended vertically to remove excess uncured resin. After being allowed to age in air for 1 day, the partially cured composite was heated in an oven at 125°C for 3 h in nitrogen to complete the cure.

3.2.4 Characterization and Testing of Clay Films and Epoxy – Clay Film Composites

X-ray diffraction (XRD) patterns were obtained on a Rigaku rotaflex 200B diffractometer equipped with Cu Kα X-ray radiation and a curved crystal graphite monochromator, operating at 45 KV and 100 mA. Samples of the clay films or the epoxy – clay composite films were prepared by mounting the films on glass X-ray sample holders.

Thermogravimetric analyses (TGA) of the clay films were performed using a Cahn TG System 121 Analyzer. The clay films were ground to produce powdered clays, which were heated to 800°C at a rate of 5°C/min under N_2 flow.

Scanning electron microscope energy dispersive spectroscopy (SEM-EDS) was performed on a JEOL 6400V microscope with LaB_6 emitter, and the EDS detector was an INCA x-sight. The film samples were mounted on aluminum stubs and coated with carbon before the analysis. The compositions of the clay films were determined by SEM-EDS, CHN chemical analysis and TGA analysis.

Transmission electron microscopy (TEM) images were obtained on a JEOL 2200FS field emission microscope with a ZrO/W Schottky electron gun and an accelerating voltage of 200 kV. Thin sections (~100 nm thick) of the epoxy-clay composite films were put on naked copper grids.

Oxygen permeability measurements were performed on a Mocon Ox-tran 2/60 oxygen permeability instrument with 100% oxygen as test gas. The specimens tested were the pristine epoxy polymer disks with an average thickness of ~0.2 mm (~8 mil), and the epoxy – clay fabric film composites with an average thickness of ~0.05 to ~0.10 mm.

3.3 Results and Discussion

3.3.1 Composition and Structural Properties of Homoionic and Mixed-ion Montmorillonite Clay Fabric Films and Their Epoxy Composites

The preparation of homoionic inorganic Na^+-montmorillonite and Li^+-fluorohectorite clay fabric films was described in Chapter 2, along with their X-ray patterns (Figure 2.1). Na^+-montmorillonite and Li^+-fluorohectorite clay fabric films are self-supported, smooth, and semi-transparent. Moreover, Li^+-fluorohectorite fabric film is very robust paper-like material and much more flexible than Na^+-montmorillonite film. The difference in flexibility is in accord with the difference in platelet aspect ratio which is ~2,000 for fluorohectorite vs. ~200 for montmorillonite. The difference in film flexibility is maintained for the mixed inorganic-organic cation exchange forms of the two clays.

Epoxy-clay fabric film composites were prepared by impregnating the clay film with a stoichiometric mixture of the epoxy resin Epon 826 and curing agent Jeffamine D230. The impregnated films were partially cured at room temperature, followed by full curing at 125°C for 3 hours. For the homoionic inorganic Na^+-montmorillonite and Li^+-fluorohectorite clay films, both showed very poor interfacial adhesion to the thermoset epoxy matrix. This can be explained by the fact that large amounts of polar inorganic ions situated on the basal surfaces of layered silicates impede the physical adsorption and intercalation of epoxy polymer chain to the clay, thus resulting in very weak interfacial interaction between these clay films and polymer.

Table 3.1 Basal spacings of homoionic and mixed-ion montmorillonite and fluorohectorite clay fabric films

clay sample designation	organic modifier	onium ion (%) [a]	basal spacings d_{001} (Å)	description
Na$^+$-MMT (PGW)	-	-	12.3	continuous film
choline$_{100}$-MMT	choline	100	14.1	continuous film
Na$^+$/CTA$^+_{42}$-MMT	CTA	42	27.8, 15.1	continuous film
Na$^+$/GTA$^+_{60}$-MMT	GTA	60	14.1	continuous film
Na$^+$/GTA$^+_{80}$-MMT	GTA	80	14.1	continuous film
Na$^+$/GTA$^+_{100}$-MMT	GTA	100	14.0	powdered, no film
Na$^+$/D2000$^+_{20}$-MMT	D2000	20	30.0, 15.9	continuous film
Na$^+$/D2000$^+_{40}$-MMT	D2000	40	42.9, 16.3	continuous film
Na$^+$/D2000$^+_{60}$-MMT	D2000	60	41.3, 16.4	continuous film
Na$^+$/D2000$^+_{80}$-MMT	D2000	80	-	easily fractured film
D2000$^+_{100}$-MMT	D2000	100	42.4	powdered, no film
Li$^+$-FH	-	-	12.1	continuous film
choline$_{100}$-FH	choline	100	13.8	continuous film
Li$^+$/CTA$^+_{40}$-FH	CTA	40	27.1, 13.5, 12.1	continuous film
Li$^+$/D2000$^+_{6.7}$-FH	D2000	6.7	72.4, 12.2	continuous film
Li$^+$/D2000$^+_{15}$-FH	D2000	15	57.0, 12.2	continuous film
Li$^+$/D2000$^+_{20}$-FH	D2000	20	62.2, 12.2	continuous film
Choline$_{90}$/D2000$^+_{10}$-FH	choline, D2000	90, 10	71.0, 13.8	continuous film
Choline$_{80}$/D2000$^+_{20}$-FH	choline, D2000	80, 20	71.0, 13.8	continuous film

[a] The percent onium ion-exchange represents the extent to which the ion-exchange sites of the clay have been replaced by onium ions; the reported values were determined by elemental or TGA analysis.

Homoionic organic clay fabric films and homostructured and heterostructured mixed inorganic-organic ion clay fabric films using different onium ions were prepared to evaluate interfacial adhesion to a thermoset epoxy matrix. The basal spacings for the films are summarized in Table 3.1. The improvement in the interfacial adhesion is found for the composites made from homoionic organo montmorillonite film intercalated exclusively by choline ion $(CH_3)_3N^+CH_2CH_2OH$ (denoted choline$_{100}$-MMT). The adhesion may be attributed to the hydroxyl group in the choline cation. Due to the 3-membered ring strain in the epoxide group of epoxy monomer, even the neutral –OH group in choline is a good nucleophile to attack the epoxide ring, forming an ether linkage with the epoxy monomer. The OH-epoxy interaction can be the driving force for the pre-solvation of the clay by epoxy pre-polymer and curing agent. Thus, the interaction of the choline and epoxy monomer is not only confined to the outer region of the clay film but also exists in the internal region of the film. The covalent bond between the choline cations and the epoxy resin contributes to the improvement in adhesion.

The mixed ion clay film containing 42 mol% cetyltrimethylammonium (CTA^+) cations on the exchange sites of Na^+-montmorillonite also exhibited good adhesion to the epoxy polymer. The long-chain alkylammonium ion CTA^+ results in a large basal spacing at 27.8 Å in the parent clay film (as shown in Figure 3.1), which facilitates swelling the clay gallery by the uncured precursor. XRD patterns show that the parent clay film has two d-spacings. The peak at 27.8 Å can be attributed to the clay gallery interlayered by paraffin-like structured onium ions. However, for the gallery with a lower basal spacing of 15.1 Å, the onium ions adopt a monolayer orientation. Therefore, phase segregation of clay layers exist in the clay film due to the different orientation of alkyl surfactants in the clay interlayer. For the epoxy composites, the disappearance of the diffraction peak with the larger interlayer spacing indicates that these clay layers are highly exfoliated in the thermoset epoxy matrix upon curing. The reduction in the intensity of the diffraction peak with regard to the smaller basal spacing suggests some of these clay particles are swelled by the polymer. Even though only unfavorable physical van der Waals interaction exists between the epoxy polymer and cationic surfactants CTA$^+$, the dispersion of clay layers in the epoxy matrix maximize the number of contacts of the two phases, therefore, resulting in some degree of adhesion.

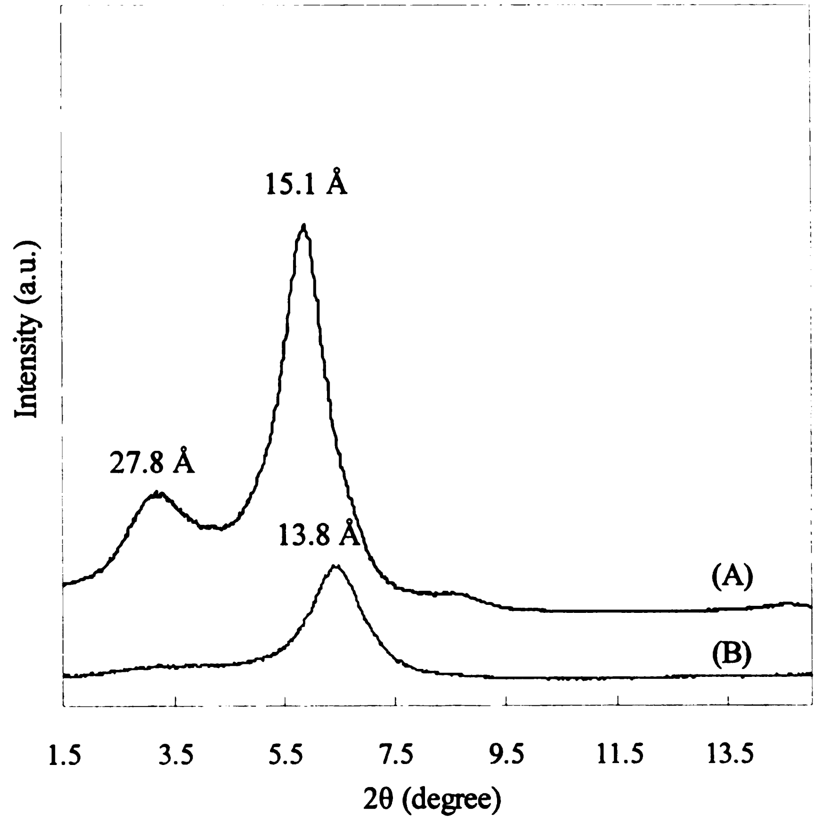

Figure 3.1 X-ray diffraction (XRD) patterns of (A) Na$^+$/CTA$^+_{42}$-MMT clay fabric film and (B) epoxy-clay film composite made from (A).

Self-supported clay films exhibit two distinguishable surfaces due to the method used to prepare the films. One surface contacts the glass substrate and the other surface contacts the air interface. The "glass" side of the clay film is smoother than its "air" side, suggesting that the evaporation of water causes some disorientation of the individual clay nanolayers in the upper part of the clay film (air side). Also, the flat glass substrate may help to align the clay platelets in the lower part of the clay film. It's interesting to note that two sides of the clay films exhibit different degree of interfacial interaction to the epoxy polymer in both epoxy-clay fabric film composites discussed above. Peeling test shows that the smooth "glass" side of the clay film adheres better to the epoxy than the rough "air" side. This interesting phenomenon will be further discussed later.

In order to further improve the adhesion between the clay film and epoxy coating, functional onium ion exchanged clay films were prepared, wherein the organic modifiers play a functional role in linking the clay film to the polymer matrix by forming covalent bonds at the interface of the two phases. Alkyl ammonium ions terminated with either epoxide group or amino group are good candidates as functional organic modifiers.

A series of glycidyltrimethylammonium (GTA^+) -PGW clays were prepared at three different levels of GTA^+ exchange, namely 60%, 80% and 100%. Continuous films were obtained at 60% and 80% exchange, but homoionic GTA^+-MMT clay at 100% exchange did not afford a continuous film. The basal spacing of 14.1 Å tells us that this short chain onium ion orients in a monolayer fashion in the gallery. The decrease in the intensity of the 001 diffraction peak of the epoxy/GTA$^{+}{}_{80}$-PGW composite film (as shown in Figure 3.2) suggests that some of the clay galleries were swollen by the epoxy polymer. The small gallery height in the parent homostructured mixed-ion clay film might impede the transport of curing agent and epoxy monomer into the clay galleries. However, the glycidyltrimethylammonium ions can form covalent bonds with curing agent D230 by ring-opening polymerization. This is expected to be the driving force for the solvation of clay layers by the polymer precursors.

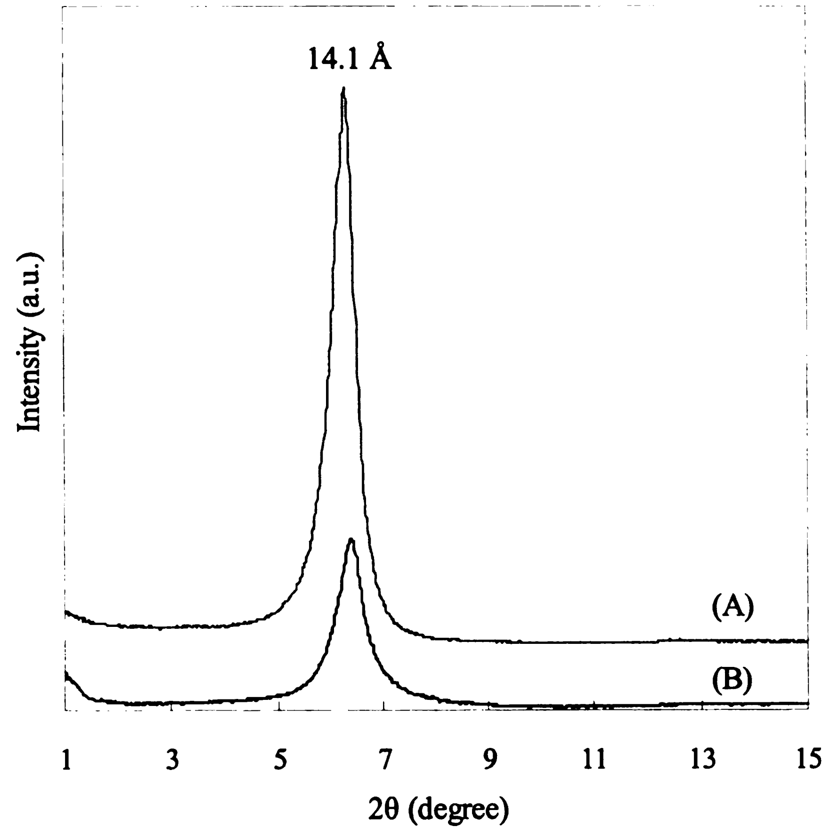

Figure 3.2 X-ray diffraction (XRD) patterns of (A) homostructured mixed-ion Na^{+}/GTA$^{+}{}_{80}$-MMT clay fabric film and (B) epoxy-clay film composite made from (A).

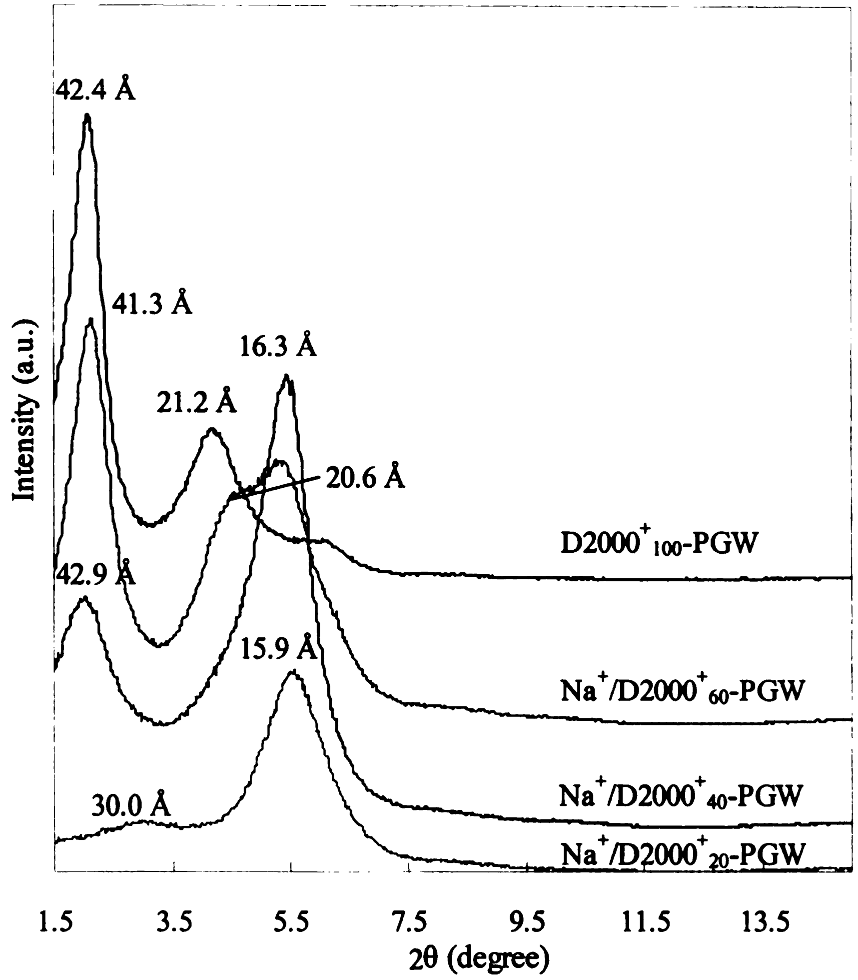

Figure 3.3 X-ray diffraction (XRD) patterns of diprotonated diamine Jeffamine D2000 exchanged montmorillonite fabric films at different onium ion equivalents.

Diprotonated diamine D2000 cation in mixed ion montmorillonite functions concomitantly as a clay surface modifier, an acid catalyst for the intragallery polymerization of epoxy monomers, and the curing agent in the thermoset epoxy matrix. Figure 3.3 provides the XRD patterns for a series of diprotonated Jeffamine D2000 onium ion exchanged PGW films. Replacement of up to 60% of the Na^+ ions by D2000 cations are still capable of forming continuous montmorillonite clay films (see Table 3.1). However, homoionic organoclay $D2000_{100}$-MMT forms a powder rather than a continuous film upon casting the clay suspension on glass. For the mixed-ion $D2000^+$-Na^+ montmorillonite films at 60%, 40% and 20% onium ion equivalent levels, two basal spacings are observed, indicating the existence of two phases in the clay film. The larger d-spacing of ~40 Å can be attributed to clay galleries intercalated by polyamine adopting a folded chain conformation as shown in Figure 3.4, part B. However, some diamines adopt a more extended chain orientation, which result in a lower d-spacing at ~16 Å. The $D2000_{60}$-PGW clay film shows a second order harmonic d_{002} at 20.6 Å. There is no evidence of a separate inorganic-rich phase (d-spacing 12.3 Å) in any of the mixed-ion clay films.

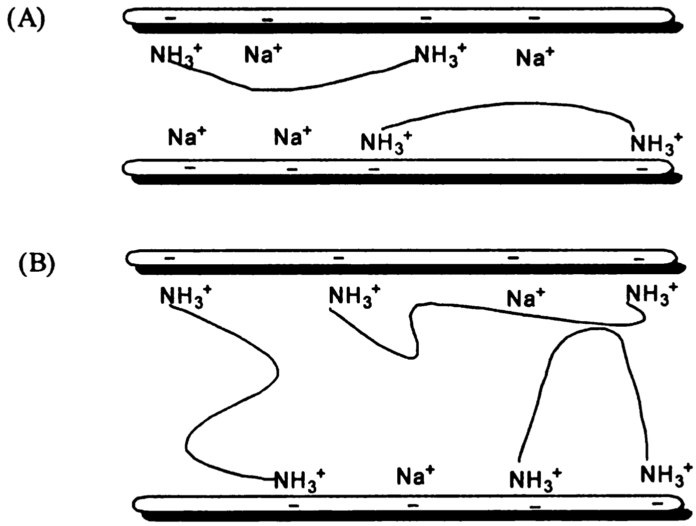

Figure 3.4 Schematic representation of the orientations of the diprotonated diamine Jeffamine D2000 onium ions intercalated in the mixed Na^+-onium ion smectite clay: (A) the diamine adopts an extended chain conformation in the gallery with low d-spacing of ~ 16 Å; (B) the diamine adopts a folded chain conformation in the gallery with high d-spacing of ~ 40 Å.

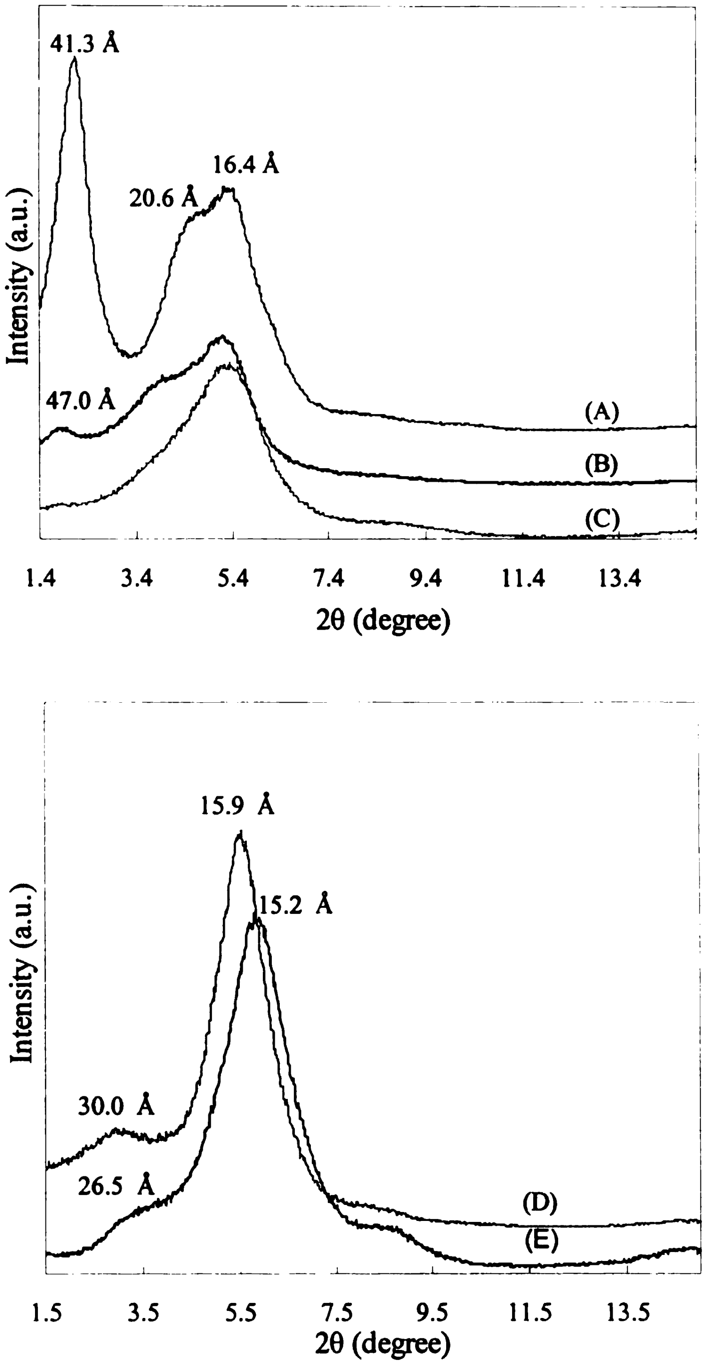

Figure 3.5 X-ray diffraction (XRD) patterns of (A) heterostructured $Na^+/D2000^+_{60}$-MMT clay fabric film, (B) epoxy-clay film composite made from (A), only aged under ambient conditions, (C) epoxy-clay film composite made from (A), further cured at 125°C for 3h, (D) heterostructured $Na^+/D2000^+_{20}$-MMT clay fabric film, (E) epoxy-clay film composite made from (D).

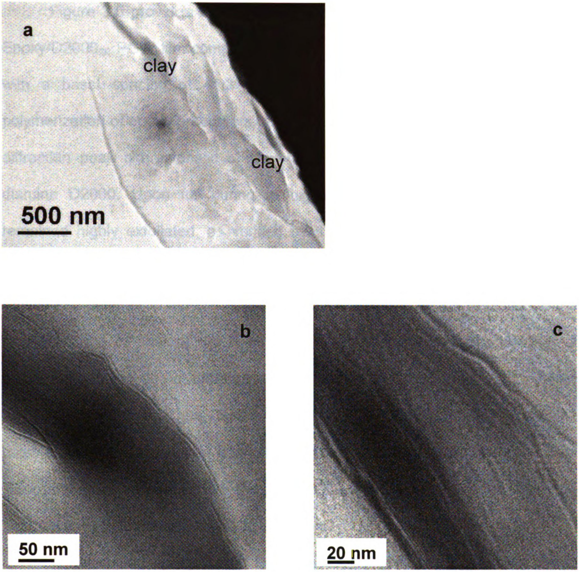

Figure 3.6 TEM images of thin section of an epoxy-D2000$_{20}$ PGW composite film showing the c-axis direction (cross-section): (a) low-magnification image showing spacial distribution of clay aggregates; (b) exfoliated clay nanolayers in composite film and (c) stacked clay layers in clay tactoids in composite film.

Figure 3.5 provides representative XRD patterns for Epoxy-D2000$_{60}$ and Epoxy-D2000$_{20}$ PGW film composites. After being cured in air, the clay particles with a basal spacing of 41.3 Å are highly separated by the intragallery polymerization of epoxy precursors, resulting in a decrease in the intensity of the diffraction peak characteristic of clay nanolayers intercalated by folded-chain diamine D2000. Upon full curing at higher temperature, these clay layers remained highly exfoliated, as verified by the disappearance of the diffraction peak in the small-angel region of the XRD pattern. Evidence for clay layer swelling by polymer in the D2000$_{20}$-PGW film is provided by the reduction in the intensity of the 2θ peak at ~30 Å. However, clay platelets with lower spacings of 16.4 Å and 15.9 Å do not undergo an expansion in basal spacing upon polymer composite formation. Thus, these clay particles are not interlayered by the polymer. Both exfoliated and intercalated clay structures can be observed from TEM images of thin-sectioned epoxy/ D2000$_{20}$-PGW composite film shown in Figure 3.6, in agreement with the XRD pattern.

The resulting epoxy-D2000 PGW composite films have attractive optical properties, as illustrated by the optical images shown in Figure 3.7, parts a and b. The composite film made from D2000$_{20}$-PGW is totally transparent and very smooth. The "glass" side of the film shows good adhesion to the epoxy matrix. The adhesion at the "air" side of the film is less robust. Epoxy composites from 40% and 60% D2000 onium ion exchanged PGW have unfavorable "wetting marks" on the surface, which decrease the clarity of the composites. Moreover, the 40% and 60% D2000 composites are very brittle, even more brittle than the parent clay paper, which is consistent with the high modulus of the epoxy matrix. The fragile nature of the composites formed from D2000$_{40}$ and D2000$_{60}$-PGW clay film is associated with the "wetting mark" imperfections but the interfacial adhesion exhibits the best result so far and the epoxy polymer coating cannot be peeled off either side of the clay film.

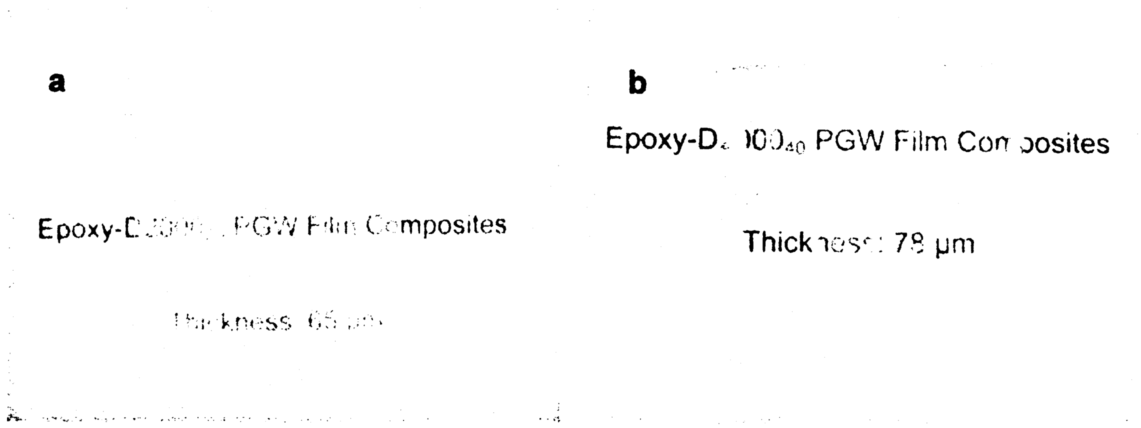

Figure 3.7 Optical images of (a) Epoxy-D2000$_{20}$ PGW film composites with a thickness of 65 μm and (b) Epoxy-D2000$_{40}$ PGW film composites with a thickness of 78 μm.

The parent mixed-ion D2000-Na$^+$ montmorillonite clay films are opaque, which can be attributed to the high degree of light scattering caused by the efficient alignment of clay platelets. However, the epoxy composite films are optically transparent. The improvement in transparency might originate from the reduction of the oriented stacking of clay nanolayers due to the exfoliation of clay layers by the polymer. Optical clarity of the nanocomposites depends on layered silicate orientation, as the amount of scattering and haziness is relative to size of the particle and wavelength of light. Alignment of the layers perpendicular to the surface will decrease the effective particle size, by a factor associated with the plate aspect ratio. However, a more likely reason for the improved transparency for the composite films is the matching of the refractive index for the clay and the epoxy polymer.

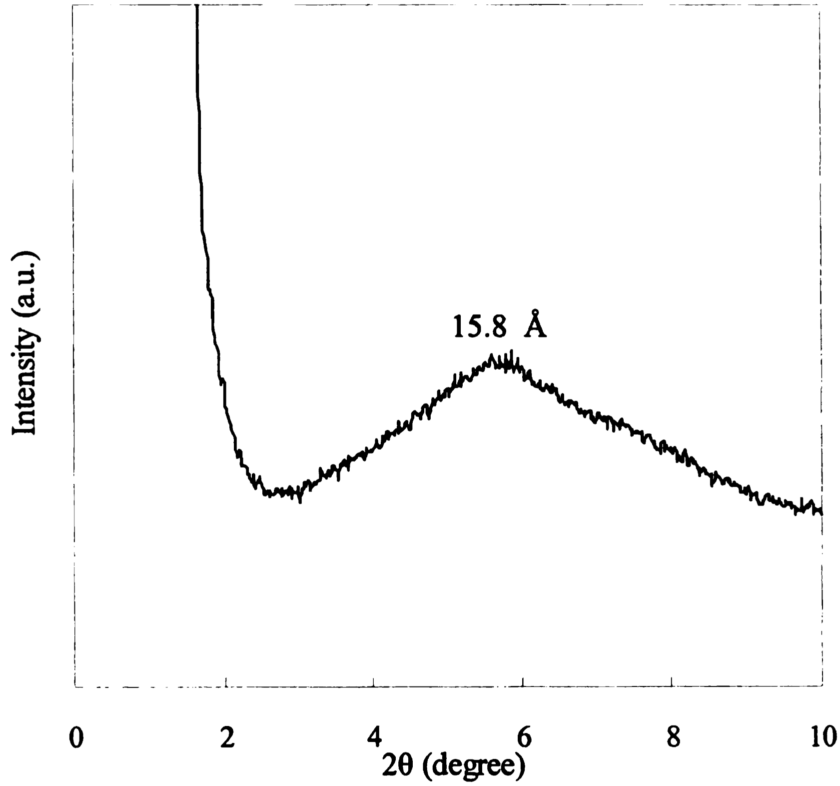

Figure 3.8 X-ray diffraction (XRD) pattern of epoxy coating released from the "air" side of $Na^+/D2000^+{}_{20}$-MMT clay fabric film.

Adhesion of the clay film to the epoxy polymer is facilitated by the formation of covalent bonds at the interface of the two phases. The large contact areas between the two phases due to clay layer swelling by the epoxy matrix also promote better adhesion. With good polymer-clay adhesion, the weakness at the interface may be caused by clay-clay interface, not by clay-epoxy interface. This hypothesis is verified by the X-ray diffraction pattern (Figure 3.8) and SEM-EDS analysis of the epoxy layer released from the "air" side of a $D2000_{20}$-PGW film. The reflection peak at 15.8 Å is characteristic of clay layers intercalated by diamines with a folded chain conformation, thus verifying that the clay particles undergo delamination when the film is peeled apart. A SEM-EDS analysis of the epoxy removed from the "air" side of $D2000_{20}$-PGW film showed the molar ratio of Na : Mg : Al : Si is 1.67 : 1.27 : 5.30 : 11.45, in agreement within experimental error with the unit cell composition of montmorillonite and further proving that the weakness at the interface is caused by the clay-clay interface.

The individual MMT nanolayers are held together by the electrostatic interaction. Therefore, pulling apart clay layers should not be easy. However, at the "air" side, the disorientation of the individual clay nanolayers decreases the magnitude of ionic bonding between the layers since some clay layers only interact in part with the edges of other clay platelets as illustrated in Figure 2.4 (a) of Chapter 2. On the other hand, the clay platelets at the "glass" side of the clay paper are well oriented face-to-face, which optimizes the electrostatic attraction between the stacked platelets. Another factor that weakens the clay-clay interface is when the epoxy coating was peeled off the "air" side of the clay film, the clay layers move relatively in a horizontal direction and in this direction it is much easier to overcome the ionic bonding to take them apart in comparison to taking them apart in a vertical direction.

3.3.2 Composition and Structural Properties of Homoionic and Mixed-ion Fluorohectorite Clay Fabric Films and Their Epoxy Composites.

Homoionic inorganic Li^+-fluorohectorite clay films are very robust paper-like materials with high flexibility that can be associated with the large aspect ratio of fluorohectorite. The aspect ratio of fluorohectorite is ten times higher than that of montmorillonite. Also, this large particle size results in the more efficient alignment of clay nanolayers in fluorohectorite paper, as verified by a much more intense 001 reflection peak compared with montmorillonite.

In order to obtain good interfacial interaction with an epoxy matrix, various homoionic organic and mixed inorganic-organic ion fluorohectorite clay films were prepared through ion-exchange reaction with desired onium ions (Table 3.1). Homoionic choline exchanged fluorohectorite film only has one d-spacing of 13.8 Å as shown in the XRD pattern of Figure 3.9. The segregation of the organic and inorganic exchange cations into separate galleries exist in the 40% CTA^+ exchanged Li^+-fluorohectorite film. Basal spacings of 27.1 Å and 13.5 Å suggest the onium ion galleries are interlayered by alkylammonium ions with paraffin-like and monolayer orientations, respectively. The diffraction peak at 12.1 Å can be attributed to the inorganic phase exclusively intercalated by Li^+ ions. The segregation of the ions is driven by differences in the solvation properties of these two very different types of cations. The inorganic galleries of the heterostructure are hydrophilic and readily solvated by water, whereas the organic galleries are lipophilic and avoid hydration.[27]

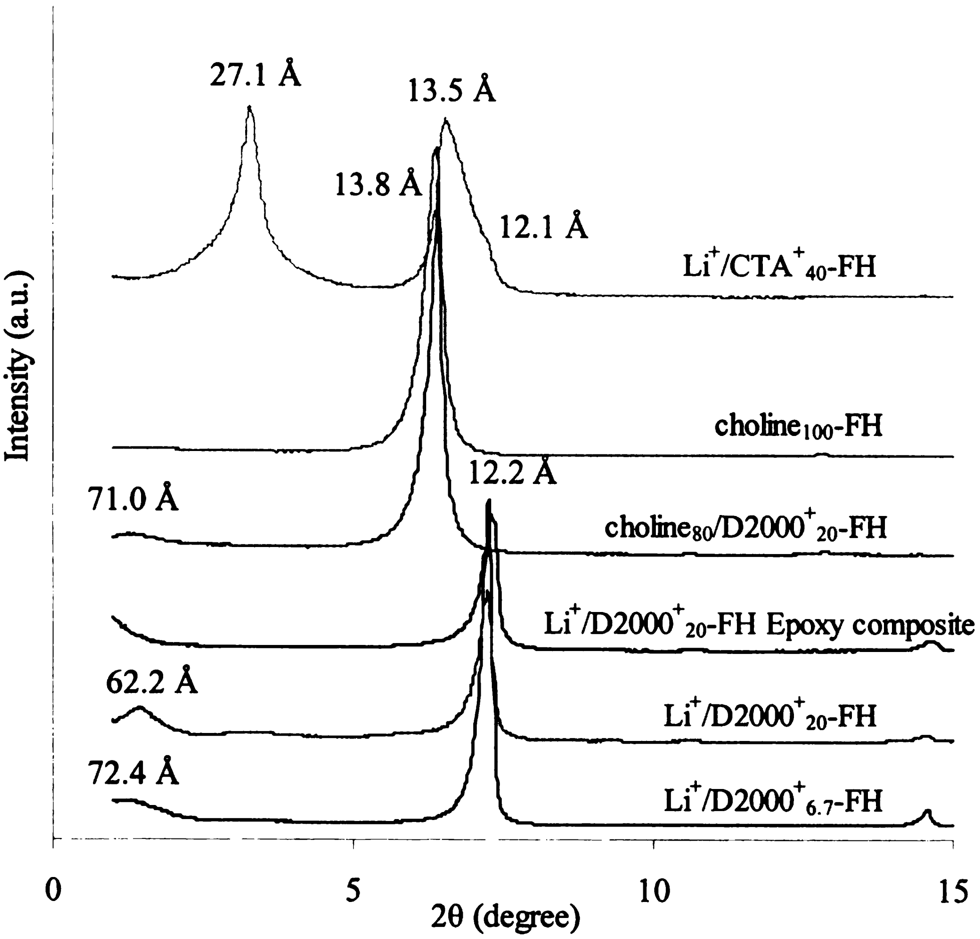

Figure 3.9 X-ray diffraction (XRD) patterns of homoionic organic and mixed inorganic-organic ion fluorohectorite films.

The partial replacement of Li^+ ions with diprotonated diamine D2000 also results in the segregation of two types of cations into separate galleries, affording a mixture of an organic and inorganic clay phases. XRD patterns of $Li^+/D2000^+_{6.7}$-FH and $Li^+/D2000^+_{20}$-FH (Figure 3.9) show that the diffraction peak of the inorganic phase at 12.2 Å is more intense than that of organic phase at 72.4 Å and 62.2 Å, resulting from the galleries interlayered by diprotonated D2000 with a folded chain conformation. The disappearance of the peak for the organic phase in $Li^+/D2000^+_{20}$-FH /epoxy composites after epoxy impregnation indicates that those clay layers are highly swollen by the epoxy matrix. However, the inorganic phase is not intercalated by polymer.

$Li^+/D2000^+_{6.7}$-FH fabric film can afford a highly transparent composite with epoxy polymer (Figure 3.10, part a). However, the "wetting marks" on the composite films made from $Li^+/D2000^+_{20}$-FH decrease the optical transparency (Figure 3.10, part b).

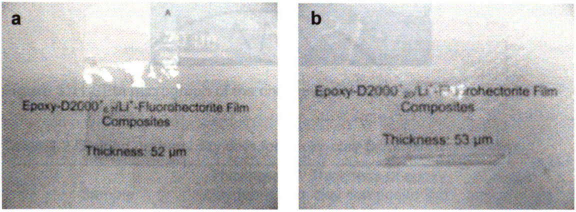

Figure 3.10 Optical images of (a) Epoxy-$D2000_{6.7}$ FH film composites with a thickness of 52 μm and (b) Epoxy-$D2000_{20}$ FH film composites with a thickness of 53 μm.

3.3.3 Oxygen Barrier Properties of Epoxy-Clay Fabric Film Composites.

The bulk density of Na^+-montmorillonite film (2.0 g/cm^3) is smaller than the intrinsic density of Na^+-MMT tactoids (2.6 g/cm^3),[24] indicating that approximately 23 vol % of the clay fabric film is occupied by the voids formed between bent clay layers or clay platelet edges. This imperfect tiling of the layers results in the high oxygen permeability of pristine Na$^+$-montmorillonite film (> 6000 cc·mil/m^2·day). SEM image of choline$_{100}$-FH film (Figure 3.11) shows the micro-size voids formed between platy fluorohectorite particles.

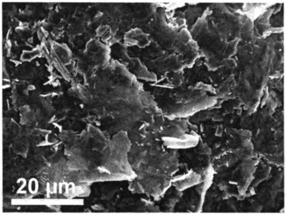

Figure 3.11 SEM micrograph of the choline$_{100}$-FH fabric film.

Table 3.2 Oxygen permeability data for epoxy-clay fabric film composites

Sample	Thickness of clay fabric film (mm)	Thickness of epoxy-clay composite film (mm)	Oxygen permeability (cc·mil/m^2·day)
Neat epoxy		0.20	98.9
Choline$_{100}$-PGW/Epoxy	0.050	0.074	110.7
D2000$_{60}$-PGW/Epoxy	0.071	0.103	440.8
D2000$_{20}$-PGW/Epoxy(1)[a]	0.038	0.049	6.70
D2000$_{20}$-PGW/Epoxy	0.038	0.061	< 0.1

[a] (1) represents the epoxy coating on the "air" side of the clay film has been peeled off, therefore, only one layer of epoxy coating exists on the "glass" side of the clay film.

Oxygen transmission rates of some epoxy-clay composite films are summarized in Table 3.2. In comparison with the neat epoxy, more than 3 orders of magnitude reduction in O$_2$ permeability was achieved by D2000$_{20}$-PGW/epoxy composite film, wherein the epoxy precursors diffuse efficiently into the clay fabric film, energetically favored by the covalent bond formation between the functional diprotonated D2000 onium ions on the clay exchange sites and the epoxy resin. After being cured, the crossed-linked epoxy polymer fills voids between clay platelet edges, which lead to the enhancement in the gas barrier property. Even after epoxy coating at the "air" side of $D2000_{20}$-PGW is peeled off the composite film, the remaining composite having one side of epoxy coating at the "glass" side retains the barrier property and exhibits 1 order and 3 orders of magnitude decrease in O_2 permeability with regard to the neat epoxy and the parent clay film, respectively.

In the preparation of the epoxy-clay composite film, the D2000 onium ions present in the clay films are not counted as being supplementary to the amino groups of curing agent Jeffamine D230. The fraction of epoxide groups capable of reacting with the diprotonated D2000 onium ions on the clay exchange sites is limited by stoichiometry to approximately ~3% in the $D2000_{20}$-PGW film. Therefore, this small amount of D2000 can be disregarded as contributing to the curing process. However, in the case of $D2000_{60}$-MMT/epoxy composite film wherein the "wetting mark" imperfection exists, the moles of onium ions present in the clay can react with around 15% of epoxy monomers. This large excess of amino groups may deteriorate the barrier property of the epoxy polymer. Thus, $D2000_{60}$-MMT/epoxy composite film is even 4 times more permeable than the neat polymer, whereas, oxygen permeability is reduced almost 15-fold compared to the parent clay film, which is again attributed to the organic components occupying the space between the clay particles. The resulting epoxy composite from choline onium ion fully exchanged montmorillonite film does not enhance the barrier property of the parent clay film as dramatically as $D2000_{20}$-PGW/epoxy. This can be rationalized by the unfavorable small interlayer spacing of $choline_{100}$-MMT (14.1 Å) which impedes the penetration of epoxy pre-polymers into the film interior. Therefore, epoxy polymer chains can only block the voids in the outer region of the clay film.

3.4 Summary

We have developed epoxy-clay fabric film composites with high O_2 gas barrier properties by impregnating self-supported clay fabric films with epoxy pre-polymers.[26] In order to improve the interfacial adhesion between the oriented clay particles and the epoxy matrix, homoionic organoclays and homostructured and heterostructured mixed inorganic-organic ion clay films were prepared. Naturally occurring Na^+-montmorillonite (MMT) and synthetic Li^+-fluorohectorite were exchanged with cetyltrimethylammonium (CTA^+), choline $(CH_3)_3N^+CH_2CH_2OH$, glycidyltrimethylammonium (GTA^+) and diprotonated primary α, ω-diamine $H_2NCH(CH_3)CH_2[OCH_2CH(CH_3)]_xNH_2$ (denoted Jeffamine D2000 with $x = 33.1$). In comparison with the parent inorganic clay films, which show no adhesion toward the epoxy matrix, CTA^+, choline and GTA^+ clay films present substantially improved interfacial adhesion. The large interlayer spacing of ~27 Å for CTA^+ organoclay (42% onium ion exchange) and the functional –OH and epoxide groups in choline and GTA^+, respectively, may facilitate the solvation of clay nanolayers by epoxy precursors and promote adhesion. Clay films partially exchanged by di-protonated Jeffamine D2000 provide the best adhesion to epoxy polymer and impart the high optical transparency. The di-protonated organocations play a dual role of organic modifier and curing agent for the thermoset epoxy matrix. Thus, the clay fabric films links to the epoxy matrix by forming covalent bond at the interface of the two phases. An interesting finding based on XRD and SEM-EDS measurements is that polymer adhesion improves with the increasing degree of clay platelet orientation at the surface of the fabric film. Also, fabric films assembled from fluorohectorite plates are very robust paper-like materials, whereas most of the organo-MMT films are very fragile. The difference in durability is correlated with the aspect ratio of the platelets. The pristine clay films are very permeable to oxygen due to the micro- to sub-micro size voids formed between clay nanolayer edges. However, the epoxy-clay fabric composite films show 3-4 orders of magnitude decrease in O_2 permeability with respect to the parent clay films. The enhancement in barrier properties is attributed to the efficient diffusion of epoxy monomer and curing agent into the clay film and to the blocking of the voids between clay platelet edges upon curing.

References

(1) Vaia, R., **AMPTIAC** *Newsletter* **2002**, *6*, 17.

(2) Jana, S. C.; Pattanayak, A. *Polymer* **2005**, *46*, 5183.

(3) Zhu, Z.; Yang, Y.; Yin, J.; Wang, X.; Ke, Y.; Qi, Z. *J. Appl. Polym. Sci.* **1999**, *73*, 2063.

(4) Zhu, Z.; Yang, Y.; Yin, J.; Wang, X.; Ke, Y.; Qi, Z. *Polymer* **1999**, *40*, 4407.

(5) Yano, K.; Usuki, A.; Okada, A.; Kurauchi, T.; Kamigaito, O. *J. Polym. Sci., Part A: Polym. Chem.* **1993**, *31*, 2493.

(6) Grunlan, J. C.; Grigorian, A.; Hamilton, C. B.; Mehrabi, A. R. *J. Appl. Polym. Sci.* **2004**, *93*, 1102.

(7) Saura, J. J.; Gavara, R.; Cabedo, L.; Gimenez, E. *Polymer* **2004**, *45*, 5233.

(8) Pinnavaia, T. J.; Lan, T.; Kaviratna, P. D. *Chem. Mater.* **1994**, *6*, 573.

(9) Khayankarn, O.; Magaraphan, R.; Schwank, J. W. *J. Appl. Polym. Sci.* **2003**, *89*, 2875.

(10) Yano, K.; Usuki, A.; Okada, A. *J. Polym. Sci., Part A: Polym. Chem.* **1997**, *35*, 2289.

(11) Chang, J.; Park, K. M.; Cho, D. *Polym. Eng. Sci.* **2001**, *41*, 1514.

(12) Nielson, L.E. *J. Macromol. Sci. (Chem.)* **1967**, *A1*, 929.

(13) Pinnavaia, T. J.; Wang, M. S. *Chem. Mater.* **1994**, *6*, 468.

(14) Pinnavaia, T. J.; Shi, H.; Lan, T. *Chem. Mater.* **1996**, *8*, 1584.

(15) Pinnavaia, T. J.; Triantafillidis, C. S.; LeBaron, P. C. *Chem. Mater.* **2002**, *14*, 4088.

(16) Pinnavaia, T. J.; Triantafillidis, C. S.; LeBaron, P. C. *J. Solid State Chem.* **2002**, *167*, 354.

(17) Pinnavaia, T. J.; Lan, T. *Chem. Mater.* **1994**, *6*, 2216.

(18) Pinnavaia, T. J.; Lan, T.; Kaviratna, P. D. *Chem. Mater.* **1995**, *7*, 2144.

(19) Giannelis, E. P.; Messersmith, P. B. *Chem. Mater.* **1994**, *6*, 1719.

(20) Pinnavaia, T. J.; Lan, T.; Kaviratna, P. D. *J. Phys. Chem. Solids* **1996**, *57*, 1005.

(21) Pinnavaia, T. J.; Wang, Z. *Chem. Mater.* **1998**, *10*, 1820.

(22) Jana, S. C.; Park, J. H. *Macromolecules* **2003**, *36*, 2758.

(23) Suter, U. W.; Osman, M. A.; Mittal, V.; Morbidelli, M. *Macromolecules*, **2004**, *37*, 7250.

(24) Osman, M. A.; Mittal, V.; Lusti, H. R. *Macromol. Rapid Commun.* **2004**, *25*, 1145.

(25) Kim, J.; Hu, C.; Woo, R. S. C.; Sham, M. *Composites Science and Tech.* **2005**, *65*, 805.

(26) Pinnavaia, T. J.; Triantafyllidis, K. S.; LeBaron, P. C.; Park, I. *Chem. Mater.* **2006**, *18*, 4393.

(27) Pinnavaia, T. J.; IJdo, W. L. *Green Chem.* **2001**, *3*, 10.

4.1

rec

co

90

(N

sy

c

(t

c

(

CHAPTER 4

Synthesis and Characterization of Cancrinite, Saponite and Their Phase Mixtures

4.1 Introduction

The synthesis of smectite clay minerals has drawn much attention in recent years in order to provide derivatives of high purity and adjustable composition.[1-6] Vogels and co-workers first reported the synthesis of saponites at 90°C from a silica-alumina gel and a solution containing urea and an M^{2+}-nitrate (M^{2+}=Mg, Zn, Ni, Co).[6] Compared to naturally occurring smectite-type clays, synthetic saponites exhibit improved catalytic activity and selectivity as acid catalysts for alkylation due to the small and uniform size of clay platelets (typically less than 50 nm), disordered nanolayer stacking, and controllable chemical compositions that result in excellent transport properties of organic compounds. Recently, it has been found by Xue[7] that synthetic Mg-saponite based on Vogels's methods improves the tensile properties of both rubbery and glassy epoxy matrices without the need for the organic modification of the clay surface.

Cancrinite (CAN) is found in nature as a porous zeolite with the composition $Na_6Ca[AlSiO_4]_6CO_3(H_2O)_2$.[8] The cancrinite framework is easily built from ABAB stacking of hexagonal arrays of 6-membered rings of SiO_4 and AlO_4 tetrahedra along the *c*-axis (see Figure 1.14).[9,10] Small 11-hedral cages (ε-cages) and a big 12-ring channel along the [001] direction are the results of this arrangement of sheets. Isomorphous positioning of aluminum in tetrahedral coordination results in negative charges on the framework counterbalanced by cations held within the cavities and channels. The big open channels host Na^+ and Ca^{2+} cations, as well as CO_3^{2-} and other anions, while the ε-cages contain chains of alternating charge-balancing cations and water molecules.[11,12]

A few researches have been reported on the synthesis of cancrinite under mild hydrothermal conditions. Preparation of large amounts of pure-phase canrinite can be difficult due to the formation of disordered cancrinite and an intermediate phase between cancrinite and sodalite, and the co-crystallization of sodalite.[9,10,13-19] Pure nitrate cancrinite crystals less than 100 nm in length were prepared by Navrotsky et al.[20,21] based on a simple synthetic route at 90°C, without the formation of intermediate phase or sodalite. This can be attributed to the difference in concentrations of the starting solutions and the fact that no crystalline precursors (e.g. kaolinite, zeolite A) were used in their synthesis process, unlike previously reported synthesis.[9,10,13-17]

We report herein the investigation of the synthesis of Mg-saponite (denoted SAP) using sodium hydroxide instead of urea as base source, which represents an economic benefit. Pure delaminated SAP platelets can be achieved at low NaOH concentration at 90°C. Interestingly, with increasing alkalinity, new phases were formed along with the co-crystallization of saponite. Garronite (GIS framework type zeolite) first emerged together with saponite when the NaOH concentration was doubled. Then cancrinite (denoted CAN) was co-crystallized along with saponite upon further increasing the alkalinity.

Another purpose of the present work is to investigate the low-temperature synthesis of single-phase cancrinite. Therefore, we also investigated the impact of Mg^{2+} concentration on saponite and cancrinite phase formation, as well as the effect of Si/Al ratios in the initial liquor on the average crystal dimensions of cancrinite material. With decreasing Mg amount, the crystallinity of cancrinite is improved. Also, a higher fraction of cancrinite appears in the product mixtures. Upon eliminating Mg^{2+} entirely from the synthesis gel, singe-phase cancrinite with rod-like morphology up to several μm in length was synthesized. Decreasing the Si/Al ratio tends to facilitate the growth of smaller CAN crystals (~ 100 nm). The chemical composition of cancrinite is also dependent on the Si/Al ratio within the synthesis gel.

4.2 Experimental

4.2.1 Materials

Sodium silicate containing 27 wt.% SiO_2 and 14 wt.% NaOH and $Al(NO_3)\cdot 9H_2O$ were purchased from Aldrich Chemical Co.. $Mg(NO_3)_2.6H_2O$ was purchased from Columbus Chemical Industries, Inc.. All other chemicals were purchased from Aldrich Chemical Co. and used without further purification.

4.2.2 Saponite Synthesis

Synthetic saponite was prepared at 90°C according to previously described methods[6] using water glass solution (27 wt.% silica, 14 wt.% NaOH),

$Al(NO_3)_3{\cdot}9H_2O$, $Mg(NO_3)_2{\cdot}6H_2O$ and NaOH as the source of base. The molar ratio of Si : Al : Mg : NaOH (not including NaOH in water glass solution) is 3.6 : 0.4 : 3.0 : 5 per 400 moles of water.

In a typical synthesis, 5.50 g of sodium silicate solution (0.02475 mol silica) and 1.031 g (0.00275 mol) of $Al(NO_3){\cdot}9H_2O$ were mixed in 49.5 g of deionized water at room temperature for 1.5 h. Then 1.37 g (0.03425 mol) of NaOH was introduced to the white suspension, followed by another 1.5 h of stirring at room temperature. The mixture was then brought to 90°C and heated under stirred condition for 30 min, followed by the introduction of 5.28 g (0.0206 mol) of $Mg(NO_3)_2{\cdot}6H_2O$. The mixture was refluxed under stirring at 90°C for 24 h in a 250 mL flask. After that, the product was centrifuged, triple washed with deionized water, and dried at 80°C under N_2 flow.

4.2.3 Synthesis of Phase Mixture of Saponite and Cancrinite

The synthesis steps are similar to those for saponite synthesis, except that various amounts of sodium hydroxide and magnesium nitrate are used to investigate the influence of concentration on the saponite to cancrinite product ratio. The reactions were performed at different time periods ranging from 24 h to 168 h.

4.2.4 Cancrinite Synthesis

Synthetic cancrinite was prepared at 90ºC using water glass solution (27 wt.% silica, 14 wt.% NaOH), $Al(NO_3)_3{\cdot}9H_2O$, and NaOH. The molar ratio of Si : Al : NaOH (not including NaOH in water glass solution) is x : 0.4 : 30 per 400 moles of water for x = 3.6, 2.4, 1.6, 0.8, 0.4. The mixture was refluxed under stirring at 90°C for reaction periods of 72 and 168 h. After that, the product was centrifuged, triple washed with deionized water, and dried at 80°C under N_2 flow.

4.2.5 Characterization

X-ray diffraction (XRD) patterns were obtained on a Rigaku rotaflex 200B diffractometer equipped with Cu Kα X-ray radiation and a curved crystal graphite monochromator, operating at 45 kV and 100 mA. Powder samples were pressed onto a glass X-ray sample holder.

N_2 adsorption-desorption isotherms were recorded at -196°C on a Micrometritcs Tristar 3000 sorptometer. Prior to analysis samples were outgassed at 150°C and 10^{-6} Torr for a minimum of 12 h. BET surface areas were calculated from the linear part of the BET plot and BJH pore sizes were obtained from adsorption isotherms.

Transmission electron microscopy (TEM) images were obtained on a JEOL 2200FS field emission microscope with a ZrO/W Schottky electron gun and an accelerating voltage of 200 kV. The powdered samples were sonified in ethanol, and dripped onto 300 mesh copper grids.

^{29}Si and ^{27}Al MAS NMR spectra were obtained at 79 MHz on a Varian VXR-400S solid-state NMR spectrometer equipped with a magic angle-spinning probe. Sample was spun at 4 kHz for each measurement. The pulse delay for ^{29}Si MAS NMR was 400 s, and chemical shifts were referenced to talc. The pulse delay for ^{27}Al MAS NMR was 0.50 s, and a 0.10 M aqueous $Al(NO_3)_3$ solution was used as the chemical shift reference. FTIR spectra of samples dispersed in KBr disks were recorded at ambient temperature on a Mattson Galaxy 3000 FTIR spectrometer over the range 400-4000 cm^{-1}.

4.3 Results and Discussion

The wide angle *hkl* X-ray diffractions demonstrate the phase transition sequence of saponite-garronite-cancrinite at 90°C as a result of increasing the NaOH concentration in the starting solutions (Figure 4.1). The characteristic 001

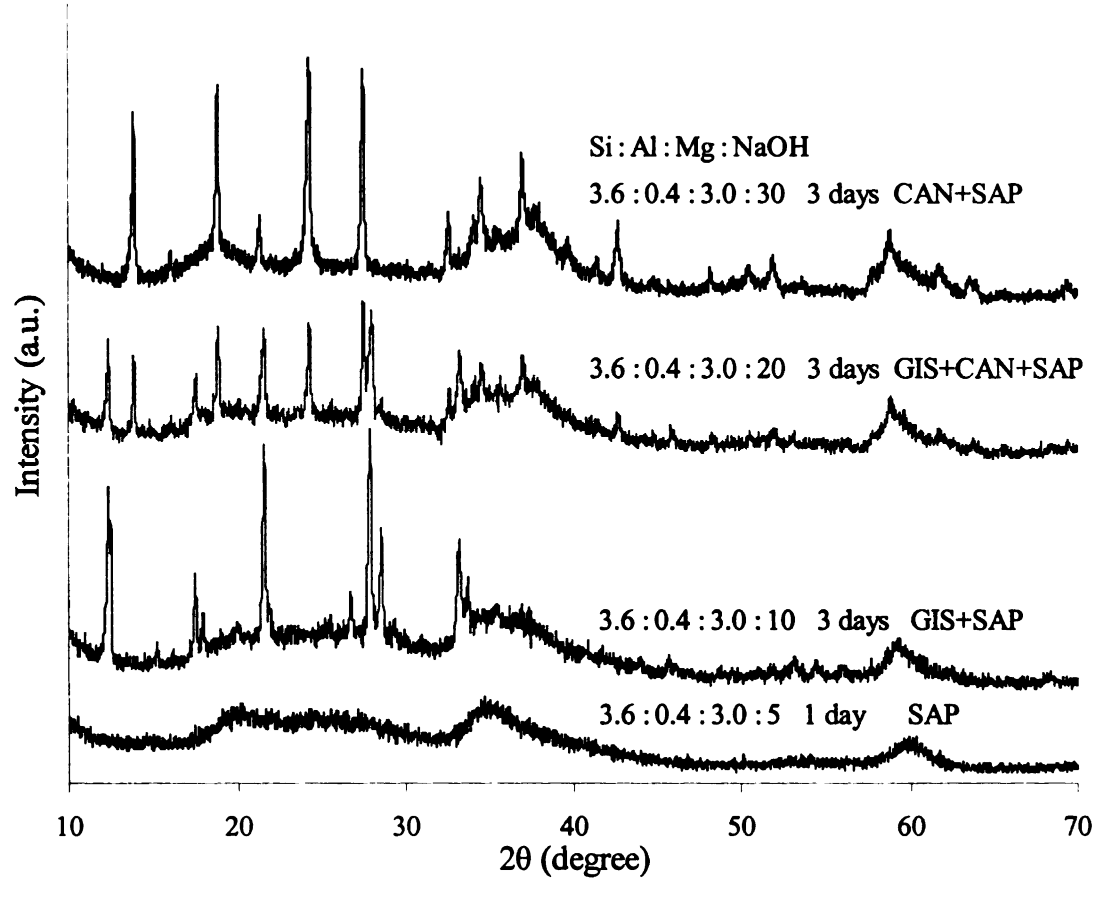

Figure 4.1 XRD patterns showing different crystalline product formation as a function of increasing alkalinity at 90°C. The ratios represent the stoichiometry of Si:Al:Mg:NaOH in the starting solutions.

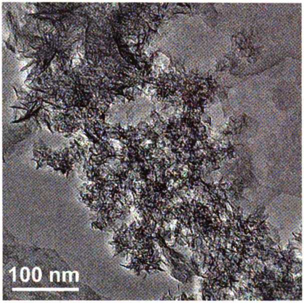

Figure 4.2 TEM image of synthetic SAP formed at 90°C after a reaction time of 1 day.

reflection is absent for saponite clay, indicating the absence of regular platelet stacking. SAP has small platelets with dimension of 20-30 nm with almost no stacking, as shown by the TEM image in Figure 4.2. When the NaOH concentration is doubled, a new phase garronite (denoted GIS) forms along with SAP. The co-crystallization of saponite is verified by the presence of an in-plane 060 reflection characteristic of clay. Garronite is replaced completely by cancrinite upon increasing the NaOH concentration six-fold. Increasing the NaOH concentration four-fold results in the formation of three phases, namely, garronite, saponite and cancrinite. Further increasing the alkalinity results in a reduction of crystallinity and a higher amorphous background in the X-ray patterns for the CAN/SAP phase mixture (not shown here). Therefore, in all subsequent studies of this phase mixture, the molar ratios of Si:NaOH are maintained at 3.6:30.

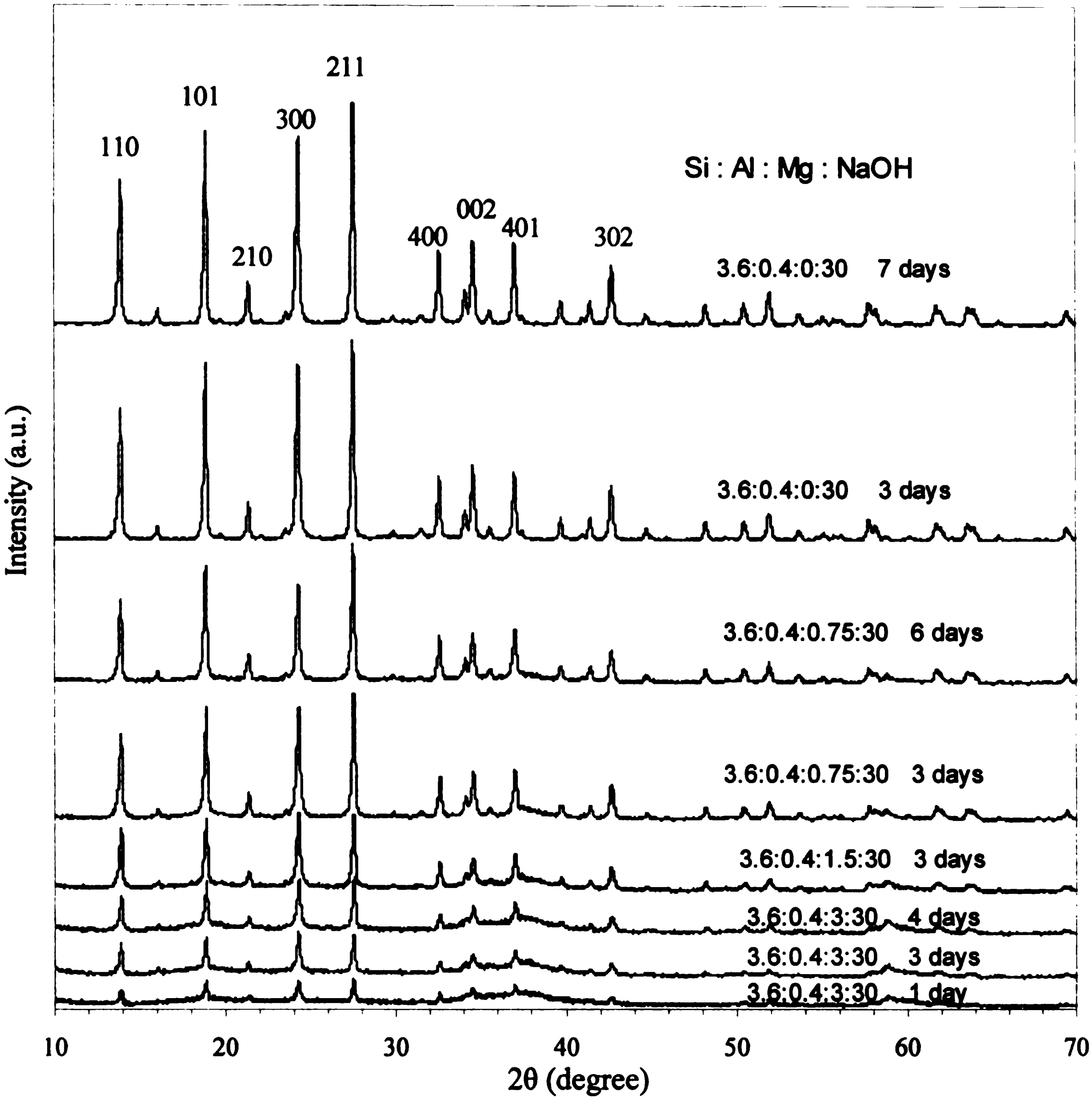

Figure 4.3 XRD patterns of crystalline products formed upon decreasing the $Mg(NO_3)_2$ content of the reaction mixture. For each product, the molar ratios of Si:Al:Mg:NaOH in the synthetic solutions are labeled, as well as the reaction time at 90°C.

The effect of magnesium nitrate concentration on the phase formation was also studied. The X-ray diffraction patterns of the crystalline products formed at different Mg ion concentrations are shown in Figure 4.3. With decreasing the Mg amount in the initial reaction liquor, the intensities of the reflection peaks from cancrinite increase, indicating a significant improvement in the crystallinity of cancrinite, as well as higher proportion of cancrinite in the CAN/SAP phase mixture. The existence of saponite in the products together with cancrinite can be easily seen from TEM images (Figure 4.4 and Figure 4.5). Figure 4.4 parts a and b show that after 4 days of aging, rod-like crystals of cancrinite with several hundred nm in length emerge together with platy saponite particles. These crystals were formed from the starting Si:Al:Mg:NaOH stoichiometry of 3.6:0.4:3:30. Evidence supporting the presence of amorphous silica in the product mixture, as suggested by the high background in the X-ray powder patterns shown in Figure 4.1, is provided by the TEM image of Figure 4.4 c. A TEM-XEDS analysis of this selected area indicated a Si:O molar ratio of 33.15:66.85, in agreement with pure silica. When the magnesium nitrate concentrations were reduced to half and one fourth, co-crystallization of saponite platelets is still observed in TEM imagings (Figure 4.5 a, b, c and d). Until completely removing magnesium nitrate from the starting reaction solutions, no SAP nanolayers are observed in the reaction product (cf. Figure 4.6 a, b, and c), suggesting the formation of pure-phase cancrinite. Moreover, some cancrinite crystallites have grown to a rather large size of several micrometers in length after a 7 day reaction period.

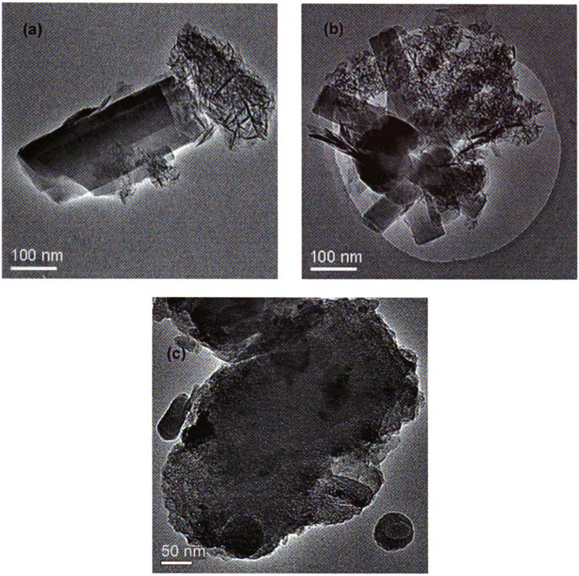

Figure 4.4 TEM images of CAN/SAP phase mixture formed from a reaction stoichiometry of Si:Al:Mg:NaOH=3.6:0.4:3:30 at 90ºC after a reaction time of 4 days, and the corresponding ratios of Si/Al=9, Mg/(Si+Al)=0.75, and OH^- /(Si+Al+Mg)=4.3.

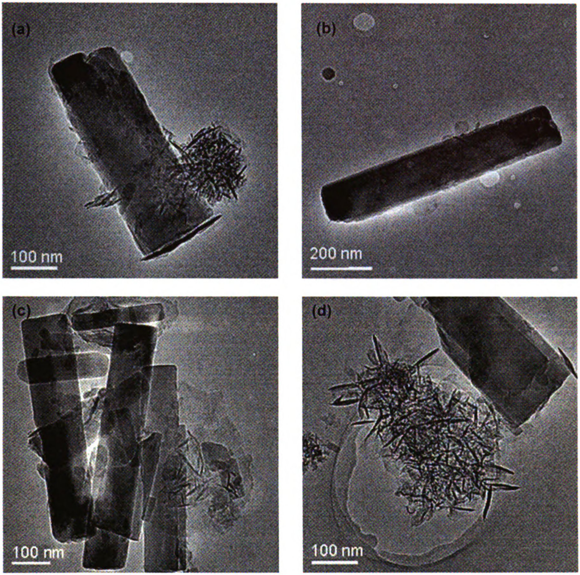

Figure 4.5 TEM images of CAN/SAP phase mixtures formed at 90ºC after a reaction time of 3 days. (a) and (b) are for the CAN/SAP mixture made from starting materials with the composition Si:Al:Mg:NaOH=3.6:0.4:1.5:30, and the corresponding ratios of Si/Al=9, Mg/(Si+Al)=0.375, and OH^-/(Si+Al+Mg)=5.45; (c) and (d) are for the CAN/SAP mixture made from Si:Al:Mg:NaOH=3.6:0.4:0.75:30, and the corresponding ratios of Si/Al=9, Mg/(Si+Al)=0.188, and OH^-/(Si+Al+Mg)=6.32.

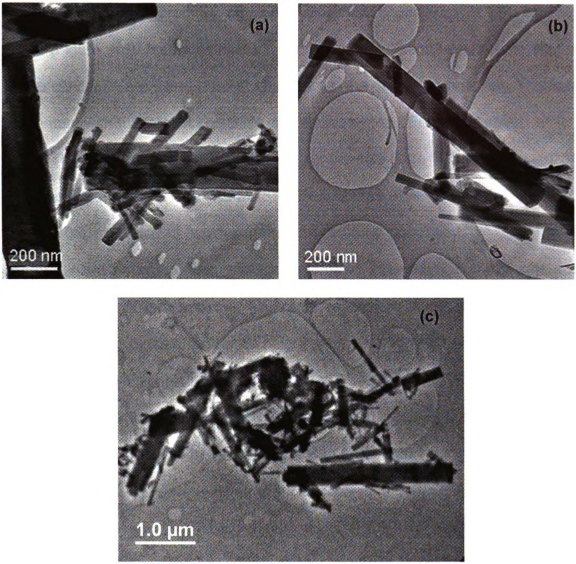

Figure 4.6 TEM images of single-phase cancrinite formed from a reaction stoichiometry of Si:Al:Mg:NaOH=3.6:0.4:0:30 at 90ºC after a reaction time of 7 days, and the corresponding ratios of Si/Al=9, Mg/(Si+Al)=0, and OH^- /(Si+Al+Mg)=7.5.

The full width at half maximum (FWHM) of the reflection peaks were measured and compared for cancrinite materials crystallized at different Mg levels (Figure 4.3). It's found that the widths of the diffraction peaks for single-phase cancrinite are the narrowest among all of the cancrinite products. This is in agreement with the largest crystallite size, found by the TEM observation.

The lattice structure of saponite and cancrinite were further characterized using solid state NMR. The ^{29}Si MAS NMR spectrum of saponite (cf. Figure 4.7) exhibits the presence of two resonances. The -85.4 ppm line is assigned to Si centers linked through bridging oxygen atoms to three tetrahedral Si ions and one tetrahedral Al ion, and the -92.7 ppm resonance is ascribed to Si linked through bridging oxygen to four Si neighbors. The ^{27}Al MAS NMR spectrum of SAP contains two signals at chemical shifts of 61.6 ppm and 10.5 ppm, indicating that Al substitution occurred in both tetrahedral and octahedral sheets of the 2:1 layered silicate structure. In the case of a CAN/SAP phase mixture, ^{29}Si and ^{27}Al solid state NMR may give qualitative information as to the relative proportions of the phases present. The sharp signal at -87.3 ppm correlates well with the alternating ordering of the framework Si and Al atoms in cancrinite crystals. The shoulder line at -92.7 ppm might be from saponite, or the formation of Si-rich cancrinite, wherein the Si/Al ratio is more than 1 and some of the silicon centers are linked through bridging oxygen to three Al and one Si. The latter assignment of -92.7 ppm resonance is verified by the quantitative analysis of cancrinte particles in the mixed CAN-SAP phase carried out by XEDS-TEM (cf. Figure 4.8), indicating a Si/Al ratio of 1.25. Moreover, according to X-ray analysis, small

Figure 4.7 ^{29}Si and ^{27}Al MAS NMR spectra of (a) SAP formed after 1 day reaction time (3.6:0.4:3:5), (b) CAN/SAP phase mixture formed after a reaction time of 4 days (3.6:0.4:0.75:30) and (c) pure CAN made after 3 days (3.6:0.4:0:30). The ratio in the parentheses represents the molar ratio of Si:Al:Mg:NaOH in the starting solution. The asterisks indicate spinning sidebands.

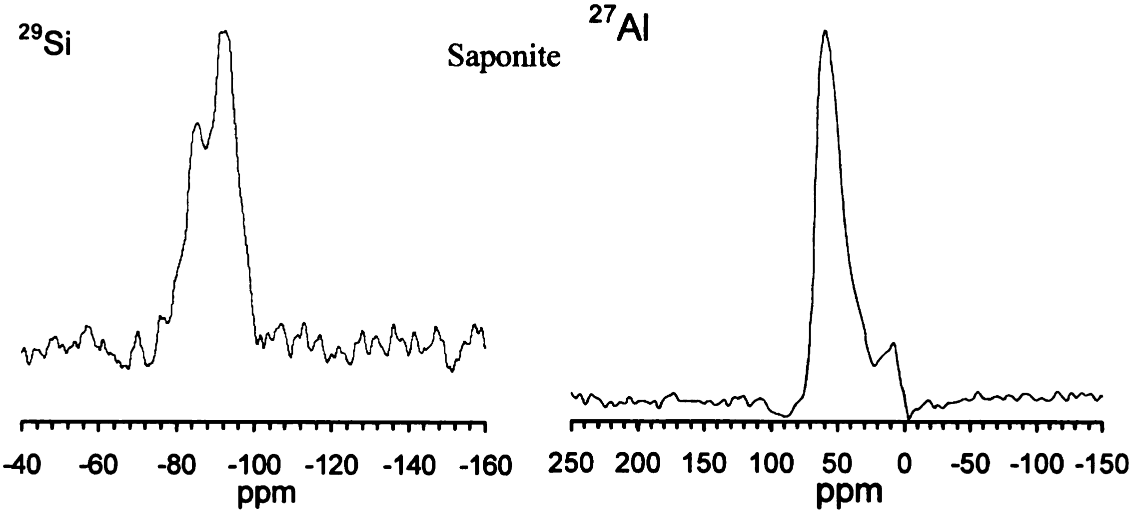

Saponite

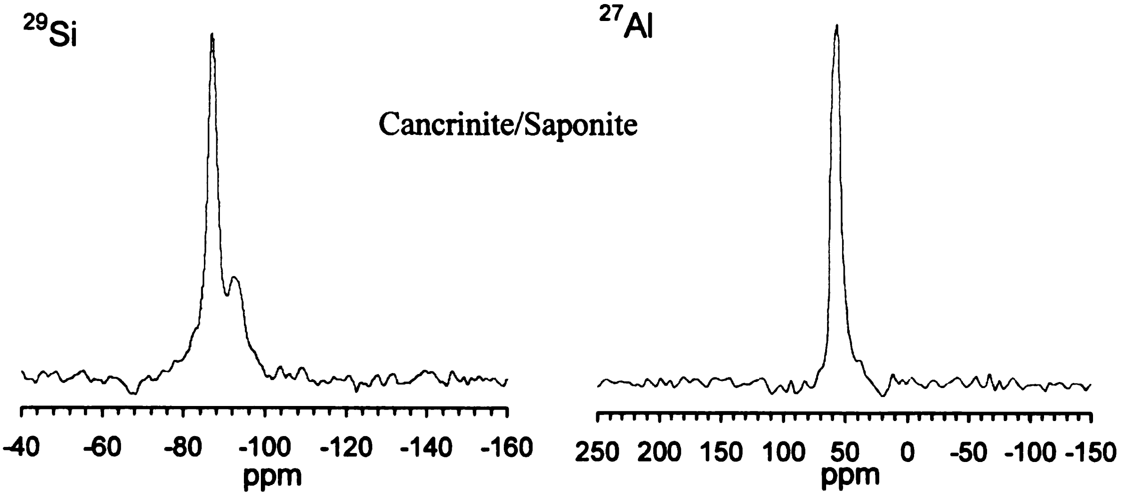

Cancrinite/Saponite

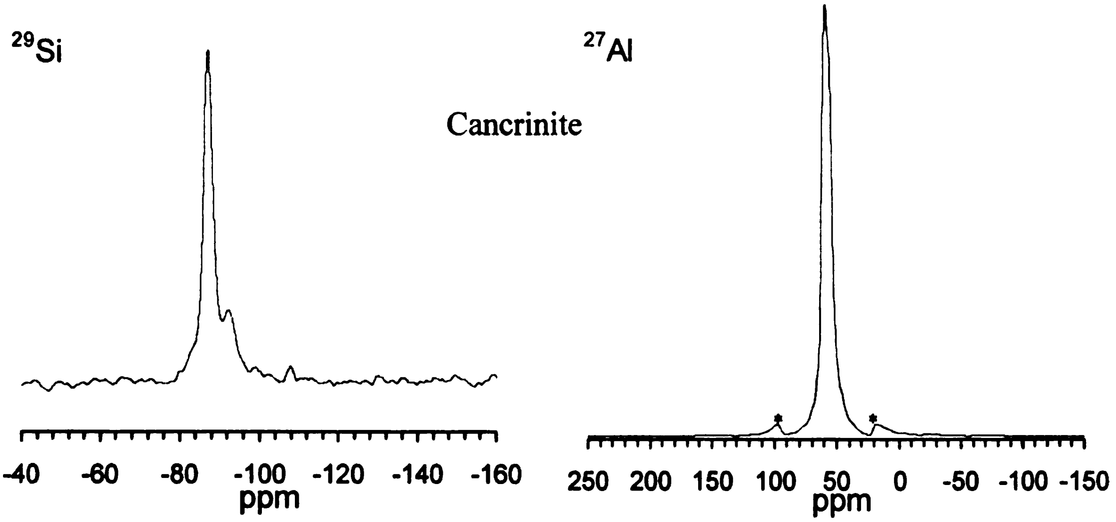

Cancrinite

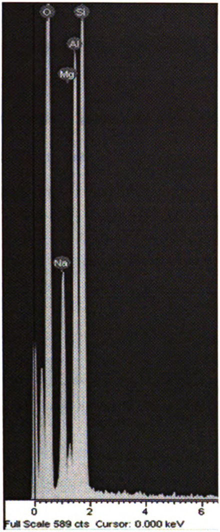

Element	Weight%	Atomic%
O K	44.61	57.09
Na K	11.17	9.95
Mg K	1.57	1.32
Al K	18.56	14.09
Si K	24.08	17.55
Totals	100.00	

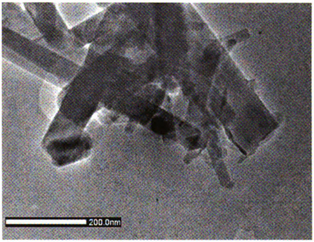

Figure 4.8 TEM image and X-ray energy dispersive spectrum (XEDS) of cancrinite crystals in the CAN/SAP phase mixture formed from a reaction mixture with the composition Si:Al:Mg:NaOH=3.6:0.4:0.75:30 after 4 days. Unlabeled peaks are from copper grid and carbon film. Quantitative analysis result is summarized in the inserted table and note the Si/Al=1.25.

amounts of magnesium are also incorporated into the cancrinite framework structure in addition to sodium cations. The ^{27}Al MAS NMR spectrum only exhibits a single line at 57.1 ppm for the aluminum in tetrahedral coordination.

The fact that a resonance for aluminum in octahedral coordination is absent suggests a low saponite population in the CAN/SAP phase mixture. The ^{29}Si MAS NMR spectrum of pure cancrinite shows the same two resonances as in CAN/SAP, and in this case the two resonances arise because a large excess of silica in the reaction mixture with Si/Al=9 facilitates the formation of a Si-rich cancrinite.

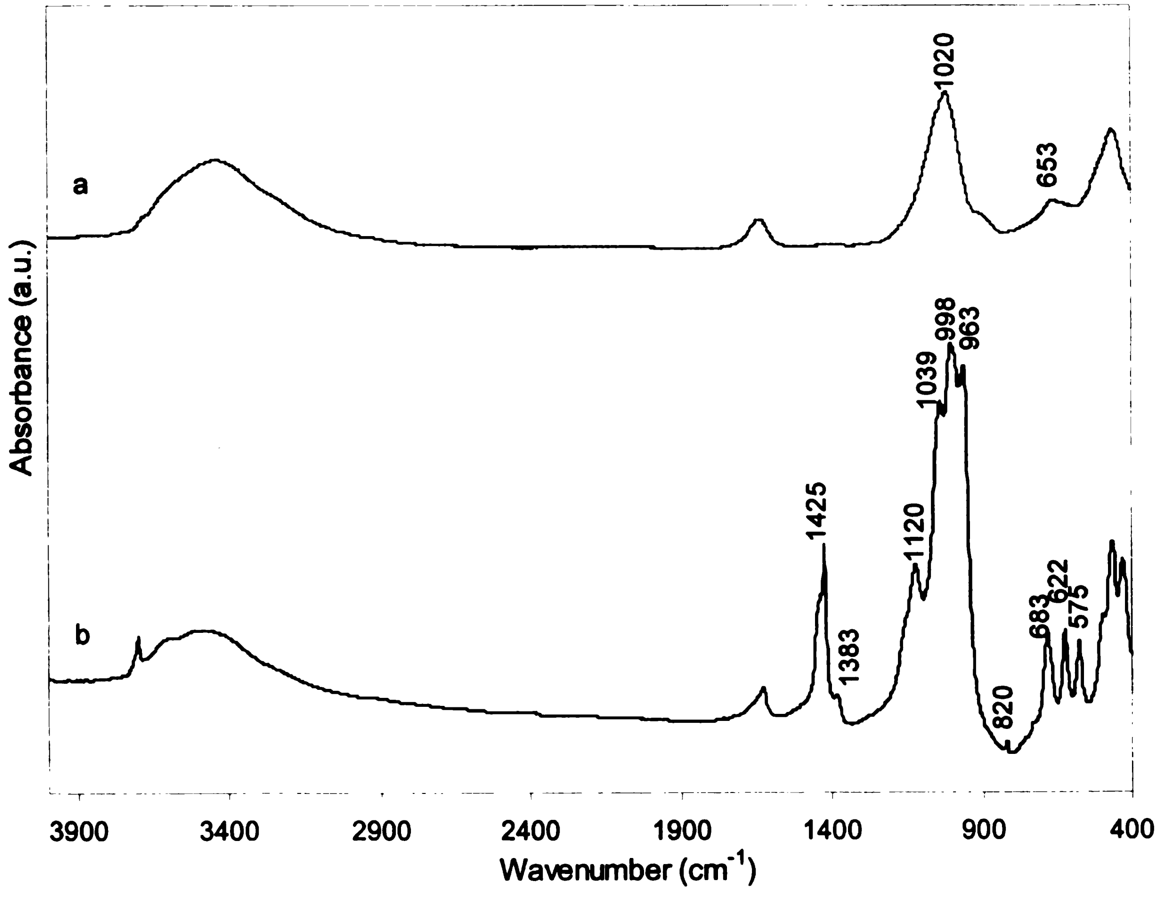

Figure 4.9 FTIR spectra of (a) pure saponite after 1 day of aging from initial solutions with a Si:Al:Mg:NaOH stoichiometry at 3.6:0.4:3:5, and (b) CAN/SAP phase mixture after 4 days of aging from initial solutions with a Si:Al:Mg:NaOH stoichiometry at 3.6:0.4:0.75:30.

The FTIR spectra of pure SAP and CAN/SAP phase mixture are compared in Figure 4.9. The water bending mode around 1630 cm^{-1} and a broad OH stretching band between 3100 and 3600 cm^{-1} are found in both samples. The IR spectroscopic result of pure saponite shows absorption bands at 1020 and 653 cm^{-1}, clearly indicating the typical asymmetric and symmetric T-O-T vibrations. The vibrations of the cancrinite phase dominate the IR spectrum of the CAN/SAP phase mixture (cf. Figure 4.9 b). For nitrate cancrinite the absorbance for the asymmetric stretch $\nu_{Al\text{-}O}$ for the Al-O-Si framework is split into four peaks at 1120, 1039, 998 and 963 cm^{-1}. The region of 400-800 cm^{-1} is known as the "fingerprint" region.[17] The characteristic fingerprint peaks for cancrinite occur at approximately 575, 622, 683, and 770 cm^{-1}. In addition to the weak bending mode near 820 cm^{-1}, the presence of nitrate groups in the zeolite channels can be better detected by the strong ν_{as} vibration at 1425 cm^{-1}. The weak absorption at 1383 cm^{-1} has been attributed to small amounts of precipitated sodium nitrate the outer surface of the crystals.[22] Another potential occluded anion for our cancrinite structure is CO_3^{2-}. This ion may form through the reaction of atmospheric CO_2 with the highly concentrated NaOH in the reaction mixture. However, carbonate was not incorporated to a detectable extent because the two CO_3^{2-} stretching bands[9] at 1410 and 1455 cm^{-1} are not observed here, indicating that NO_3^- is the major anion in the channels of the cancrinite structure. Cancrinite vibrations almost completely mask the vibrations of the minor saponite phase. This further confirms the low proportion of saponite in the phase mixture, which is consistent with the ^{29}Si and ^{27}Al MAS NMR results.

Table 4.1 Textural properties of saponite, cancrinite and CAN/SAP phase mixtures

Product	Si:Al:Mg:NaOH ratio of reaction mixture	Reaction time (days)	BET surface area (m^2/g)	Total pore volume (cm^3/g)	BJH adsorption pore size (nm)
SAP	3.6:0.4:3:5	1	875	1.54	1.8
CAN/SAP	3.6:0.4:3:30	3	329	0.42	1.4
CAN/SAP	3.6:0.4:1.5:30	3	227	0.39	1.8
CAN/SAP	3.6:0.4:0.75:30	3	134	0.31	2.0
CAN	3.6:0.4:0:30	7	10.2	0.068	-
CAN	3.6:0.4:0:30	3	8.9	0.060	-
CAN	2.4:0.4:0:30	3	21.8	0.14	-
CAN	1.6:0.4:0:30	3	40.0	0.17	-
CAN	0.8:0.4:0:30	3	36.6	0.17	-
CAN	0.4:0.4:0:30	3	21.3	0.095	-

BET surface areas and pore volumes of single-phase saponite and cancrinite, and CAN/SAP phase mixtures are summarized in Table 4.1. The N_2 adsorption-desorption isotherms (Figure 4.10) show a Type H3 hysteresis loop for pure saponite. The BET surface area and pore volume of the pure saponite is 875 m^2/g and 1.54 cm^3/g, respectively, resulting from the irregular stacking and small in-plane dimension of clay platelets.

The pore aperture in the cancrinite framework structure is 5.9×5.9 Å, which is big enough for the access of N_2 molecules. But the presence of intercalated nitrate anions in CAN severely blocks the big channels and prevents N_2 molecules from accessing the interior of the pores. This accounts for the low uptake of N_2, as reflected in the gas adsorption isotherm behavior of pure cancrinite (Figure 4.10). The very low surface area of pure cancrinite zeolite

(10.2 m^2/g) is due to adsorption on the external surfaces of large particles up to several *u*m in length (Figure 4.6 a, b and c). As expected, CAN/SAP phase mixtures have the surface area between the pure saponite and cancrinite. Moreover, lower surface area of CAN/SAP (134 m^2/g) made from a reaction mixture with the composition Si:Al:Mg:NaOH=3.6:0.4:0.75:30 illustrates the higher population of CAN in this phase mixture in comparison to that of CAN/SAP with higher surface area of 227 or 329 m^2/g.

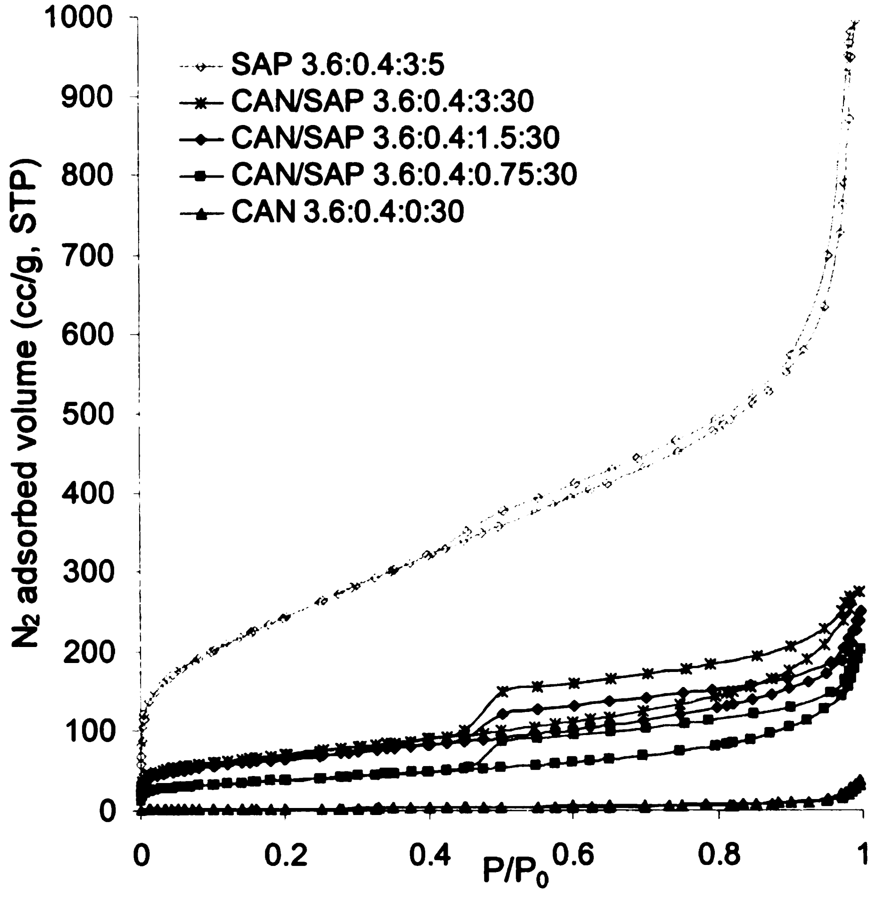

Figure 4.10 N_2 adsorption-desorption isotherms of pure saponite and cancrinite, and their phase mixtures. The ratios represent the molar ratios of Si:Al:Mg:NaOH in the reaction mixtures. The reaction time for pure saponite is one day and all the other products are made after a reaction period of 3 days.

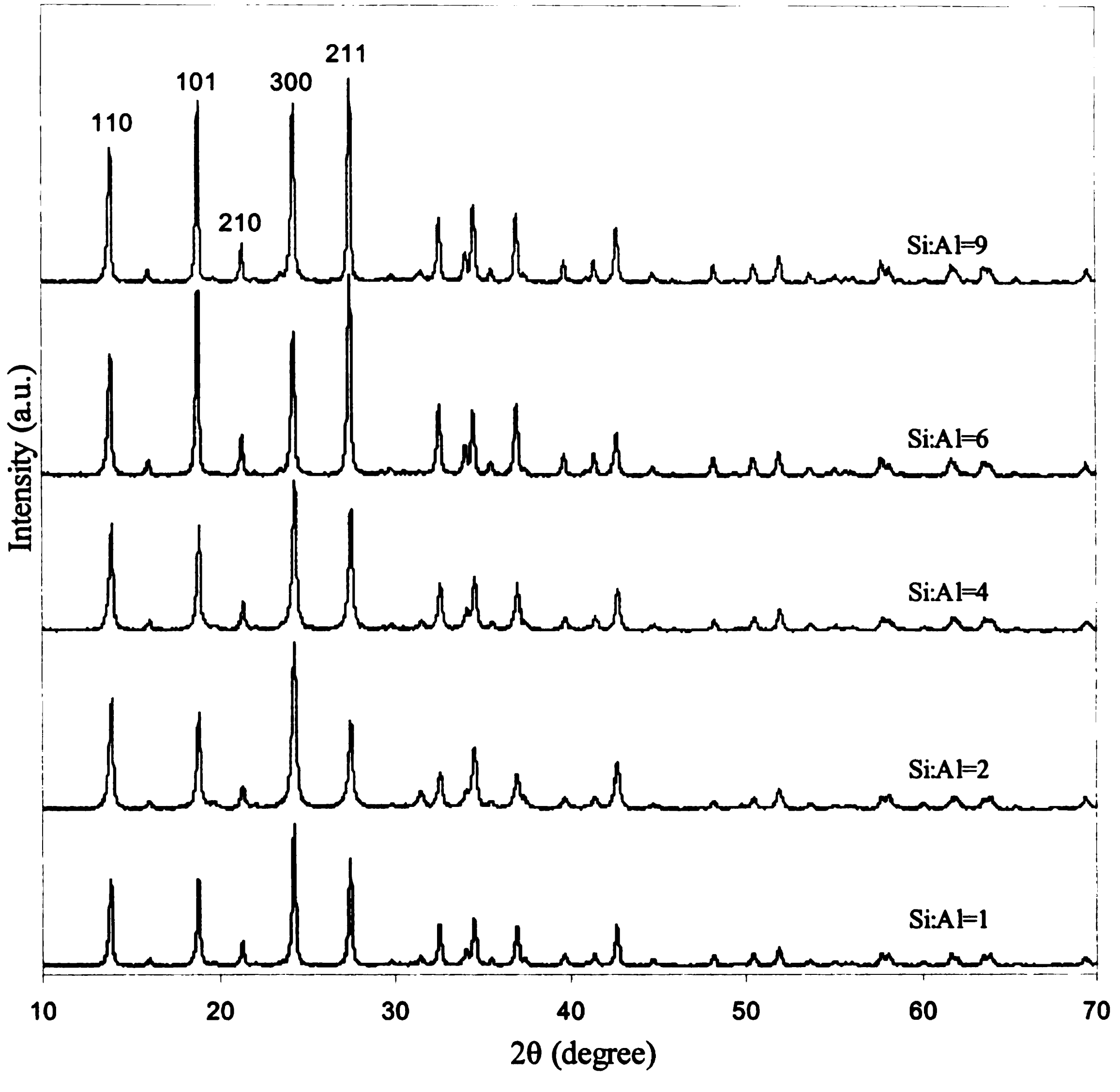

Figure 4.11 XRD patterns of cancrinite products formed as a function of the Si/Al ratio within the starting system after 3 days of reaction time under Mg-free condition.

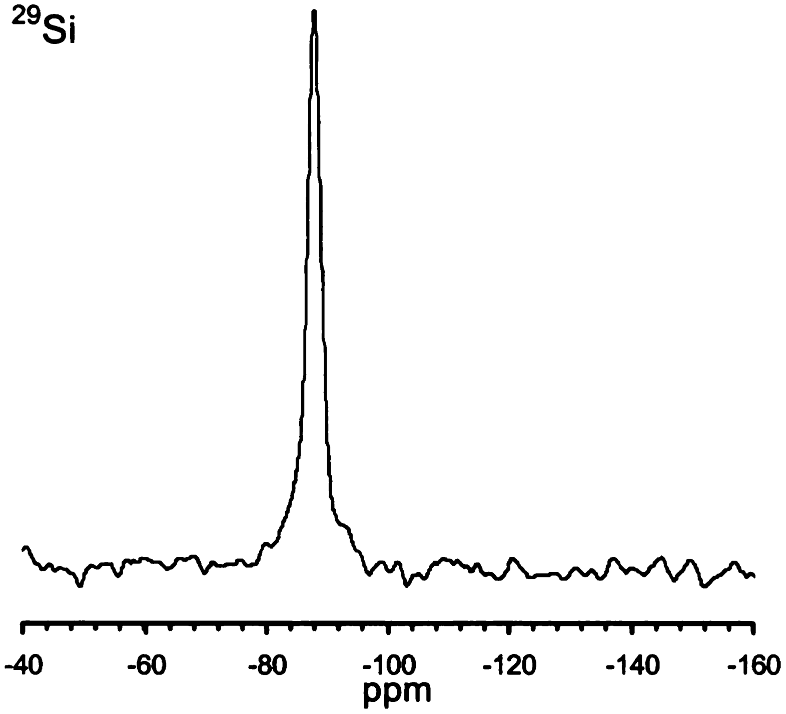

Figure 4.12 ^{29}Si MAS NMR spectrum of pure cancrinite synthesized from the educts with the composition of Si:Al:NaOH=1.6:0.4:30 under Mg-free condition.

Additional experiments were performed at various Si/Al ratios of 6, 4, 2 and 1 within the starting reaction mixtures. Powder XRD patterns of crystals of cancrinites formed at different Si/Al ratios after 3 days reaction time are shown in Figure 4.11. For each reaction, the molar ratio of Al:NaOH was maintained at 0.4:30. It can be seen that relative peak intensities are dependent upon the Si/Al ratio. For example, the relative intensity of the 300 peak decreases in comparison to the 101 and 211 reflections as the Si/Al ratio is increased from 1.0 to 9.0. This result most likely reflects a varying chemical composition of cancrinite crystals. As discussed before, a large excess of silica facilitates the formation of Si-rich cancrinites, which may be the case for Si/Al=9 and 6. XEDS-TEM analysis reveals a Si/Al ratio of 1.02 for cancrinite formed from a reaction mixture with Si/Al=4, which is very close to the ratio expected for the alternating occupation of tetrahedral sites by Si and Al. As a result of the $Si(OAl)_4$ framework building units, a single ^{29}Si line at -87.3ppm is found (Figure 4.12) for cancrinite grown from a reaction mixture with a Si/Al ratio of 4.

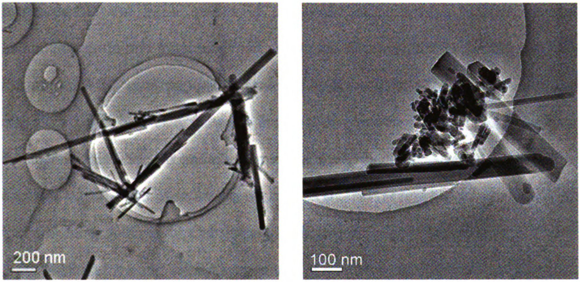

Figure 4.13 TEM images of cancrinite crystals formed at Si:Al:NaOH=1.6:0.4:30 under Mg-free condition.

The Si/Al ratios in the reaction mixture also have an influence on the textural properties of cancrinite products. As can be seen from Table 4.1, the effect of the Si/Al ratio on the surface areas and pore volumes is significant. Cancrinites prepared at a Si/Al ratio of 9 and 4 exhibit the largest differences in textural characteristics. TEM investigations of products made at Si/Al=4 show a large number of small crystals of cancrinite less than 100 nm in length, along with large needle-like crystals up to several micrometers in length (cf. Figure 4.13). The increased fraction of small crystallites explains the comparatively high surface area of 40 m^2/g.

4.4 Summary

The synthesis of saponites was carried out at 90°C using sodium hydroxide as the base source in a mixed gel containing sodium silicate, aluminum nitrate and magnesium nitrate. At low alkalinity corresponding to a OH^-/Si ratio of 1.39, pure saponite with small in-plane dimension of 20-30 nm and disordered stacking is achieved. The use of NaOH as a base represents a significant cost-effective improvement over the previously reported synthesis of saponite which used urea as the base source[6]. The present work demonstrates that the slow release of OH^- through the thermal hydrolysis of urea is not a prerequisite for the nucleation and growth of saponite nanolayers. Equivalent 2:1 layered silicate nanolayers are obtained through the direct addition of hydroxide ions to the reaction mixture.

In an effort to improve the layer aspect ratio and stacking order of the saponite nanolayers, the NaOH concentration in the reaction mixture was increased over the range $OH^-/Si=2.78$ to 8.33. However, some new zeolite phases appear along with saponite upon increasing alkalinity. Garronite first emerged together with saponite when the NaOH concentration was doubled ($OH^-/Si=2.78$). Increasing the NaOH concentration by six-fold ($OH^-/Si=8.33$) results in the co-crystallization of cancrinite with saponite. This finding represents the first example of the direct synthesis of a cancrinite-saponite phase mixture.

The appearance of garronite and cancrinite as co-products demonstrates that these aluminosilicate phases compete kinetically with the nucleation of saponite. The depletion of silicon and aluminum due to garronite or cancrinite formation leaves the reaction mixture rich in magnesium. The enrichment in magnesium allows the nucleation of saponite to compete with the nucleation of the zeolite phases.

The concentration of magnesium ions also has an influence on the formation of mixed CAN-SAP phase. Decreasing the $Mg(NO_3)_2$ amount leads to an improvement of crystallinity of cancrintie and a higher proportion of cancrinite in the CAN/SAP phase mixture, as evidenced by the increased intensities of diffraction peaks from cancrinite in the X-ray powder patterns. Removing Mg^{2+} completely from the reaction mixture results in the formation of single-phase cancrinite with rod-like morphology up to several μm in length. Moreover, both ^{29}Si MAS NMR and composition analysis indicate the formation of Si-rich cancrinite, wherein the Si/Al ratio in the CAN framework structure is greater than 1.0. This can be explained by the fact that a large excess of silica within the synthesis solution with Si/Al=9 facilitates the crystallization of a Si-rich cancrinite. Additional experiments were performed at various Si/Al ratios of 6, 4, 2 and 1 to study the effect of the Si/Al ratio on the chemical composition, as well as the textural properties of cancrinite zeolite. XEDS-TEM analysis reveals a Si/Al ratio of 1.02 for cancrinite crystals formed from a reaction mixture with Si/Al=4.

Therefore, relatively low Si/Al ratio (e.g. 4, 2 and 1) within the synthesis gel leads to the formation of cancrinite with an ideal Si/Al ratio of 1.0. Also, with decreasing the Si/Al ratio, higher fraction of small cancrinite crystallites tends to crystallize with dimensions within 100 nm in length, as shown by the TEM images. The decrease in the average crystal size with decreasing Si/Al ratio results in an increase in textural properties.

References

(1) Kloprogge, J. T.; Komarneni, S.; Amonette, J. E. *Clays Clay Miner.* **1999**, *47*, 529.

(2) Fajnor, V. S.; Kuchta, L. *Chem. Papers*, **1988**, *42*, 339.

(3) Kloprogge, J. T.; Breukelaar, J.; Jansen, B. H.; Geus, J. W. *Clays Clay Miner.* **1993**, *41*, 103.

(4) Vogels, R. J. M. J.; Breukelaar, J.; Kloprogge, J. T. *Clays Clay Miner.* **1997**, *45*, 1.

(5) Prihod'ko, R.; Sychev, M.; Hensen, E. J. M.; Veen, J. A. R. V. *Stud. Surf. Sci. Catal.* **2002**, *142*, 271.

(6) Vogels, R. J. M. J.; Kerkhoffs, M. J. H. V.; Geus, J. W. *Stud. Surf. Sci. Catal.* **1995**, *91*, 1153.

(7) Xue, S.; Pinnavaia, T. J. *Micropor. Mesopor. Mater.* **2008**, *107*, 134.

(8) Strunz, H. *Mineralogische Tabellen* **1997**, 7.

(9) Buhl, J.-Ch.; Hackbarth, K.; Gesing, Th.M.; Fechtelkord, M.; Stief, F. *Micropor. Mesopor. Mater.* **1999**, *30*, 347.

(10) Weller, M. T.; Kenyon, N. J. *Micropor. Mesopor. Mater.***2003**, *59*, 185.

(11) Merlino, S.; Mellini, M.; Bonaccorsi, E.; Marco, P.; Pasero, M.; Leoni, L.; Orlandi, P. *Am. Mineral.* **1991**, *76*, 2003.

(12) Bonaccorsi, E.; Ventura, G. D.; Bellatreccia, F.; Merlino, S. *Micropor. Mesopor. Mater.* **2007**, *99*, 225.

(13) Buhl, J.-Ch.; Hermeler, G.; Hoffmann, W. *Catal. Today* **1991**, *8*, 415.

(14) Buhl, J.-Ch.; Fechtelkord, M.; Hackbarth, K. *React. Kinet. Catal. Lett.* **1998**, *65*, 33.

(15) Dann, S. E.; Armstrong, J. A. *Micropor. Mesopor. Mater.* **2000**, *41*, 89.

(16) Gerson, A. R.; Barnes, M. C.; Addai-Mensah, J. *Micropor. Mesopor. Mater.* **1999**, *31*, 287.

(17) Gerson, A. R.; Barnes, M. C.; Addai-Mensah, J. *Micropor. Mesopor. Mater.* **1999**, *31*, 303.

(18) Zheng, K.; Gerson, A. R. *J. Cryst. Growth* **1997**, *171*, 209.

(19) Zheng, K.; Gerson, A. R.; Addai-Mensah, J.; Smart, R. S. *J. Cryst. Growth* **1997**, *171*, 197.

(20) Navrotsky, A.; Liu, Q.; Xu, H. *Micropor. Mesopor. Mater.* **2005**, *87*, 146.

(21) Navrotsky, A.; Liu, Q.; Jove-Colon, C. F.; Bonhomme, F. *Micropor. Mesopor. Mater.***2007**, *98*, 227.

(22) Buhl, J.-C.; Stief, F.; Fechtelkord, M.; Gesing, T. M.; Taphorn, U.; Taake, C. *J. Alloy. Compd.* **2000**, *305*, 93.

CHAPTER 5

Influence of the Alkalinity and Temperature on the Synthesis of Cancrinite-Sodalite System

5.1 Introduction

Cancrinite and sodalite are very interesting zeolites because they have very low Si/Al ratio (Si/Al=1.0) and they're able to incorporate anions in their structure. Cancrinite (CAN) is found in nature with the composition $Na_6Ca[AlSiO_4]_6CO_3(H_2O)_2$, while sodalite (SOD) with the composition $Na_8[AlSiO_4]_6Cl_2$.[1] The cancrinite framework can be easily built from ABAB stacking of hexagonal arrays of 6-membered rings of SiO_4 and AlO_4 tetrahedra along the *c*-axis (see Figure 1.14).[2,3] Small 11-hedral cages (ε-cages) and a big 12-ring channel along the [001] direction are the results of this arrangement of sheets. On the other hand, stacking these layers in an ABCABC sequence leads to the cubic sodalite framework with its characteristic β-cage (Figure 1.14). In cancrinite, isomorphous positioning of aluminum in tetrahedral coordination results in negative charges on the framework counterbalanced by cations held within the cavities and channels. The big open channels host cation-anion pairs, while the ε-cages contain chains of alternating charge-balancing cations and water molecules.[4,5]

The structural and compositional similarities between the sodalite and cancrinite often results in the co-crystallization of both aluminosilicates. Therefore, the preparation of large amounts of pure-phase canrinite can be difficult due to the formation of disordered cancrinite and an intermediate phase between cancrinite and sodalite, and the co-crystallization of sodalite.[2,3,6-23] Buhl et al.[2,6,7] investigate the best conditions for the synthesis of sodium carbonate cancrinite as a single phase. Cancrinite was only shown to form as a pure phase at temperatures not below 200°C. The concentration of reactants and the alkalinity of the hydrothermal solution had a much lower influence on the phase formation. An intermediate phase with one-dimensional stacking disorder of the $(AlSiO_4)_n$ layers was obtained at lower reaction temperature of 80°C. Weller reported the effect of calcium on the hydrothermal synthesis of the cancrinite framework in the presence of carbonate at 150 and 220°C.[3] Ideal cancrinite was formed under calcium-free conditions at 220°C, whereas a disordered cancrinite/sodalite intergrown phase was observed at 150°C. The addition of calcium into the reaction mixture leads to its incorporation into the cancrinite structure. At high concentration of calcium a new phase ($NaCaSiO_3OH$) is formed. A phase transition sequence of amorphous phase–zeolite A– sodalite–cancrinite was reported by Barns and co-workers.[9,10] The pathway by which sodalite converts to cancrinite is the result of sodalite dissolution and subsequent cancrinite precipitation. Pure nitrate cancrinite was prepared by Navrotsky et al.[24-26] based on a simple synthetic route at 90°C, without the formation of intermediate phase or sodalite. This can be attributed to the difference in concentrations of the starting solutions and the fact that no crystalline precursors (e.g. kaolinite, zeolite

A) were used in their synthesis process, which were used by most of the reported synthesis.[2,3,6-10,15-17,19-22]

In the previous chapter, we reported a new phase mixture of saponite and cancrinite and investigated the influence of $Mg(NO_3)_2$ and NaOH concentrations on the synthesis of this mixed phase. Pure cancrinite can be prepared under Mg-free conditions, because Mg cations are essential for saponite formation, but not for cancrinite formation. Also, various Si/Al ratios in the reaction mixture affected the chemical composition and textural property of the resulting cancrinite.

In the present chapter, we investigate the effect of alkalinity and reaction temperature on the synthesis of nitrate cancrinite and nitrate sodalite. Ideal nitrate cancrinite is formed in a wide range of reaction parameters, e.g. NaOH concentration, temperature, and duration. The concentration of NaOH influences the product distribution at a reaction temperature of 90°C in the following way: high OH^- concentrations lead preferentially to the formation of single-phase CAN, while low concentrations produce a CAN-SOD mixture. Also, pure cancrinite could be synthesized if the aging temperature is not below 40°C. However, a cancrinite-sodalite mixture with sodalite as the major phase is formed at room temperature.

5.2 Experimental

5.2.1 Materials

Sodium silicate containing 27 wt.% SiO_2 and 14 wt.% NaOH and $Al(NO_3)\cdot 9H_2O$ were purchased from Aldrich Chemical Co.. All other chemicals were purchased from Aldrich Chemical Co. and used without further purification.

5.2.2 Synthesis of Nitrate Cancrinite

8.55 g of sodium silicate solution (27 wt.% silica, 14 wt.% NaOH) (0.03850 mol silica) and 14.44 g (0.03850 mol) of $Al(NO_3)_3\cdot 9H_2O$ were first added to 87 ml of deionized water in a sealed polypropylene bottle. A cloudy gel-like solution was obtained after complete mixing. Then, NaOH as the source of base ranging between 28.8 g (0.72 mol) and 115.2 g (2.88 mol) was introduced and the bottle was vigorously shaken to ensure homogeneous mixing. The molar ratio for sodium silicate, aluminum nitrate, sodium hydroxide (not including NaOH in the sodium silicate solution) and water is 1:1:18.8-75:125. The resulting gels were placed in oven heated at 40°C to 90°C in tightly stoppered polypropylene bottles. Samples were taken from the oven at pre-determined time periods ranging from 1 day to 7 days. All products were washed using deionized water via centrifugation 3 times. All samples were dried overnight in oven at 80°C under nitrogen gas flow.

5.2.3 Synthesis of Phase Mixtures of Nitrate Cancrinite and Nitrate Sodalite

Synthesis steps are similar to those used for the synthesis of nitrate cancrinite except that the molar ratio for sodium silicate, aluminum nitrate, sodium hydroxide and water in the initial solutions is 1:1:4.69-9.38:125.

5.2.4 Characterization

X-ray diffraction (XRD) patterns were obtained on a Rigaku rotaflex 200B diffractometer equipped with Cu Kα X-ray radiation and a curved crystal graphite monochromator, operating at 45 kV and 100 mA. Powder samples were pressed onto a glass X-ray sample holder.

N_2 adsorption-desorption isotherms were recorded at –196°C on a Micrometritcs Tristar 3000 sorptometer. Prior to analysis samples were outgassed at 150°C and 10^{-6} Torr for a minimum of 12 h. BET surface areas were calculated from the linear part of the BET plot and BJH pore sizes were obtained from adsorption isotherms.

Transmission electron microscopy (TEM) images were obtained on a JEOL 2200FS field emission microscope with a ZrO/W Schottky electron gun and an accelerating voltage of 200 kV. The powdered samples were sonified in ethanol, and dripped onto 300 mesh copper grids.

^{29}Si MAS NMR spectra were obtained at 79 MHz on a Varian VXR-400S solid-state NMR spectrometer equipped with a magic angle-spinning probe. Sample was spun at 4 kHz for each measurement. The pulse delay for ^{29}Si MAS NMR was 400 s, and chemical shifts were referenced to talc. FTIR spectra of samples dispersed in KBr disks were recorded at ambient temperature on a Mattson Galaxy 3000 FTIR spectrometer over the range 400-4000 cm^{-1}.

5.3 Results and Discussion

To investigate the effect of the alkalinity of the starting solutions on cancrinite phase formation, we selected five different NaOH concentrations. The

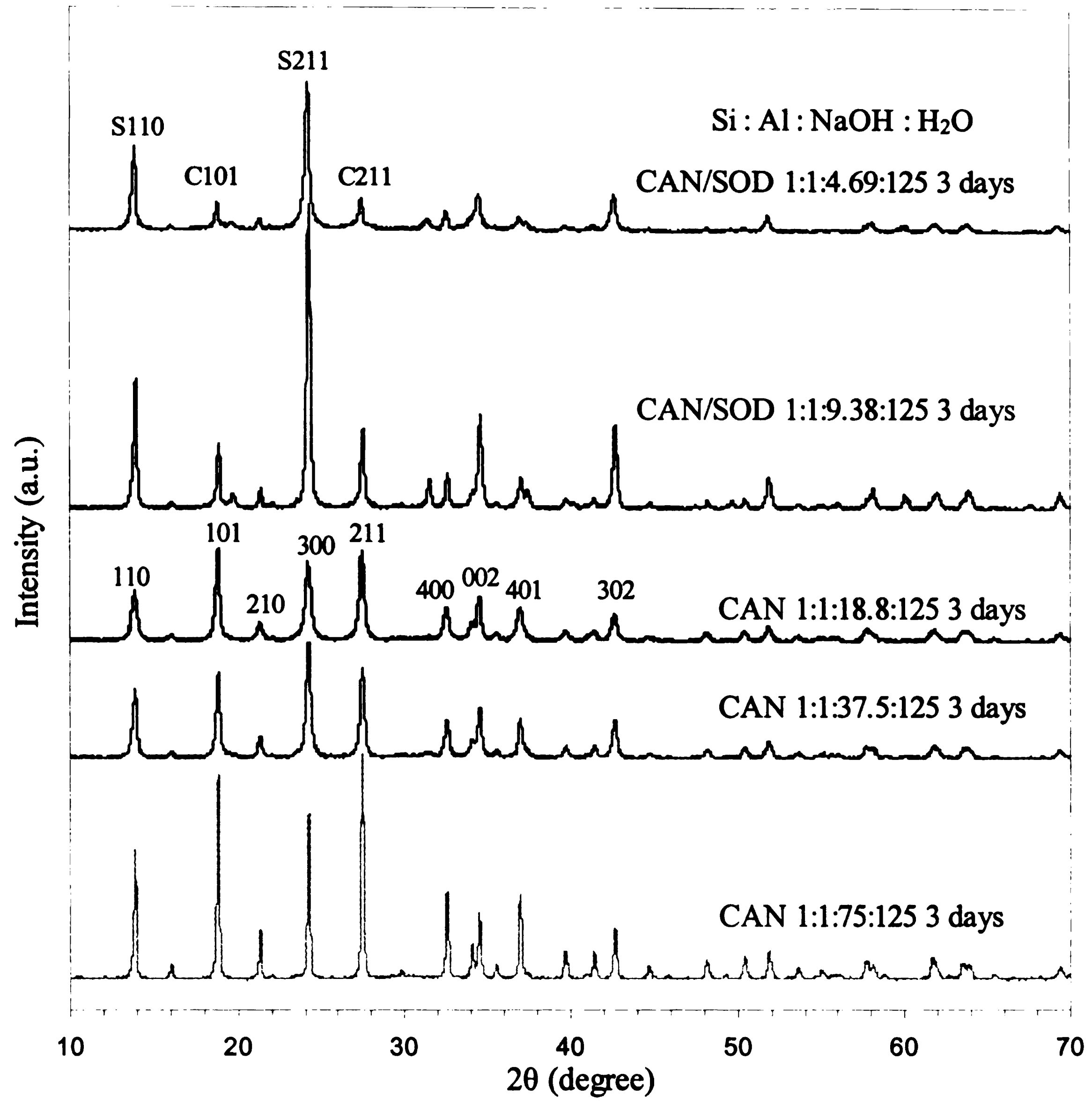

Figure 5.1 XRD patterns of reaction products as a result of varying alkalinity in the starting solutions after a reaction time of 3 days at 90°C. The ratios represent the Si:Al:NaOH:H_2O stoichiometry of the reaction system. (S=sodalite, C=cancrinite)

Figure 5.2 TEM images of (a), (b) and (c) ideal cancrinite crystals formed at 3 different alkalinities of x=75, 37.5 and 18.8, respectively; (d) cancrinite in CAN/SOD phase mixture formed at x=9.38; (e) and (f) rod-like cancrinite and cotton-ball like sodalite in CAN/SOD phase mixture formed at x=4.69. All the samples were prepared at 90°C after a reaction time of 3 days.

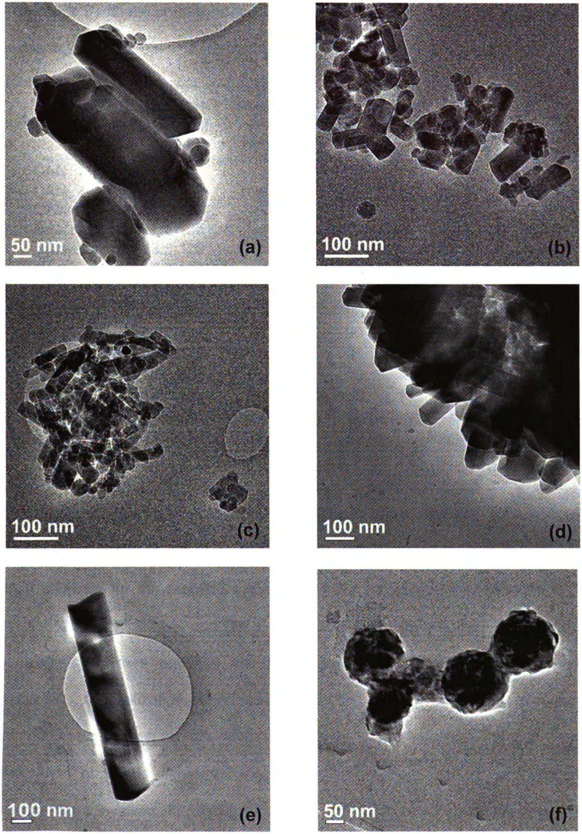
50 nm
(a)
100 nm
(b)
100 nm
(c)
100 nm
(d)
100 nm
(e)
50 nm
(f)

Table 5.1 Synthetic conditions together with the textural properties of reaction products

Products	$Si:Al:NaOH:H_2O$ in the starting materials	Reaction time (days)	Temperature (°C)	BET surface area (m^2/g)	Total pore volume (cm^3/g)
CAN	1:1:75:125	3	90	7.9	0.056
CAN	1:1:37.5:125	1	90	68.9	0.55
CAN	1:1:37.5:125	3	90	41.9	0.41
CAN	1:1:37.5:125	7	90	48.6	0.38
CAN	1:1:18.8:125	1	90	97.6	0.66
CAN	1:1:18.8:125	3	90	74.8	0.49
CAN	1:1:18.8:125	7	90	59.6	0.35
CAN/SOD	1:1:9.38:125	1	90	24.0	0.13
CAN/SOD	1:1:9.38:125	3	90	22.6	0.15
CAN/SOD	1:1:4.69:125	1	90	71.4	0.19
CAN/SOD	1:1:4.69:125	3	90	41.0	0.20
CAN	1:1:18.8:125	3	60	109.5	0.70
CAN	1:1:18.8:125	3	40	125.7	0.61
SOD/CAN	1:1:18.8:125	3	25	208.6	0.29

X-ray powder patterns of the products after 3 days reaction at 90°C are summarized in Figure 5.1. Pure-phase nitrate cancrinite was formed at relatively high alkalinity for the reaction systems with the compositions $Si:Al:NaOH:H_2O$ =1:1:x:125, x=75, 37.5 and 18.8. The diffraction patterns of these three crystalline powders matched the data reported by Buhl[15] for ideal nitrate cancrinite. Crystallization of nitrate cancrinite was almost completed after 1 day at 90°C, as verified by the X-ray diffraction pattern (not shown here). The formation of nitrate cancrinite was rather fast considering the low reaction temperature involved. TEM images in Figure 5.2 (parts a, b and c) illustrate the differences in morphology and crystallite size for cancrinites formed at three different alkalinities corresponding to x=75, 37.5 and 18.8. At x=75, cancrinite grows into rather large rod-like crystals with several hundred nm in length. This product has a very low BET surface area of 7.9 m^2/g (Table 5.1), which is associated with the large crystallite size. When the alkalinity was reduced to half and one fourth, mostly rod-like cancrinite crystals exhibit uniform size distribution within 100 nm in length. Additionally, crystals formed at x=37.5 seem to grow wider than those at x=18.8, and both of their BET surface areas increase a lot in comparison to the large crystals prepared at x=75. With longer reaction time, cancrinite crystals tends to nucleate and grow larger, as indicated by the decrease in the surface area with increasing reaction period (see Table 5.1).

XRD patterns show that upon decreasing the NaOH concentration further, some new phases appear. The precipitation of a phase mixture of cancrinite and sodalite takes place at a Si:Al:NaOH:H_2O stoichiometry of 1:1:9.38:125 and 1:1:4.69:125. The reflection peaks of the CAN/SOD phase mixtures indicate the typical cancrinite reflections in the powder pattern, but with much weaker intensities for the 101 and 211 peaks. Pure sodalite and cancrinite have very similar XRD patterns, and the two can be distinguished by the presence of the cancrinite 101 and 211 diffraction peaks. Barnes and co-workers developed a simple methodology for determining the cancrinite proportion of a sodalite and cancrinite phase mixture using powder X-ray diffraction.[10] They used overlapping C110+S110 and C300+S211 (where C=cancrinite and S=sodalite) diffraction peaks as the reference peaks and the C101 and C211 peaks as variables because they're unique to cancrinite. The relative peak intensities for the C101 and C211 diffraction peaks, when normalized against the C300+S211 peak, were each found to increase linearly with increasing CAN concentration. Here, Table 5.2 shows an increase in the relative peak height of the characteristic cancrinite 101 and 211 diffraction peaks with increasing reaction time, which can be attributed to an increased CAN population in the phase mixture. This result suggests that sodalite-to-cancrinite phase transformation can occur in the reaction system.

Table 5.2 Relative intensities of four diffraction peaks for sodalite and cancrinite phase mixtures

Products	$Si:Al:NaOH:H_2O$ =1:1:x:125	Aging time (days)	Relative diffraction peak intensity			
			C110+ S110	C101	C300+ S211	C211
CAN/SOD	x=9.38	1	41.6	14.9	100	16.5
		3	42.4	20.2	100	25.5
CAN/SOD	x=4.69	1	62.7	4.1	100	11.5
		3	57.5	16.1	100	20.0

A TEM image of aggregated cancrinite in the CAN/SOD phase mixture (Figure 5.2 d) shows that it retains the rod-like morphology, but forms much larger crystallites in comparison to cancrinite formed at x=37.5 and 18.8. In addition, the *hkl* reflections for ideal cancrinite at x=37.5 and 18.8 are broader than those for CAN/SOD at x=9.38, indicative of a much smaller crystalline dimension and in agreement with the TEM observation. In the case of CAN/SOD at x=4.69, sodalite with "cotton-ball" like morphology was also observed in addition to the rod-like cancrinite morphology (Figure 5.2 e, f).

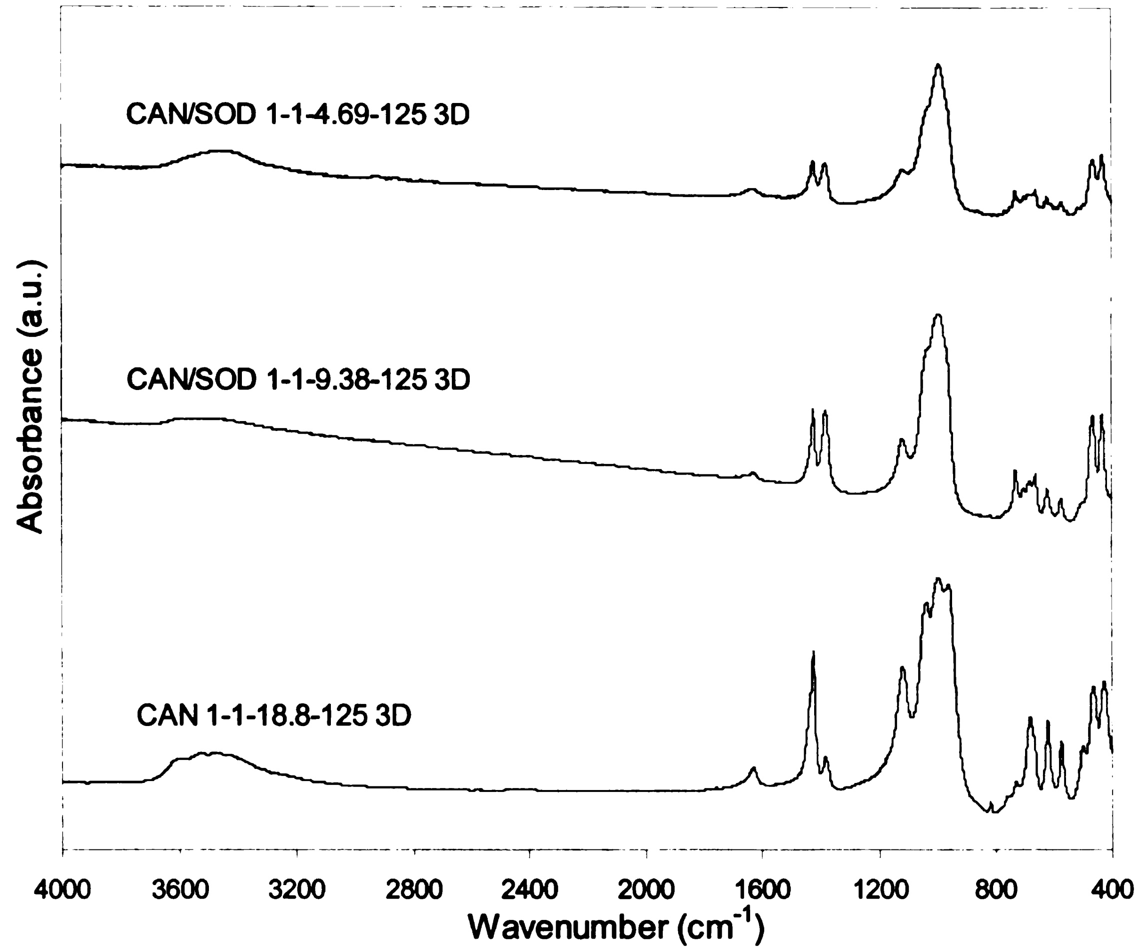

Figure 5.3 FTIR spectra of selected products formed at varying alkalinity in the starting solutions after 3 days reaction at 90°C. The ratios represent the Si:Al:NaOH:H_2O stoichiometry in the reaction system.

A further indication of a cancrinite-sodalite mixture formation is provided by IR spectroscopic results (Figure 5.3). The broad band at 3100-3600 cm^{-1} and the bending mode at 1630 cm^{-1} can be assigned to water molecules. For the ideal nitrate cancrinite prepared at x=18.8 and a reaction time of 3 days, the absorbance for the asymmetric stretch $\nu_{Al\text{-}O}$ for the Si-O-Al framework is split into four peaks at 1120, 1039, 998 and 963 cm^{-1}, in accordance with the reported IR assignments for cancrinite.[10,15,20] In the phase mixture of cancrinite and sodalite formed at x=9.38 and 4.69, absorptions at 1120, 1040 (shoulder) and 996 cm^{-1} can be resolved. Pure sodalite should exhibit a single peak at 996 cm^{-1} for the asymmetric framework stretch. The region of 400-800 cm^{-1} is known as "fingerprint" region. The characteristic fingerprint peaks for pure cancrinite occur at 575, 622, 683, and 770 cm^{-1} as shown in Figure 5.3. The absorptions at 683 and 770 cm^{-1} correspond to the symmetric Al-O stretch for the Si-O-Al framework and the bands at 575 and 622 cm^{-1} arise from the vibration of the parallel 4- or 6-membered double rings of cancrinite. For sodalite, fingerprint peaks occur at 665, 704 and 731 cm^{-1}. For CAN/SOD phase mixtures made at x=9.38 and 4.69, characteristic fingerprint peaks for both cancrinite and sodalite can be resolved in the region of 500-800 cm^{-1}. In addition to the weak bending mode near 820 cm^{-1}, the presence of nitrate groups inside the cancrinite channels can be better detected by the ν_{as} vibration at 1425 cm^{-1}. The absorption band at 1383 cm^{-1} could be attributed to small amounts of precipitated sodium nitrate on the outer surface of the crystals. Intercalated nitrate within the sodalite cages also exhibits a band at 1383 cm^{-1}.[19,27] Thus, the intensity of this peak increases relative to the peak at 1425 cm^{-1} in the phase mixture.

The ^{29}Si MAS NMR spectrum of pure cancrinite (Figure 5.4) formed from a reaction composition of Si:Al:NaOH:H_2O=1:1:18.8:125 exhibits a single sharp signal at -87.3 ppm, in agreement with the alternating ordering of tetrahedrally coordinated Si, Al atoms in the CAN framework for a Si/Al ratio of 1.0. Some studies[10,19] have demonstrated that ^{29}Si MAS NMR is not suitable for determining whether an aluminosilicate sample is sodalite or cancrinite because both phases have the same or very similar chemical shifts. Therefore, ^{29}Si MAS NMR is not helpful for distinguishing cancrinite from a cancrinite-sodalite phase mixture.

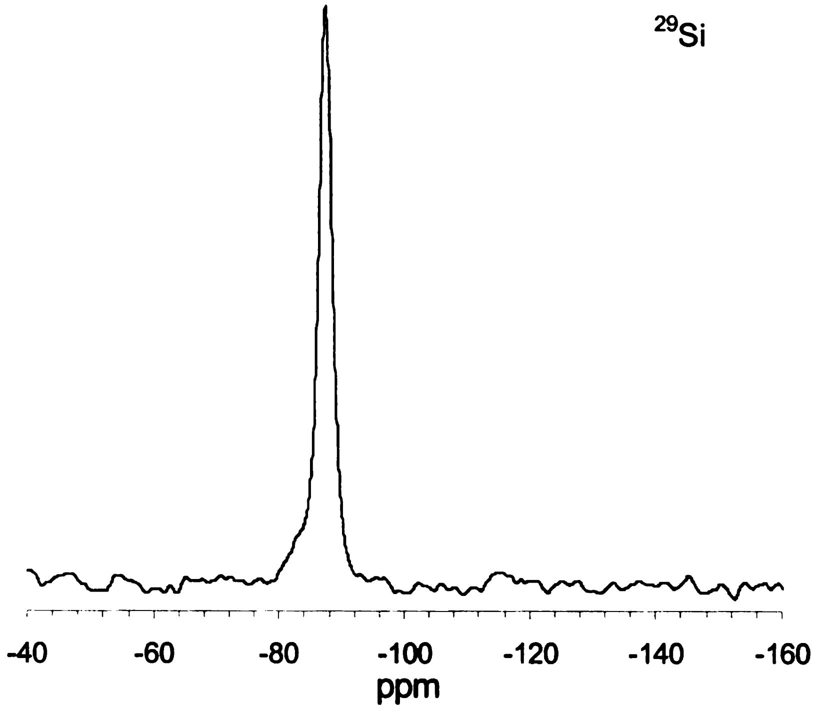

Figure 5.4 ^{29}Si MAS NMR spectrum of pure cancrinite precipitated from the educts with composition of Si:Al:NaOH:H_2O=1:1:18.8:125 at 90°C after 3 days.

N_2 adsorption-desorption isotherms for products synthesized at different alkalinities are presented in Figure 5.5. A fairly narrow hysteresis loop for pure cancrinite formed at x=37.5 and 18.8 implies a mesoporous structure for these products. However, it should be noted that the pore sizes shown in Figure 5.5 (a) are the result of secondary pores between aggregated cancrinite crystals rather than the pores in the cancrinite framework structure. The micropores (5.9×5.9 Å) of cancrinite are blocked by nitrate anions, thus preventing the N_2 molecules from

Figure 5.5 N_2 adsorption-desorption isotherms of (a) pure cancrinite products and (b) CAN/SOD phase mixtures, formed at different alkalinities after 1 day or 3 days of reaction period. The insert provides BJH pore size distributions determined from the adsorption branches of the N_2 isotherms of selected products.

(a)

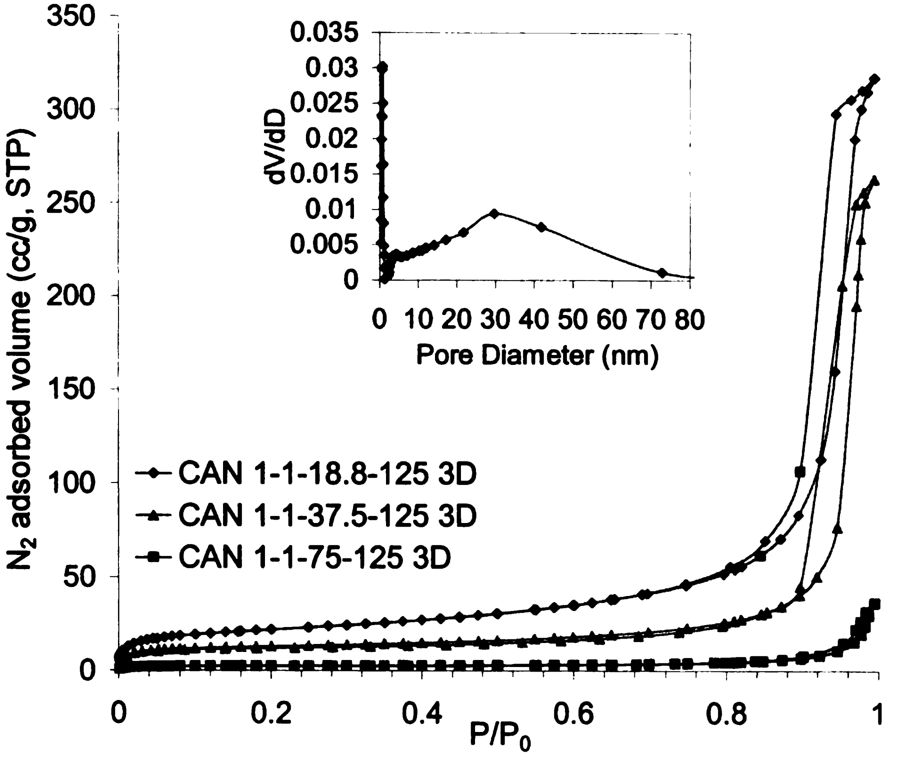

N₂ adsorbed volume (cc/g, STP)
350
300
250
200
150
100
50
0
0
0.2
0.4
0.6
0.8
1
P/P₀
CAN 1-1-18.8-125 3D
CAN 1-1-37.5-125 3D
CAN 1-1-75-125 3D
dV/dD
0.035
0.03
0.025
0.02
0.015
0.01
0.005
0
0 10 20 30 40 50 60 70 80
Pore Diameter (nm)

(b)

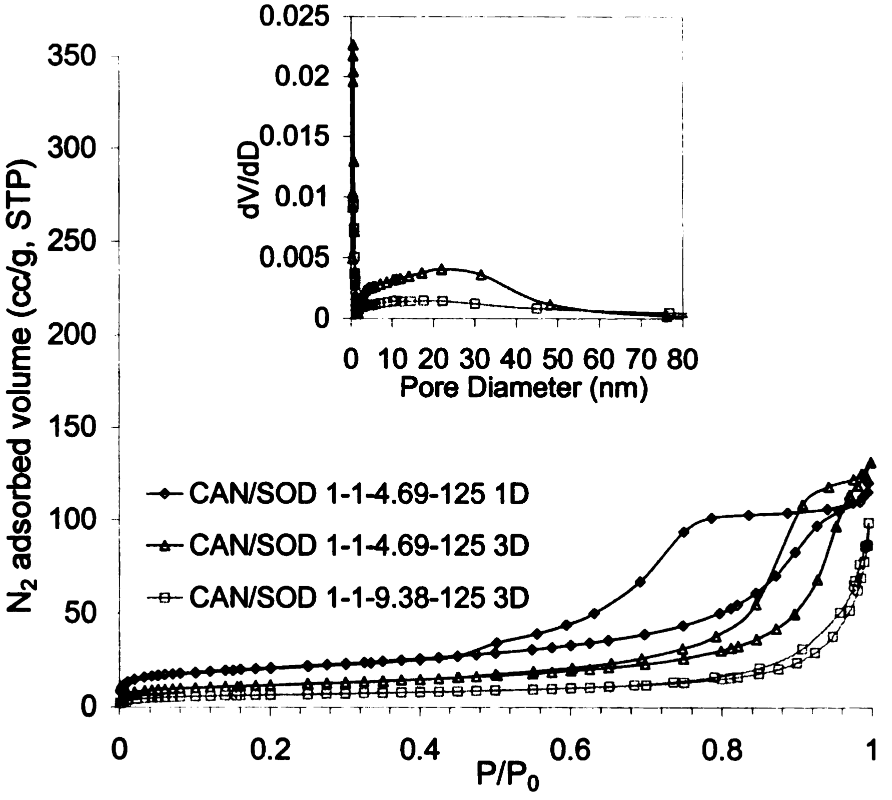

N₂ adsorbed volume (cc/g, STP)
350
300
250
200
150
100
50
0
0
0.2
0.4
0.6
0.8
1
P/P₀
CAN/SOD 1-1-4.69-125 1D
CAN/SOD 1-1-4.69-125 3D
CAN/SOD 1-1-9.38-125 3D
dV/dD
0.025
0.02
0.015
0.01
0.005
0
0 10 20 30 40 50 60 70 80
Pore Diameter (nm)

accessing the interior of the pores. This explains the very limited N_2 uptake in the adsorption branch at low relative pressure ($P/P_0 < 0.1$) for cancrinite. With regard to the SOD/CAN phase mixture prepared at x=4.69 after 1 day, the nitrogen shows a broad hysteresis loop and the pore filling step begins at about 0.45 P/P_0. Moreover, the hysteresis loop shape of this cancrinite-sodalite mixture transforms to that of the pure cancrinite when the reaction period was increased to 3 days, suggesting that sodalite-to-cancrinite phase conversion may occur.

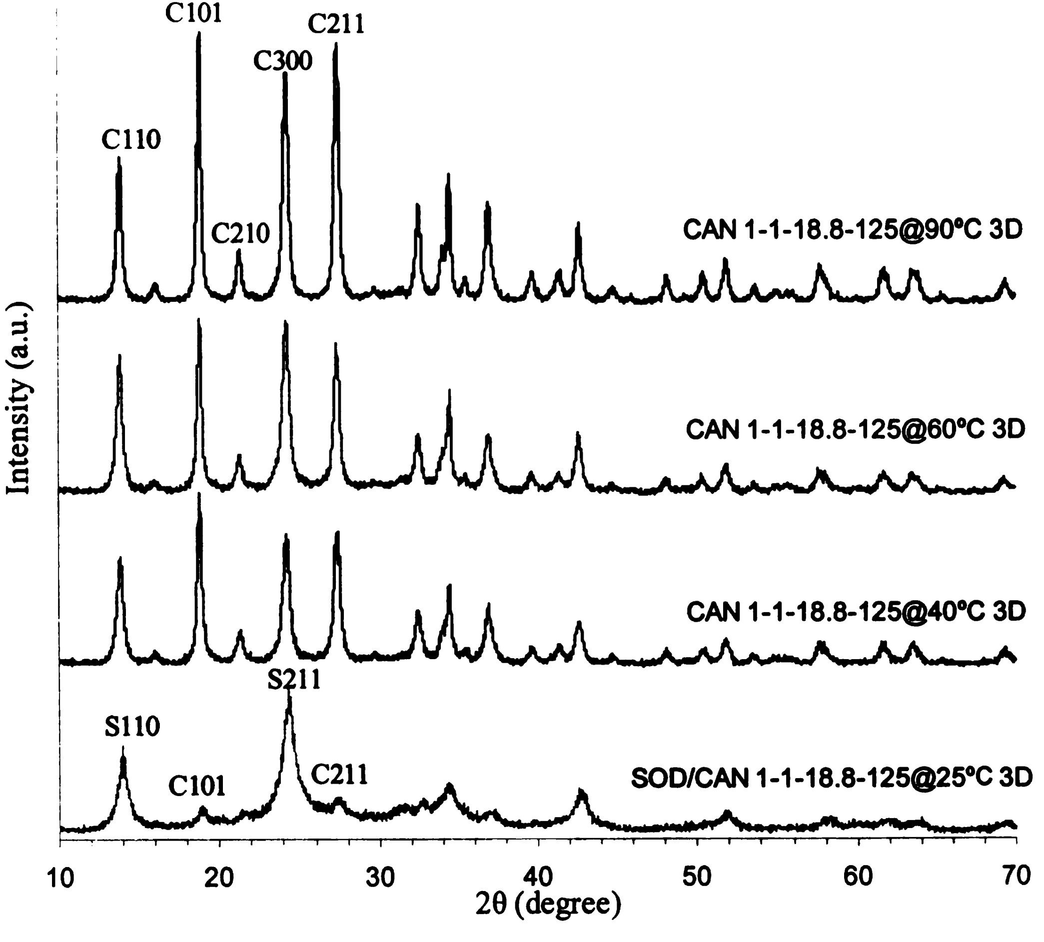

Figure 5.6 XRD patterns of products formed at different reaction temperatures. (S=sodalite, C=cancrinite)

We also studied the influence of reaction temperature on the synthesis of cancrinite and sodalite. The wide angle *hkl* reflections of reaction products formed at 90, 60, 40 and 25°C are provided in Figure 5.6. All of the products were formed from the same initial reaction composition of Si:Al:NaOH:H_2O at 1:1:18.8:125 after 3-day period. As illustrated by XRD patterns, pure cancrinite can be synthesized at temperatures as low as 40°C. In addition, the lower temperatures may be in favor of the formation of smaller cancrinite crystallites, as indicated by the broader reflection peaks for CAN@60°C and 40°C in comparison to CAN@90°C. Sodalite crystals emerge together with cancrinite at room temperature, but the cancrinite is a minor co-product, as indicated by the very weak intensities of the CAN 101 and 211 reflections. TEM images in Figure 5.7 clearly show the cotton-ball like aggregation of nanometric sodalite crystals with dimension less than 500 nm. Actually, no cancrinite crystals with a characteristic rod-like morphology are observed during the TEM investigation due to the minor amount.

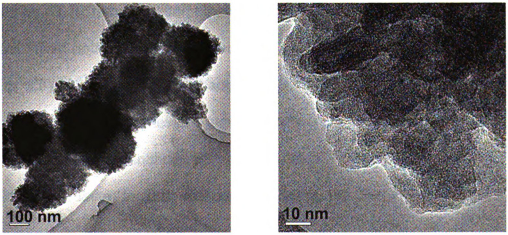

Figure 5.7 TEM images of sodalite crystals prepared at 25°C after 3 days at high and low magnifications.

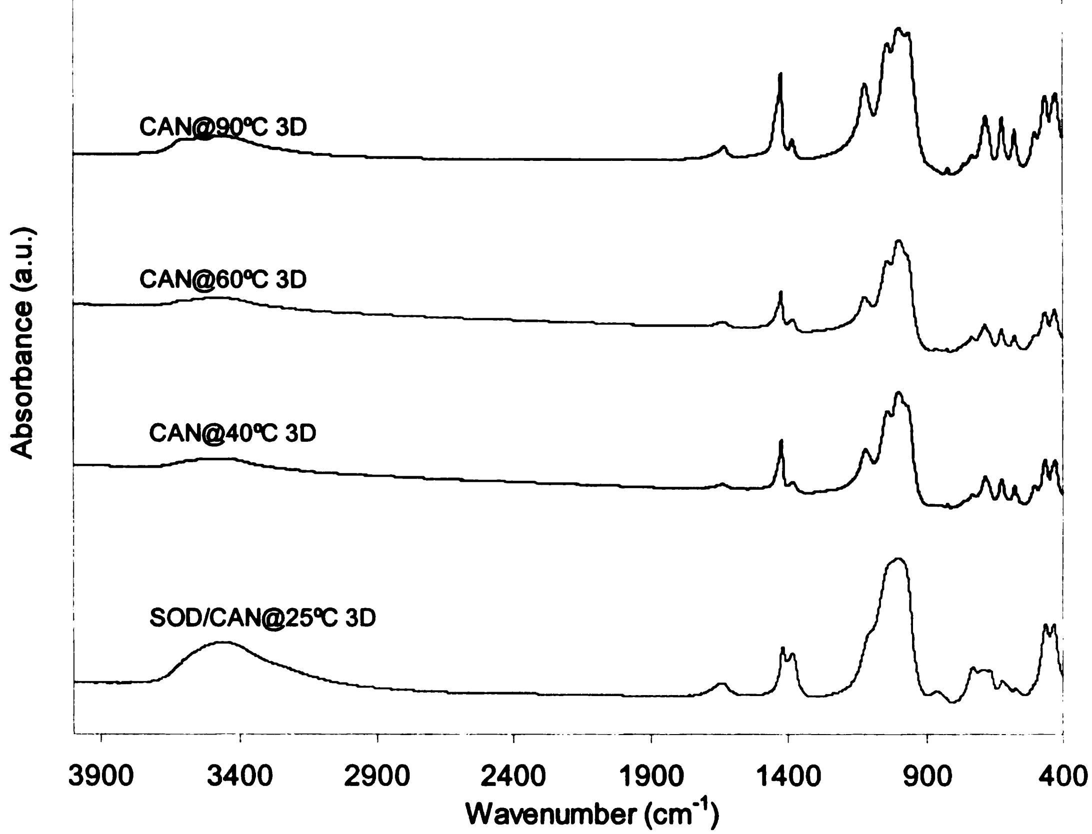

Figure 5.8 FTIR spectra of products as a result of changing reaction temperature.

Pure cancrinite framework structures formed at 40°C or above also can be verified by FT-IR results. A combination of fingerprint peaks in the region of 500-800 cm^{-1} from both sodalite and cancrinite can be resolved for SOD/CAN@25°C (Figure 5.8). Also, the strong absorption band at ~1000 cm^{-1} attributed to v_{as} vibration for sodalite framework together with the shoulder peak at 1120 cm^{-1} from v_{as} vibration for cancrinite framework further suggests that the major phase should be sodalite in this mixture. According to N_2 adsorption-desorption measurements, this SOD/CAN phase mixture exhibits a large BET surface area of 209 m^2/g, a uniform BJH adsorption pore size distribution centered at 3.0 nm and a total pore volume of 0.29 cm^3/g. The nitrogen isotherm of SOD/CAN is easily distinguished from those of pure CAN, as shown in Figure 5.9.

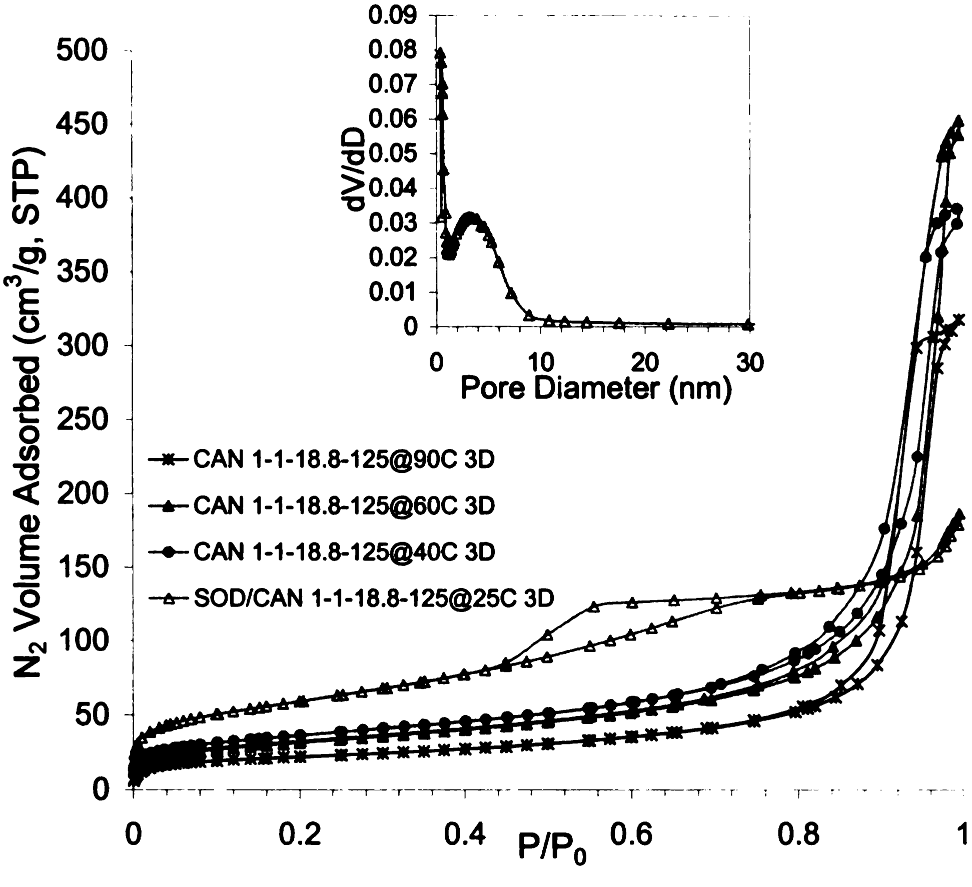

Figure 5.9 N$_2$ adsorption-desorption isotherms of samples formed as a function of reaction temperature after 3 days reaction time. The insert provides the BJH pore-size distribution determined from the adsorption branch of the N$_2$ isotherm of SOD/CAN@25°C phase mixture.

5.4 Summary

Nitrate cancrinite and sodalite have been synthesized based on a simple batch reaction method using sodium silicate and aluminum nitrate as silica and alumina sources. The reaction conditions, e.g. amount of base, reaction temperature and reaction time, were varied to determine their influence on the zeolite phase formation. Single-phase nitrate cancrinite can be formed in a wide range of synthesis parameters. At high concentrations of NaOH corresponding to OH^-/Si ratios of 18.8 to 75, cancrinite emerged at 90°C after 24 h. The morphology and crystallite size of the resulting products are very sensitive to the alkalinity, according to the BET surface area and TEM measurements. At low concentrations of NaOH corresponding to OH^-/Si ratios of 4.69 to 9.38, a cancrinite-sodalite mixture was obtained, as confirmed by the powder X-ray diffraction and FTIR spectroscopy characterizations. Moreover, a phase transformation from sodalite to cancrinite occurred in this mixture with increasing reaction time. This observation suggests that sodalite is the kinetically favored phase under reaction conditions, but cancrinite predominates as the thermodynamically stable phase. With respect to the dependence on the temperature, pure cancrinite was found over the range 40-90°C, whereas a reaction temperature below 40°C results in the co-crystallization of sodalite as the major phase.

References

(1) Strunz, H. *Mineralogische Tabellen* **1997**, 7.

(2) Buhl, J.-Ch.; Hackbarth, K.; Gesing, Th.M.; Fechtelkord, M.; Stief, F. *Micropor. Mesopor. Mater.* **1999**, *30*, 347.

(3) Weller, M. T.; Kenyon, N. J. *Micropor. Mesopor. Mater.* **2003**, *59*, 185.

(4) Merlino, S.; Mellini, M.; Bonaccorsi, E.; Marco, P.; Pasero, M.; Leoni, L.; Orlandi, P. *Am. Mineral.* **1991**, *76*, 2003.

(5) Bonaccorsi, E.; Ventura, G. D.; Bellatreccia, F.; Merlino, S. *Micropor. Mesopor. Mater.* **2007**, *99*, 225.

(6) Buhl, J.-Ch.; Hermeler, G.; Hoffmann, W. *Catal. Today* **1991**, *8*, 415.

(7) Buhl, J.-Ch.; Fechtelkord, M.; Hackbarth, K. *React. Kinet. Catal. Lett.* **1998**, *65*, 33.

(8) Dann, S. E.; Armstrong, J. A. *Micropor. Mesopor. Mater.* **2000**, *41*, 89.

(9) Gerson, A. R.; Barnes, M. C.; Addai-Mensah, J. *Micropor. Mesopor. Mater.* **1999**, *31*, 287.

(10) Gerson, A. R.; Barnes, M. C.; Addai-Mensah, J. *Micropor. Mesopor. Mater.* **1999**, *31*, 303.

(11) Zheng, K.; Gerson, A. R. *J. Cryst. Growth* **1997**, *171*, 209.

(12) Zheng, K.; Gerson, A. R.; Addai-Mensah, J.; Smart, R. S. *J. Cryst. Growth* **1997**, *171*, 197.

(13) Buhl, J.-C.; Fechtelkord, M.; Posnatzki, B. *Chem. Mater.* **2001**, *13*, 1967.

(14) Burton, A.; Feuerstein, M.; Lobo, R. F.; Chan, J. C. C. *Micropor. Mesopor. Mater.* **1999**, *30*, 293.

(15) Buhl, J.-C.; Stief, F.; Fechtelkord, M.; Gesing, T. M.; Taphorn, U.; Taake, C. *J. Alloys. Compd.* **2000**, *305*, 93.

(16) Ocanto, F.; Alvarez, R.; Lieb, A.; Linares, C. F. *Micropor. Mesopor. Mater.* **2008**, *116*, 318.

(17) Ocanto, F.; Figueredo, E.; Brikgi, M.; Linares, C. F. *Mater. Lett.* **2009**, *63*, 11.

(18) Ngamcharussrivichai, C.; Chatratananon, C.; Nuntang, S. Prasassarakich, P. *Fuel* **2008**, *87*, 2347.

(19) Buhl, J.-C.; Löns, J. *J. Alloys. Compd.* **1996**, *235*, 41.

(20) Zhao, H.; Deng, Y.; Harsh J.; Flury, M.; Boyle, J. *Clays Clay Miner.* **2004**, *52*, 1.

(21) Buhl. J.-C.; Hackbarth, K.; Fechtelkord, M. *React. Kinet. Catal. Lett.* **1998**, *65*, 33.

(22) Buhl, J.-C.; Taake, C.; Stief, F.; Fechtelkord, M. *React. Kinet. Catal. Lett.* **2000**, *69*, 15.

(23) Buhl. J.-C.; Mundus, C.; Mueller-Warmuth, W. *Eur. J. Mineral.* **1996**, *8*, 231.

(24) Navrotsky, A.; Liu, Q.; Xu, H. *Micropor. Mesopor. Mater.* **2005**, *87*, 146.

(25) Navrotsky, A.; Liu, Q.; Jove-Colon, C. F.; Bonhomme, F. *Micropor. Mesopor. Mater.***2007**, *98*, 227.

(26) Navrotsky, A.; Liu, Q. *Geochim. Cosmochim. Acta* **2007**, *71*, 2072.

(27) Buhl, J.-C. *Thermochim. Acta* **1991**, *189*, 75.

CHAPTER 6

Epoxy-Zeolite Composites with Enhanced Tensile Properties

6.1 Introduction

The chemical stability, excellent adhesion properties, and optical transparency of thermoset epoxy polymers make them suitable for a variety of applications, such as coatings, adhesives and electronic insulators. So far, most of the epoxy-based composites reported are reinforced by layered silicate clay nanoparticles[1-8], mesostructured silicas[9-13] and carbon nanotubes (CNTs)[14-18] in order to improve mechanical, thermal, and barrier properties. Only a few studies have been reported on zeolite-epoxy composites,[19-22] wherein the focus was on the effect of natural zeolite particles on the curing kinetics and mechanical properties of the epoxy system. With increasing zeolite content, tensile strength decreased dramatically, while Young's modulus increased, which is the result typical of conventional composites.[19]

In Chapter 5, we described the low-temperature synthesis of nitrate cancrinite (denoted as CAN) and nitrate sodalite (denoted as SOD) zeolites. In the present study, we investigate the use of CAN and SOD zeolites as reinforcement agents for thermoset epoxy polymer, particularly for a glassy epoxy system. The large one-dimensional 12-ring channel (5.9 Å×5.9 Å) and the small particle size (<100 nm) of rod-like cancrinite, and the high surface area

(~200 m^2/g) and a large average BJH pore size (~3.0 nm) of cotton-ball like sodalite are shown to substantially improve the tensile properties of the polymer.

Though a few studies have been reported concerning applications of cancrinite or cancrinite-type zeolites,[23-28] including as antacid,[24-26] heavy-metal trapping agents,[27] and cholesterol-controlling drug,[28] no efforts have been made on the polymer reinforcement application. The composites formed from synthetic nitrate cancrinite and sodalite represent the first example wherein the modulus, strength and toughness of epoxy-zeolite composites all are improved.

6.2 Experimental

6.2.1 Materials

Sodium silicate containing 27 wt.% SiO_2 and 14 wt.% NaOH and $Al(NO_3)\cdot 9H_2O$ were purchased from Aldrich Chemical Co.. $Mg(NO_3)_2\cdot 6H_2O$ was purchased from Columbus Chemical Industries, Inc.. The epoxide resin used to form glassy epoxy matrices was a diglycidyl ether of bisphenol A (DGEBA), more specifically, EPON 826 with an epoxy equivalent weight of ~182 g/equivalent. The curing agent was a polyoxypropylene diamine of the type $NH_2CH(CH_3)CH_2[OCH_2CH(CH_3)]_xNH_2$ ($x = 2.6$), which was provided by Huntsman Chemicals under the tradename Jeffamine D230. All other chemicals were purchased from Aldrich Chemical Co. and used without further purification.

6.2.2 Cancrinite and Sodalite Synthesis

In a typical synthesis, 8.55 g of sodium silicate solution (27 wt.% silica, 14 wt.% NaOH) (0.03850 mol silica) and 14.44 g (0.03850 mol) of $Al(NO_3)_3\cdot 9H_2O$

were first added to 87 ml of deionized water in a sealed polypropylene bottle. A cloudy gel-like mixture was obtained after complete mixing. Then, 28.8 g (0.72 mol) or 57.6 g (1.44 mol) of NaOH was introduced and the bottle was vigorously shaken to ensure homogeneous mixing. The molar ratio for sodium silicate, aluminum nitrate, sodium hydroxide (not including NaOH in sodium silicate solution) and water is 1:1:18.8/37.5:125. The resulting gels were heated in oven at 90°C or were allowed to age at room temperature in tightly stoppered polypropylene bottles for 3 days. All products were washed using deionized water via centrifugation 3 times. All samples were dried overnight in oven at 80°C under nitrogen gas flow.

6.2.3 Preparation of Epoxy-Zeolite Composites

A predetermined amount of cancrinite or sodalite was added to the epoxy resin and mixed at 50°C for 10 min. The amount of Jeffamine D230 curing agent needed to achieve an overall NH: epoxide stoichiometry of 1:1 was then added and the mixture was stirred with a stir bar at room temperature for 15 min, outgassed under vacuum for 20 min at room temperature, and transferred to a silicone mold. The composites were partially cured at 75°C for 3 h and then fully cured at 125°C for 3 h under N_2 flow.

6.2.4 Characterization

X-ray diffraction (XRD) patterns were obtained on a Rigaku rotaflex 200B diffractometer equipped with Cu Kα X-ray radiation and a curved crystal graphite monochromator, operating at 45 kV and 100 mA. Rectangular flat specimens of cross-linked composites were mounted onto an aluminum holder for XRD examination. N_2 adsorption-desorption isotherms were recorded at –196°C on a Micrometritcs Tristar 3000 sorptometer. Prior to analysis samples were outgassed at 150°C and 10^{-6} Torr for a minimum of 12 h. BET surface areas were calculated from the linear part of the BET plot and BJH pore size distribution were obtained from adsorption isotherms.

Tensile properties of dog-bone shaped specimens were tested according to ASTM procedure D3039 using an SFM-20 United Testing System equipped with a laser extensometer. The measurements were conducted at room temperature with a crosshead speed of 0.5 mm/min for glassy specimens. The reported tensile values are the averages for 4-5 specimens with dog-bone shapes.

6.3 Results and Discussion

Detailed characterization of nitrate cancrinite and nitrate sodalite is described in Chapter 5. The synthetic conditions together with the textural properties of the selected zeolites used for reinforcements of glassy epoxy polymers are summarized in Table 6.1. Note that SOD-18.8-25°C is actually a mixed SOD-CAN phase with minor amount of nitrate cancrinite. X-ray powder patterns and N_2 adsorption-desorption isotherms of selected zeolites are provided in Figure 6.1 and Figure 6.2, respectively.

Table 6.1 Textural properties of synthetic zeolites

Sodium aluminosilicate[a]	$Si:Al:NaOH:H_2O$ = 1:1:x:125 in the starting solutions	BET surface area (m^2/g)	Total pore volume (cm^3/g)	BJH adsorption pore size (nm)
CAN-37.5-90°C	x=37.5	41.9	0.41	-
CAN-18.8-90°C	x=18.8	74.8	0.49	-
SOD-18.8-25°C	x=18.8	208.6	0.29	3.0

[a] All zeolite products are aged for 3 days.

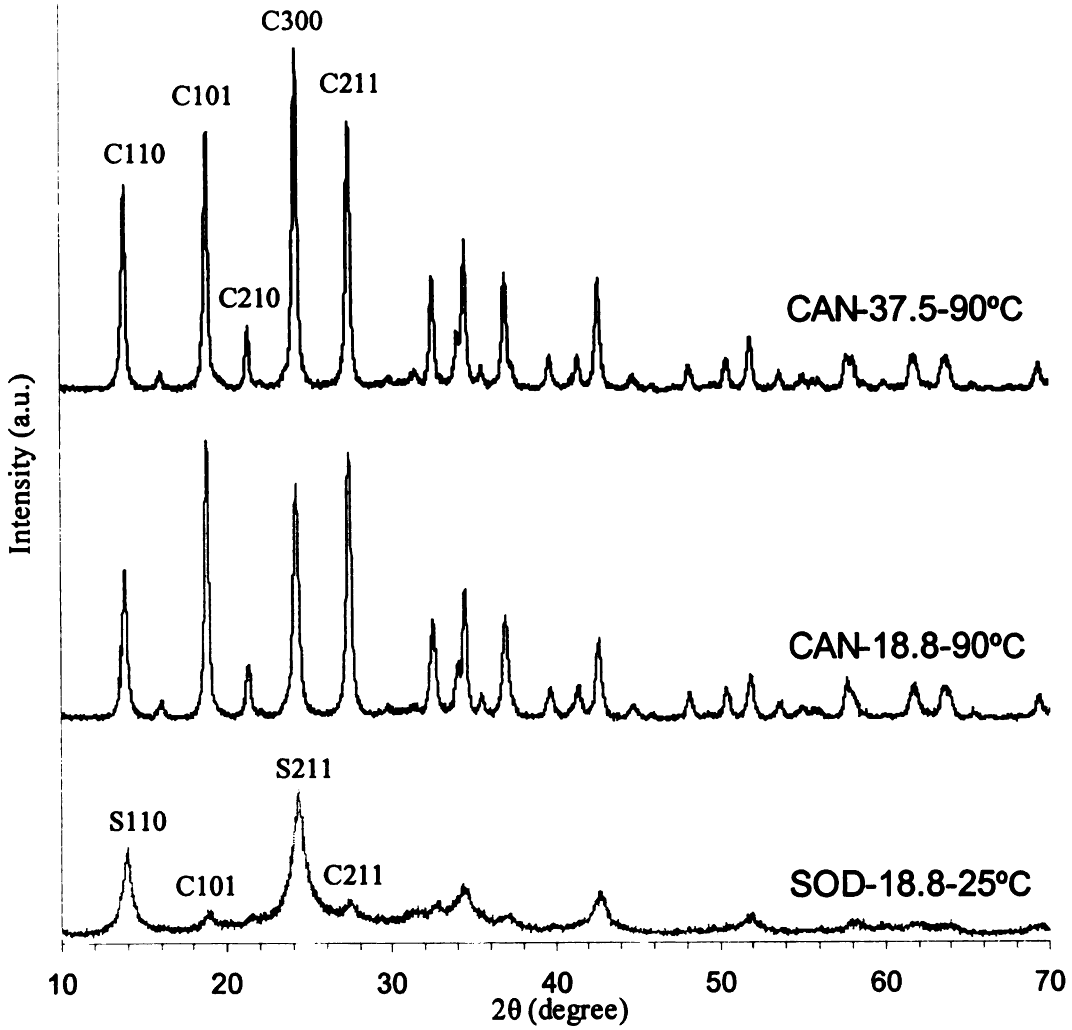

Figure 6.1 XRD patterns of synthetic zeolites after a reaction time of 3 days.

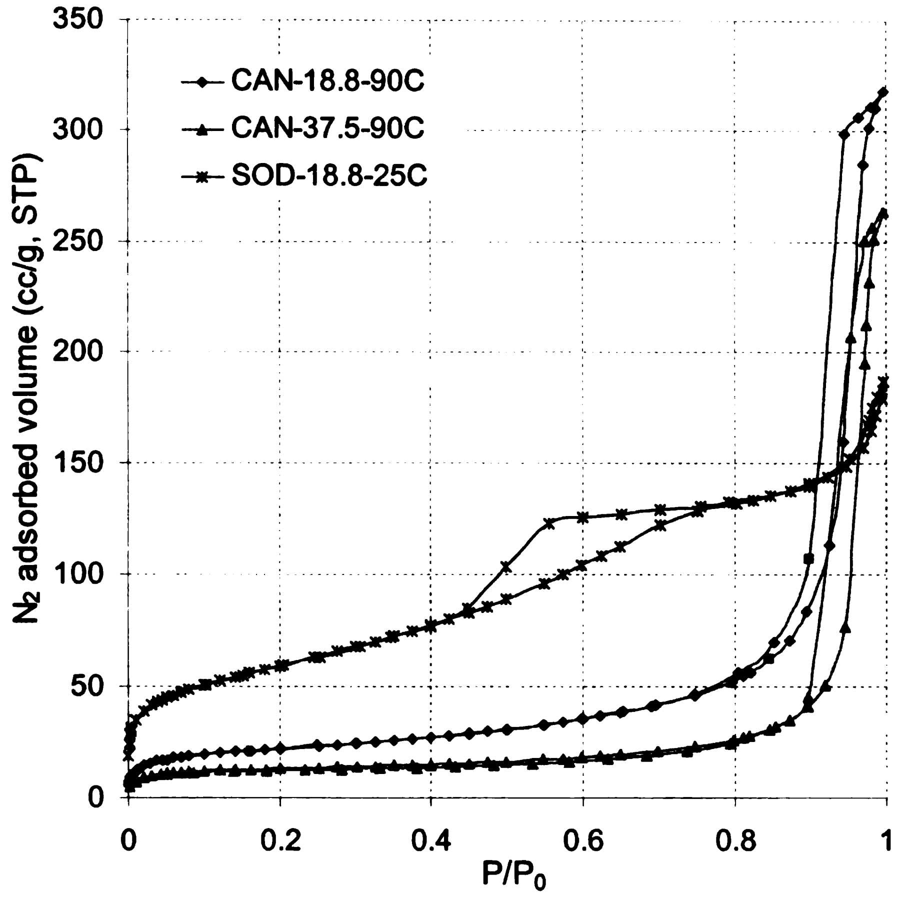

Figure 6.2 N_2 adsorption-desorption isotherms of synthetic zeolites after a reaction time of 3 days.

All of the selected zeolites exhibited visually very good dispersion in epoxy prepolymers. The distribution of sodium aluminosilicates was qualitatively judged by examining the relative intensities of zeolite diffraction peaks obtained from the lower and upper surfaces of the cured composite specimens. Little or no settling of aluminosilicate occurred during the polymer curing process because the intensities of the Bragg reflection peaks of zeolite particles from the top and bottom surfaces of the composite were equivalent.

Table 6.2 Tensile properties of glassy epoxy composites reinforced by nitrate cancrinite and sodalite

Sodium aluminosilicates	Loading (wt%)	Tensile strength (Mpa)[a]	Tensile modulus (Gpa)	Elongation-at-break (%)
Pristine Epoxy	0	82.1	3.12	5.14
CAN-37.5-90°C	2	85.9	3.19	5.16
	5	85.9	3.31	4.63
	10	94.3	3.65	5.00
CAN-18.8-90°C	2	90.4	3.29	6.39
	5	89.1	3.95	5.68
	10	94.0	3.85	5.25
SOD-18.8-25°C	5	94.9	4.19	6.95
	10	90.3	4.52	5.35

[a] The standard deviations for all values are <6%, except for the values of elongation-at-break in which case the standard deviation is <20%.

The tensile properties of glassy epoxy composites prepared from CAN and SOD zeolites and a comparison of representative stress-strain curves are provided in Table 6.2 and Figure 6.1, respectively. When compared to the pristine epoxy, all of the epoxy composites reinforced by cancrinite and sodalite demonstrate significant improvement in Young's modulus and tensile strength at all loadings. Moreover, elongation-at-break is also enhanced in most of the cases except for the cases of CAN-37.5-90°C at 5 wt% and 10 wt% loadings. For these composites, reduced elongation-at-break may be caused by the local defects (e.g. air bubbles) in the composites. The increase in the elongation-at-break additionally results in enhanced toughness.

The dramatic influence of cancrinite and sodalite on the tensile properties of the glassy polymer is obviously evidenced by the stress-strain curves (Figure 6.3). The pristine epoxy showed a failure behavior typical of a brittle material.

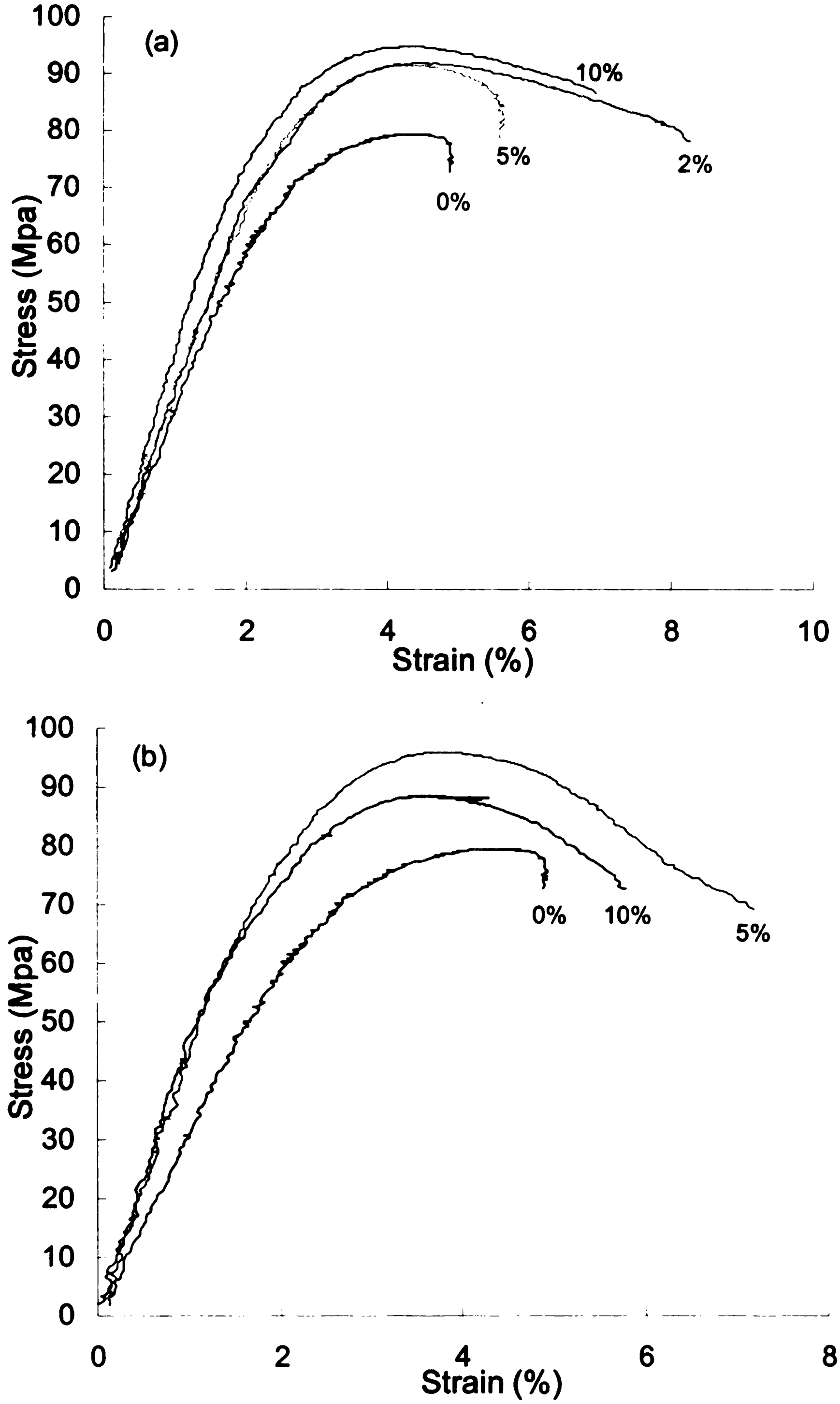

Figure 6.3 Representative stress-strain curves for glassy epoxy nancomposites reinforced by (a) CAN-18.8-90°C and (b) SOD-18.8-25°C at the wt% zeolite loadings indicated.

The stress increases with increasing load to a maximum value, after which the specimen ruptured with little yield. Similar behavior is observed for the composites, except that the composites exhibit substantial yield and the initial slopes are larger and the maximum stress is higher due to increased modulus and strength, respectively. Elastic modulus of the nanocomposites increases with increasing zeolite concentration, while stress and strain-at-break suffer from a loss in some cases. For instance, a 15.6% increase in stress and 35.2% increase in elongtation-at-break were observed at 5 wt% of SOD-18.75-25°C loading, while at 10 wt%, only a 10.0% increase in stress and 4.1% increase in elongation-at-break were achieved. It's been noticed that with increasing fillers content, especially for those fillers having good adhesion with epoxy monomers, the viscosity of epoxy precursors goes up rapidly, which may lead to the difficulty of degassing the prepolymers and associated air-bubble defects in the dog-bone samples. This may explain the loss of strength and elongation-at-break at higher loadings.

The substantial improvements in the tensile strength, stiffness and toughness achieved for the epoxy-zeolite composites in comparison to the pristine polymer most likely are a consequence of strong interfacial interaction between the epoxy polymer chains and microporous zeolites and the good dispersion of zeolite particles throughout the matrix.

It had been previously reported that poly(ethylene oxide) (PEO), poly(acrylic acid) (PA), dextran and proteins were found to be adsorbed on a dealuminated FAU-type zeolite.[29] The high specific interaction suggested the penetration of zeolite pores by macromolecules to some extent. Recently, Macko et al.[30-33] reported for the first time that the highly hydrophobic polyethylene (PE) and isotactic polypropylene (PP) may be adsorbed from solutions onto certain zeolites with pore/channel diameters ranging from ~5 to 6 Å. These authors conclude that both hydrophobic polyolefins likely penetrate and are at least partially included in the interiors of the narrow zeolite nanopores. Moreover, polymers may be synthesized within the zeolite pores, but this occurs after pre-intercalating the pores with the monomers, and then the polymer is fixed as an integral part of the zeolite lattice.[34] The cancrinite structure consists of a main one-dimensional channel system along the [001] axis and is formed from elliptical 12-rings of tetrahedra giving a pore dimension of 5.9×5.9 Å, which is big enough for the diffusion of epoxy monomers. However, there are invariably nitrate anions situated inside the channels which might impede efficient penetration of epoxy resin and curing agents from one side to another. Also, the entrance to the ε-cages of cancrinite is too small to allow entry of epoxy prepolymers. Hence, the cross-linked epoxy chains after curing process might not be included in the interiors of the cancrinite pores. Thus, the polymer most likely is adsorbed onto external surfaces of the cancrinite crystal. The increased Young's modulus is due to the cancrinite crystallites being stiffer than the epoxy matrix and the improved tensile strength can be ascribed to the strong chemical interaction between the hydroxyl groups generated during the cure reaction of epoxy monomers and the sodium cations at cancrinite external surface sites.

The magnitude of tensile property improvement achieved by CAN-18.75-90°C is better than that of CAN-37.5-90°C and this can be rationalized by the fact that CAN-18.8-90°C has a smaller particle size and associated higher BET surface area (Table 6.1) compared to CAN-37.5-90°C, thereby resulting in better dispersion and interfacial interaction with the epoxy matrix.

The pore opening in the sodalite framework structure is only 2.4×2.4 Å and is too small to expect intercalation of the epoxy polymer within the nanopores. However, the high surface area (~200 m^2/g) and a large average BJH pore size (~3.0 nm) of sodalite with a cotton-ball like morphology allows the polymer to fill the secondary pores between sodalite nanoparticles and thus eliminate the tendency toward microcrack formation between the two phases, leading to improved tensile properties. Furthermore, the reinforcing benefits provided by sodalite are superior to those provided by cancrinite at equivalent loadings.

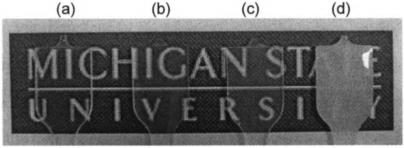

Figure 6.4 Optical image comparing the transparency of (a) pristine epoxy polymer and epoxy composites prepared from (b) CAN-18.8-90°C, (c) CAN-37.5-90°C and (d) SOD-18.8-25°C. All of the composites are at 5 wt% zeolite loading.

Another significant advantage of synthetic cancrinite as a reinforcing agent is the optical transparency of the resulting composites (cf. Figure 6.4). The transparency of the epoxy-cancrinite nanocomposite is comparable to that of the pure polymer. On the other hand, the composite made from sodalite is opaque. Thus, in comparison to sodalite, the refraction index of the cancrinite zeolite more nearly matches that of the epoxy matrix.

In order to evaluate the advantages of synthetic nitrate cancrinite and nitrate sodalite as polymer reinforcing agents, the observed mechanical properties of epoxy-zeolite nanocomposites are compared with those of epoxy nanocomposites made from organoclay, mesoporous silicas, and carbon nanotubes. Organoclays have been successfully used for reinforcing rubbery epoxy matrices[1-3], which are relatively soft and easy to reinforce. However, the reinforcement provided by organoclays became less significant for rigid glassy epoxy matrices. The strength of glassy epoxy nanocomposites was not improved by the addition of organoclays.[35] Even when uniform dispersion of exfoliated or intercalated clay nanolayers is achieved in epoxy, the tensile strength is decreased by 25% at 5 wt% of organoclay loading, although the modulus is improved by 40%.[35] The plasticizing effect of the clay organic modifiers may compromise the interfacial interactions needed for enhanced strength.

Mesoporous silicas (denoted MSU-J-TEOS and MSU-J-SS) with wormhole framework structure have been proven to be effective reinforcement agents for glassy epoxy system.[11] The larger pore mesophases (MSU-J-TEOS) provide better reinforcement at 5 wt% loading, than the corresponding smaller pore analogs (MSU-J-SS), most likely, because of more efficient polymer impregnation of the larger mesopores. A 18.2% increase in strength and a 31.3% increase in modulus were observed at 5 wt% loading of MSU-J-TEOS, in comparison to the pristine glassy epoxy. However, elongation-at-break is decreased by 15.6%. The improvements in the tensile strength and modulus provided by MSU-J-TEOS silica is comparable with those achieved by synthetic zeolites of this investigation at the same loading. Epoxy-zeolite composites made from nitrate sodalite exhibit a 15.6% and 34.3% increase in strength and modulus, respectively, at 5 wt% loading. Additionally, a 35.2% increase in elongation-at-break is realized, resulting in enhanced toughness. Therefore, microporous zeolites are better toughening agents for glassy epoxy polymer.

When carbon nanotubes are considered for reinforcement applications, it is important to address bundle formation arising from intertubular van der Waals forces.[36] Normally, surface functionalization of the nanotubes is necessary in order to facilitate the dispersion of CNTs in the polymer matrix.[14-18] In one study, a fully integrated nanotube-glassy epoxy polymer composite with covalent chemical bonding between the matrix and functionalized SWNTs is reported.[16] At a loading of only 1 wt% functionalized SWNTs, the resulting glassy epoxy composites demonstrated significant 25.3%, 30.8% and 30.8% increases in tensile strength, Young's modulus and elongation-at-break, respectively. This also suggests higher toughness with respect to the neat epoxy. For the composites with higher loading of 4 wt%, up to 70% improvement in Young's modulus was found, although no further increase of tensile strength was observed. This might indicate an upper limit to the content of nanotubes that can be added directly into epoxy resin because of a significant increase in viscosity.

6.4 Summary

Microporous nitrate cancrinite and nitrate sodalite zeolites have been used to form glassy epoxy nanocomposites containing 2-10 wt% zeolite. In comparison to the pristine epoxy polymer, epoxy composites reinforced by cancrinite and sodalite demonstrate substantial improvement in the tensile strength, modulus, elongation-at-break and toughness. For example, a 15.6% increase in strength, a 34.3% increase in modulus and a 35.2% increase in strain were observed at 5 wt% loading of SOD-18.8-25°C. The reinforcement benefits are most likely a consequence of strong interfacial interactions between the epoxy matrix and microporous zeolite. Moreover, the increases in tensile properties occur with little or no sacrifice in optical transparency.

When compared with organoclay, mesoporous silica and carbon nanotubes, microporous zeolites still exhibit advantages as reinforcing agents for glassy epoxy system. In order to achieve homogeneous dispersion in an epoxy matrix, both clay and carbon nanotubes need to be surface modified. Organically modified clays can only improve the Young's modulus, not the strength of rigid glassy epoxy. Thus, nitrate CAN and SOD are better reinforcing agents for glassy epoxy system than organoclays. Regarding functionalized CNTs, only a 1 wt% loading can reach the reinforcement benefits provided by synthetic zeolites at a 5 wt% loading. However, increasing the content of nanotubes will decrease rather than further increase the tensile strength owing to a significant increase in viscosity. The reinforcements provided by mesoporous silicas with large average pore size (~ 20 nm) are comparable with those achieved by synthetic zeolites at equivalent loading. But epoxy-silica mesocomposites suffer from a loss in the elongtation-at-break. Therefore, synthetic zeolites are better toughening agents for glassy epoxy polymer. Also, it should be noted that the improvement in tensile properties are realized without the need for organic surface modification.

References

(1) Pinnavaia, T. J.; Lan, T.; Kaviratna, P. D. *Chem. Mater.* **1995**, *7*, 2144.

(2) Pinnavaia, T. J.; Lan, T.; Kaviratna, P. D. *J. Phys. Chem. Solids* **1996**, *57*, 1005.

(3) Pinnavaia, T. J.; Lan, T. *Chem. Mater.* **1994**, *6*, 2216.

(4) Xue, S.; Pinnavaia, T. J. *Micropor. Mesopor. Mater.* **2008**, *107*, 134.

(5) Jana, S. C.; Park, J. P. *Macromolecules* **2003**, *36*, 8391.

(6) Jana, S. C.; Park, J. H. *Macromolecules* **2003**, *36*, 2758.

(7) Pluart, L. L; Duchet, J.; Sautereau, H.; Halley, P. Gerard, J.-F. *Appl. Clay Sci.* **2004**, *25*, 207.

(8) Qi, B.; Zhang, Q. X.; Bannister, M.; Mai, Y.-W. *Compos. Struct.* **2006**, *75*, 514.

(9) Park, I.; Peng, H.; Gidley, D. W.; Xue, S.; Pinnavaia, T. J. *Chem. Mater.* **2006**, *18*, 650.

(10) Jiao, J.; Sun, X.; Pinnavaia, T. J. *Adv. Funct. Mater.* **2008**, *18*, 1067.

(11) Jiao, J.; Sun, X.; Pinnavaia, T. J. *Polymer* **2009**, *50*, 983.

(12) Park, I.; Pinnavaia, T. J. *Adv. Funct. Mater.* **2007**, *17*, 2835.

(13) Wang, N.; Shao, Y.; Shi, Z.; Zhang, J.; Li, H. *J. Mater. Sci.* **2008**, *43*, 3683.

(14) Liu, L.; Grunlan, J. C. *Adv. Funct. Mater.* **2007**, *17*, 2343.

(15) Gojny, F. H.; Wichmann, M. H. G.; Fiedler, B.; Kinloch, I. A.; Bauhofer, W.; Windle, A. H.; Schulte, K. *Polymer* **2006**, *47*, 2036.

(16) Zhu, J.; Peng, H.; Rodriguez-Macias, F.; Margrave, J. L; Khabashesku, V. N.; Imam, A. M.; Lozano, K.; Barrera, E. V. *Adv. Funct. Mater.* **2004**, *14*, 643.

(17) Warren, G. L.; Sun, L.; Hadjiev, V. G.; Davis, D.; Lagoudas, D.; Sue, H.-J. *J. Appl. Polym. Sci.* **2009**, *112*, 290.

(18) Zhu, J.; Kim, J.; Peng, H.; Margrave, J. L.; Khabashesku, V. N.; Barrera, E. V. *Nano Lett.* **2003**, *3*, 1107.

(19) Kim, S.-W.; Shim, M.-J.; Lee, J.-Y. *Polym. Eng. Sci.* **1999**, *39*, 1993.

(20) Kim, S.-W.; Shim, M.-J.; Lee, J.-Y. *J. Mater. Sci.* **2001**, *36*, 4405.

(21) Kim, S.-W.; Shim, M.-J.; Lee, J.-Y. *Mater. Chem. Phys.* **1997**, *48*, 36.

(22) Narayanan, S.; Palaniappan, S.; Sreedhar, B. *Polym. Adv. Technol.* **2002**, *13*, 459.

(23) Lindner, G.-G.; Hoffmann, K.; Witke, K.; Reinen, D.; Heinemann, C.; Koch, W. *J. Solid State Chem.* **1996**, *126*, 50.

(24) Linares, C. F.; Solano, S.; Infante, G. *Micro. Meso. Mater.* **2004**, *74*, 105.

(25) Linares, C. F.; Sánchez, S.; Navarro, C. U.; Rodríguez, K.; Goldwasser, M. R. *Micro. Meso. Mater.* **2005**, *77*, 215.

(26) Linares, C. F.; Brikgi, M. *Meso. Mater.* **2006**, *96*, 141.

(27) Zheng, Y.; Qiu, W. *Chem. Eng. J.* **2009**, *145*, 483.

(28) Linares, C. F.; Colmenares, M.; Ocanto, F.; Valbuena, O. *Mater. Sci. Eng. C* **2009**, *29*, 350.

(29) Buttersack, C.; Rudolph, H.; Mahrholz, J.; Buchholz, K. *Langmuir*, **1996**, *12*, 3101.

(30) Macko, T.; Pasch, H.; Denayer, *J. F. J Chromatogr. A* **2003**, *1002*, 55.

(31) Macko, T.; Denayer, J. F.; Pasch, H.; Baron, G. V. *J. Sep. Sci.* **2004**, *26*, 1569.

(32) Macko, T.; Pasch, H.; Denayer, J. F. *J. Sep. Sci.* **2005**, *28*, 59.

(33) Macko, T.; Pasch, H.; Wang, X,; Rusa, C. C.; Hunt, M. A.; Tonelli, A. E. *Macromolecules*, **2005**, *38*, 10341.

(34) Cooney, R. P.; Millar, G. J.; Lewis, A. R.; Bowmaker, G. A. *J. Mater. Chem.* **1993**, *3*, 867.

(35) Wang, K.; Wang, L.; Wu, J.; Chen, L.; He, C. *Langmuir* **2005**, *21*, 3613.

(36) Ajayan, P. M.; Schadler, L. S.; Giannaris, C.; Rubio, A. *Adv. Mater.* **2000**, *12*, 750.